Solution-mediated alternative reaction methods for the deposition of transition metal oxide and hydroxide nanolayers

Asako Taniguchi

February 2022

Solution-mediated alternative reaction methods for the deposition of transition metal oxide and hydroxide nanolayers

Asako Taniguchi
Doctoral Program in Materials Science

Submitted to the Graduate School of
Pure and Applied Sciences
in Partial Fulfillment of the Requirements
for the Degree of Doctor of Philosophy in
Engineering

at the
University of Tsukuba

Preface

The studies presented in this thesis were carried out under the guidance of Professor Yoshikazu Suzuki in the Faculty of Pure and Applied Sciences, University of Tsukuba. In this thesis, solution-mediated alternative reaction methods were developed for the deposition of transition metal oxide and hydroxide nanolayers with catalytic activities for oxygen evolution reactions.

Now, one of the most globally-concerned issues is global warming. To realize the sustainable development of our modern society, large scale reduction of CO_2 emission is an important task of various scientific communities. In the fields of materials science, there are many subjects to aim the reduction of CO_2 exhaust. One is to enhance efficiencies of energy storage materials, devices, and systems. For example, improving the capacity and durability of Li-ion batteries has been paid much attention. Also, fuel cells that do not produce CO_2 are expected to be next generation power sources in more general uses. For all of these energy devices, controlling chemical reactions on electrode surfaces is key. For this reason, the studies on catalysts to acerate these reactions are essential. This is particularly true for the production of H_2 fuel by water-electrolysis. The equilibrium potential of water electrolysis is 1.23 eV. However, there always need overpotentials in the available water electrolytic systems. How and how much we can minimalize them is of industrial and scientific importance.

The second one where the materials scientist can contribute to the CO_2 reduction is to reduce the energy consumption for materials production. Although it is true that the thin film technology supports the current IT and IoT societies, the productions of electronic devices require a lot of energy, due to the utilization of ultra-high vacuumed processes for functional thin film deposition. If we can fabricate such functional thin films by alternative low-energy processes using aqueous solutions, it can cause a paradigm shift in manufacturing. For this ultimate goal, the initial step should be the development of the way allowing the thickness control at a nanoscale.

In this thesis, based on the above two scientific aspects, the framework of the study is constructed. Namely, the development of a novel nanoscale deposition method of functional thin films is set as a methodical target, while oxygen evolution catalysts are set as a target of the application of produced films. Thus, the thesis involves the descriptions on the advantages and disadvantages of the present thin film deposition methods to outline the research target (Chapter 1), the proof-of-concept demonstrations of solution-mediated alternative reaction methods and the design of nanoscale structures to obtain high catalytic activity for oxygen evolution reactions (Chapter 2-4). Finally, the results obtained through these studies are summarized in Chapter 5.

Asako Taniguchi

February, 2022

Contents

Chapter 1: Introduction

1.1 Thin film fabrication methods

1.1.1 General introduction for inorganic thin film fabrication methods

Functional thin films have been playing an important role in many technologies, and the development of thin film coating technologies aim to impart new functions to the surface of a substrate by controlling film thickness and structure at the nano level. For example, in modern technologies, thin film coating methods are attractive for applications in anticorrosion[1-2], catalysis[3-4], sensing[5-6], energy storage[7-8] and conversion[9-10], optics[11-12], and electronics[13-14]. As shown in Figure 1.1, inorganic thin film coating methods can be broadly classified into dry and wet-processes.

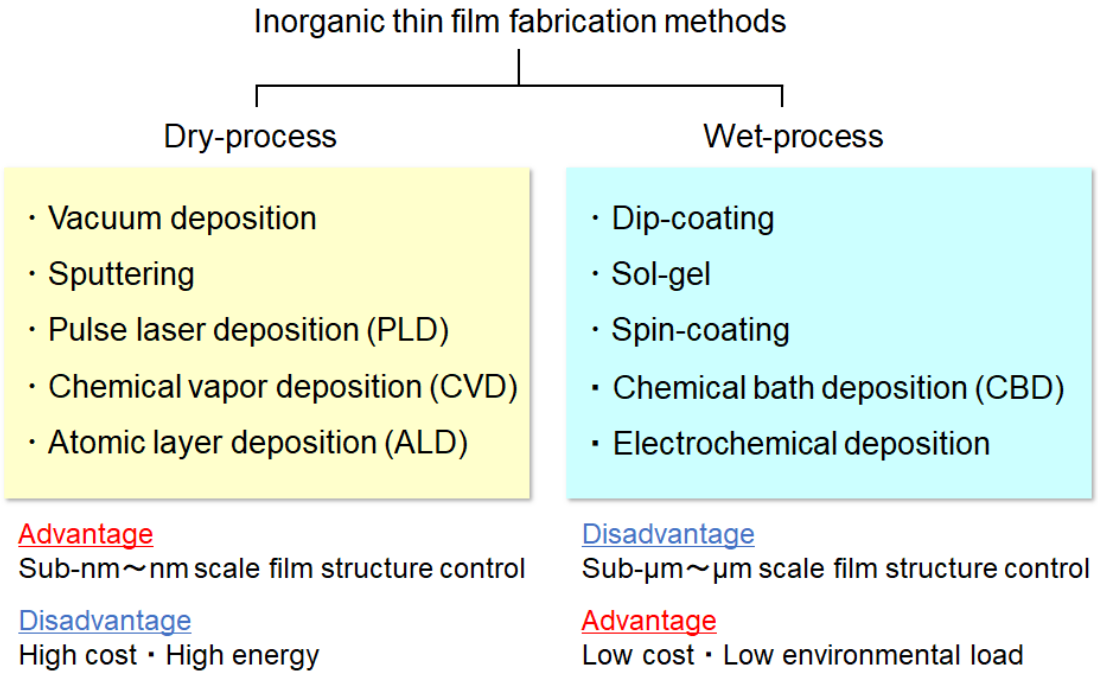

Figure 1.1. Classification of inorganic thin film fabrication methods.

1.1.2 Dry-process

The dry-process is further classified into physical vapor deposition (PVD) and chemical vapor deposition (CVD). Vacuum evaporation and sputtering are typical PVD methods. In both methods, a solid is used as the starting source. Once it is converted to a gaseous state, it is deposited on the substrate and reconstituted as a solid thin film. For example, in the vacuum evaporation method[15-17], the raw materials are heated in a vacuum to vaporize the component, which is then deposited by diffusion onto the substrate and subsequent cooling. In the sputtering method[18-20], the component is decomposed into atoms or molecules by bombarding a target then deposited on the substrate in the same process as in the vapor deposition method. In the CVD method[21-25], a target film is formed through thermal decomposition, oxidation, and reduction of vaporized raw compounds in a gas phase or on a substrate. These dry-processes can be used to produce high

quality functional inorganic thin films, but they require a high vacuum and a large external driving force to decompose and vaporize raw materials with high melting points and evaporation temperatures, respectively. Therefore, these methods are not only expensive but also require large energy consumption.

1.1.3 Wet-process

Wet-processes are simpler, less expensive, and more energy-efficient than the dry-processes. As representative wet-processes, sol-gel[26-28] and chemical bath deposition (CBD)[29-31] methods are used to fabricate functional inorganic films. In these methods, inorganic thin films are deposited using inexpensive and less toxic solution precursors under ambient pressure. In the sol-gel method, metal alkoxides are used as raw materials. Since metal alkoxide violently reacts with water for hydrolysis, organic solvents are often used. In addition, an dry atmosphere is often needed throughout the coating process to avoid hydrolysis. On the other hand, metal salts dissolved in water are used in CBD. Thus, humidity control is not necessary throughout the process, which makes it simpler. The following describes the film formation mechanisms of these wet-processes.

1.1.4 Sol-gel method

First, the sol-gel reaction in the synthesis of inorganic compounds follows the reaction pathways in a general polymer synthesis, where it includes the formation of polymer particles by condensation of monomers and gelation by their condensation. The chemical reaction can be described in a simplified form as reaction equation (1.1)-(1.3)[32].

Hydrolysis

$$M(OR)_x + H_2O \rightarrow M(OR)_{x-1}(OH) + ROH \quad (1.1)$$

Condensation (water elimination)

$$2M(OR)_{x-1}(OH) \rightarrow M_2O(OR)_{2x-2} + H_2O \quad (1.2)$$

Condensation (alcohol elimination)

$$2M(OR)_{x-1}(OH) \rightarrow M_2O(OR)_{2x-3}(OH) + ROH \quad (1.3)$$

Gel-based films are formed from hydrolysis and polycondensation reactions of the metal alkoxide. Dip-coating and spin-coating are generally used to produce gel films (Figure 1.2). In dip-coating[33-35], a substrate is immersed in a precursor alkoxide solution or sol dispersion solution, and then the substrate is pulled out of the solution to form the gel film formed through evaporation of the solvent at the air-liquid interface formed on the substrate surface. The film thickness can be controlled to some extent by the pull-up speed of the substrate and the solution concentration[36]. Spin-coating is a technique in which a substrate is fixed at the center of a rotating table, where the above precursor solution is dropped before or during rotation[37-39]. Centrifugal force causes the solution on the substrate to wet and spread, while drying occurs. The balance of these speeds

determines the thickness of the sol (or gel) layer remaining on the substrate. In the case of the spin-coating method, in addition to the solution conditions, the rotational speed of the substrate is a determining factor in the film thickness[40]. By using multiple metal alkoxides and controlling the reactivity of each, it is also possible to fabricate oxides composed of two or more metal ions. It is also possible to fabricate organic-inorganic hybrid structures by designing the organic component of the alkoxide[41-42].

The disadvantage of this technique is that, in many cases, the reaction stops by the formation of amorphous hydroxides and oxides after the coating process. In order to obtain crystallized materials, post-annealing at relatively high temperatures (500 °C or higher) is usually employed. Such heat treatment not only makes it difficult to fabricate the films on a plastic substrate, but often causes cracks and reduces film quality. In order to solve such problems, the careful design of the precursor and the annealing process should be conducted. For example, solvent molecules remain in the gel film, resulting in crack formation due to solvent evaporation. This problem is generally avoided by inserting the gel film into an electric furnace that is heated to a certain temperature. In this case, drying and solidification (dehydration-condensation) occur simultaneously to suppress the formation of pores and cracks in the resultant film. However, if the solvent has a high boiling point, such annealing conditions may even promote the formation of cracks[43].

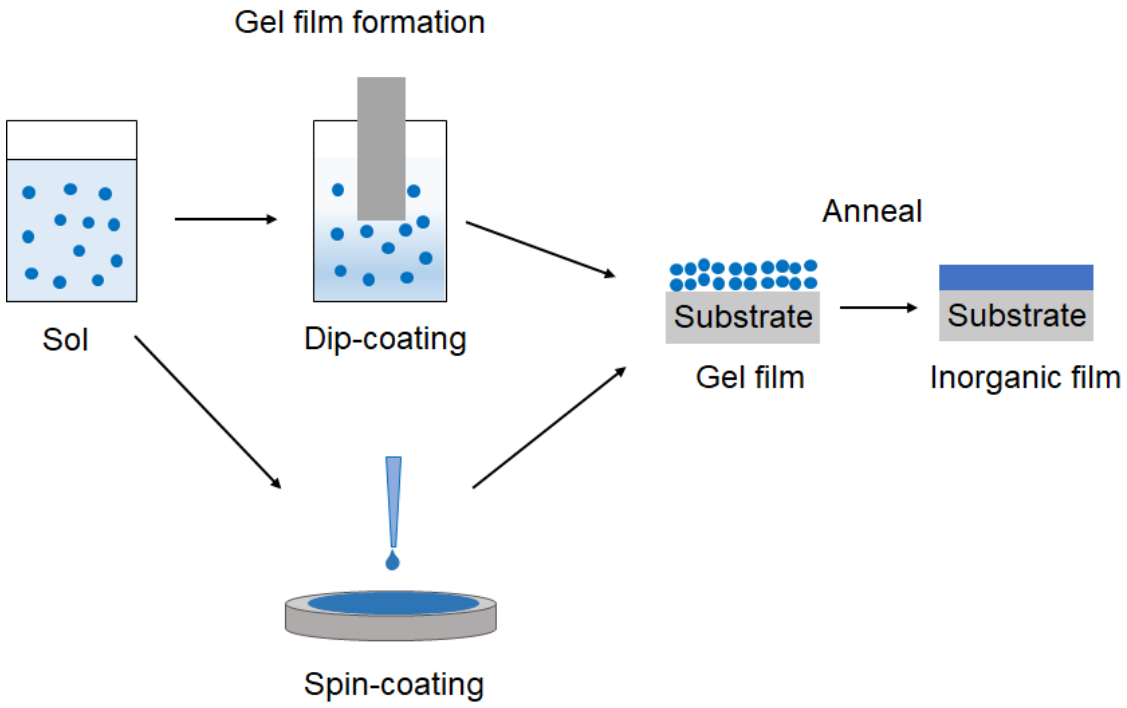

Figure 1.2. Sol-gel coating process.

1.1.5 Chemical Bath Deposition (CBD)

CBD is a technique for depositing inorganic films on a substrate using a precipitation reaction in a solution. In the simplest case (Figure 1.3 (a)), the substrate is immersed in an aqueous solution consisting of a metal salt and a precipitant (mineralizing agent). Subsequently, the solution is heated below the boiling point to induce a precipitation reaction. If the degree of supersaturation is excessive, homogeneous nucleation

predominantly occurs. In such a case, either heterogeneous nucleation on the substrate is prevented, or growth and nucleation are uncontrollable, leading to non-uniform film formation. Therefore, it is ideal to achieve film formation by heterogeneous nucleation under conditions where homogeneous nucleation does not occur by controlling the degree of supersaturation. When hydroxides are a target film component, urea is frequently used as a mineralizing agent. Since urea produces NH_4^+ by the thermal decomposition in the aqueous solution, the pH can be gradually increased by heating, and at a certain heating time, heterogeneous nucleation selectively occurs, resulting in the formation of hydroxide films. In some cases, heating causes simultaneous hydroxide precipitation and dehydration reactions, resulting in the direct formation of oxide layers[44]. For example, it has been reported that oxides such as ZnO[45], CdO[46], and TiO_2[47] can be directly formed by the CBD method without post-annealing treatment. Following the principle of controlling the degree of supersaturation, various inorganic compounds other than hydroxides and oxides can be formed by the CBD method. In fact, dozens of single- and multi-component sulfides, fluorides, etc. have been synthesized at temperatures below 100 °C using the CBD methods. As an example, the CBD method has been applied to various types of chalcogenides (CdS[48], SnS_2[49], PbS[50]), chalcopyrite ($CuInS_2$[51], $CuInSe_2$[52]), and others.

In addition, the crystal growth can also be controlled by adding surfactants and controlling the solution concentration. Techniques that allow controlling micro-, meso-, and nanoscale structures have been significantly developed in recent years. The electrochemical deposition method is a CBD that uses electrochemical reactions as the driving force for the precipitation reaction (Figure 1.3 (b))[44]. By adjusting the electrode potential, thin films can be deposited from aqueous electrolyte solutions via redox reactions at room temperature and pressure.

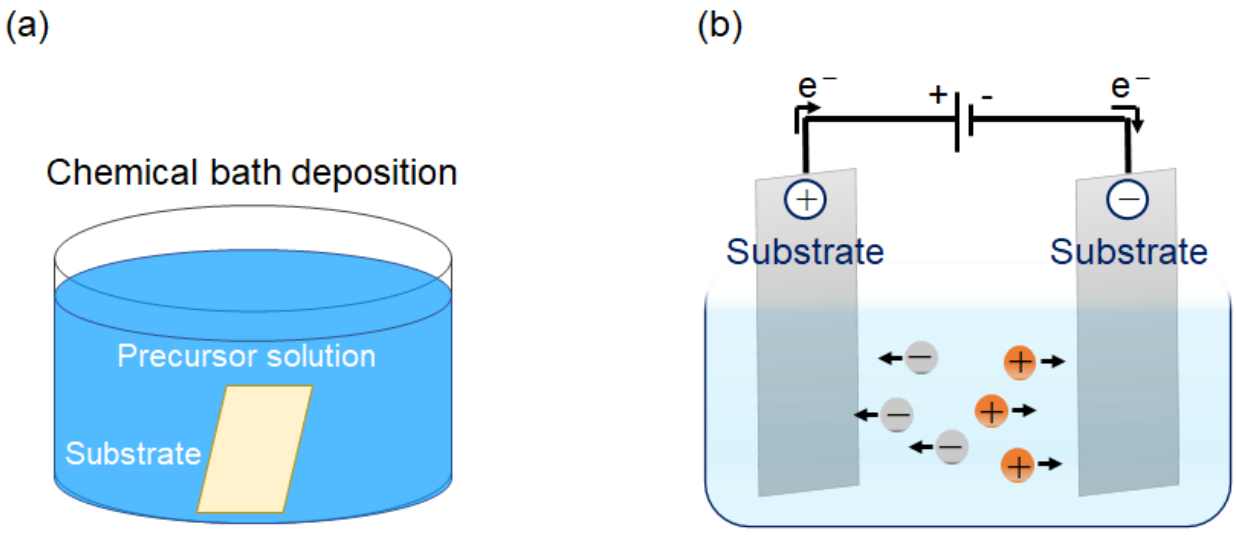

Figure 1.3. (a) Chemical bath deposition (CBD) and (b) Electrochemical deposition.

As described above, the diversity of objects to which the CBD method can be applied and the controllability of the film shape have led to its wide range of potential applications from catalyst materials, electrode materials, to solar cell materials. Nevertheless, the thickness, shape, and crystallinity of the film must

be finely controlled in order to afford sufficient properties in any cases. Nucleation depends on the density of the nucleation sites and the degree of supersaturation of the solution. These two factors are practically controlled by various experimental conditions such as substrate cleanliness, shape, surface charge, hydrophilicity, solution concentration, concentration gradient, ionic strength, etc. These parameters interact in a complex manner. Furthermore, it is difficult in principle to separate nucleation from crystal growth. Thus, the current CBD techniques suffer from the precise control in the film structure and thickness at the nanometer level. In order to solve this problem toward realizing functional nano-coatings by solution processes, it is necessary to go back to the principle of film formation and seek the development of a new film-deposition process. In addition, it is also important to design the material structure based on the mechanisms of the emergent properties.

In the thesis study, I develop a new solution process to overcome the above problems. The formation of adsorbed cationic layer and the subsequent conversion into functional inorganic layer are carried out alternately to control film formation at nanometer scale. Furthermore, I explore the novel hetero-stacking processes by taking advantage of the alternating adsorption reaction. In the following section, LbL and SILAR are refereed as the relevant technology to the method developed in my PhD study.

1.2 Adsorption based film fabrication

1.2.1 Layer-by-layer (LbL) deposition

The LbL method is used to fabricate multilayer films by repeated adsorption of the building blocks[53-55]. The oldest and still most representative method is electrostatic LbL, in which positively and negatively charged polymers are alternately adsorbed electrostatically. The principle and operation of this electrostatic LbL method are shown in Figure 1.4. Here, an example of film formation using a negatively charged substrate is introduced. First, by immersing the substrate in a solution containing the positively charged polymer cation, the polymer film is electrostatically adsorbed on the substrate. Note that the polymer located near the surface is immediately adsorbed onto the substrate, so the duration required for the saturation adsorption is a few minutes or less. Next, the substrate is pulled up from the polymer solution and the excess solution on the substrate is washed with water or another appropriate solvent. This results in a polymer adlayer with a thickness of about a single molecule. Next, by immersion in the polyanion solution, the polyanions are electrostatically adsorbed on the polycationic film formed on the substrate. Subsequent washing, immersion in the polycationic solution, washing, and immersion in the polyanionic solution are repeated to produce a polycation/polyanion multilayered film.

In the film deposition experiments at a laboratory, only a beaker and tweezers are required, which has the advantage of not requiring expensive equipment at all. On the other hand, for industrial applications, in addition to dipping, various methods such as spray[56], spin coating[57] (Figure 1.5), roll to roll deposition techniques[58], etc. can be employed depending on the application. The electrostatic LbL method is not limited to polymers, and in principle, alternative adsorption/deposition is possible as long as the two constituent materials have opposite charges. Therefore, in addition to polymers, a wide variety of materials such as inorganic nanoparticles, biomolecules, etc. can be used for the LbL deposition. In addition to the electrostatic

adsorption described here, the LbL method using hydrogen bond[59], charge transfer interaction[60], and biospecific interaction[61] as the driving force for stacking has been reported.

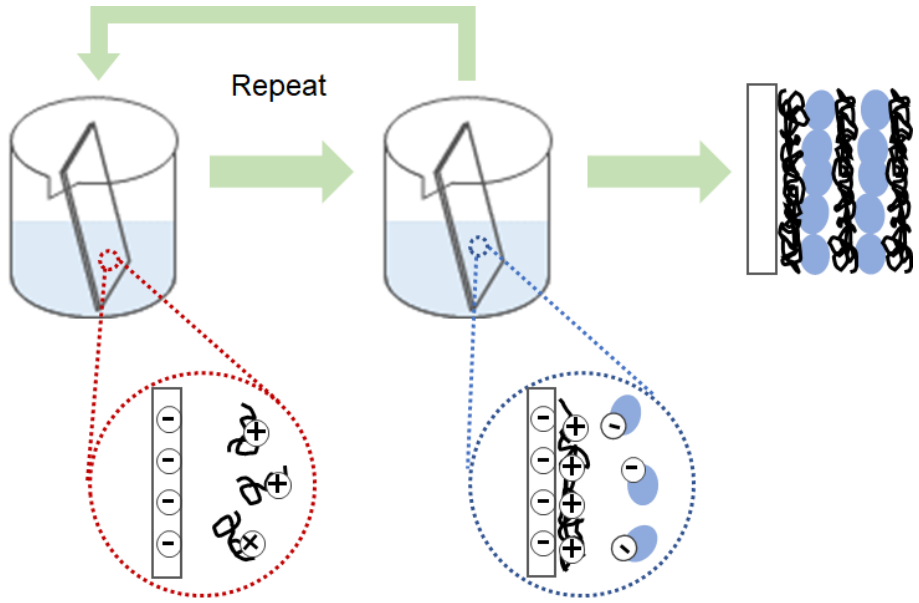

Figure 1.4. Layer-by-layer (LbL) deposition.

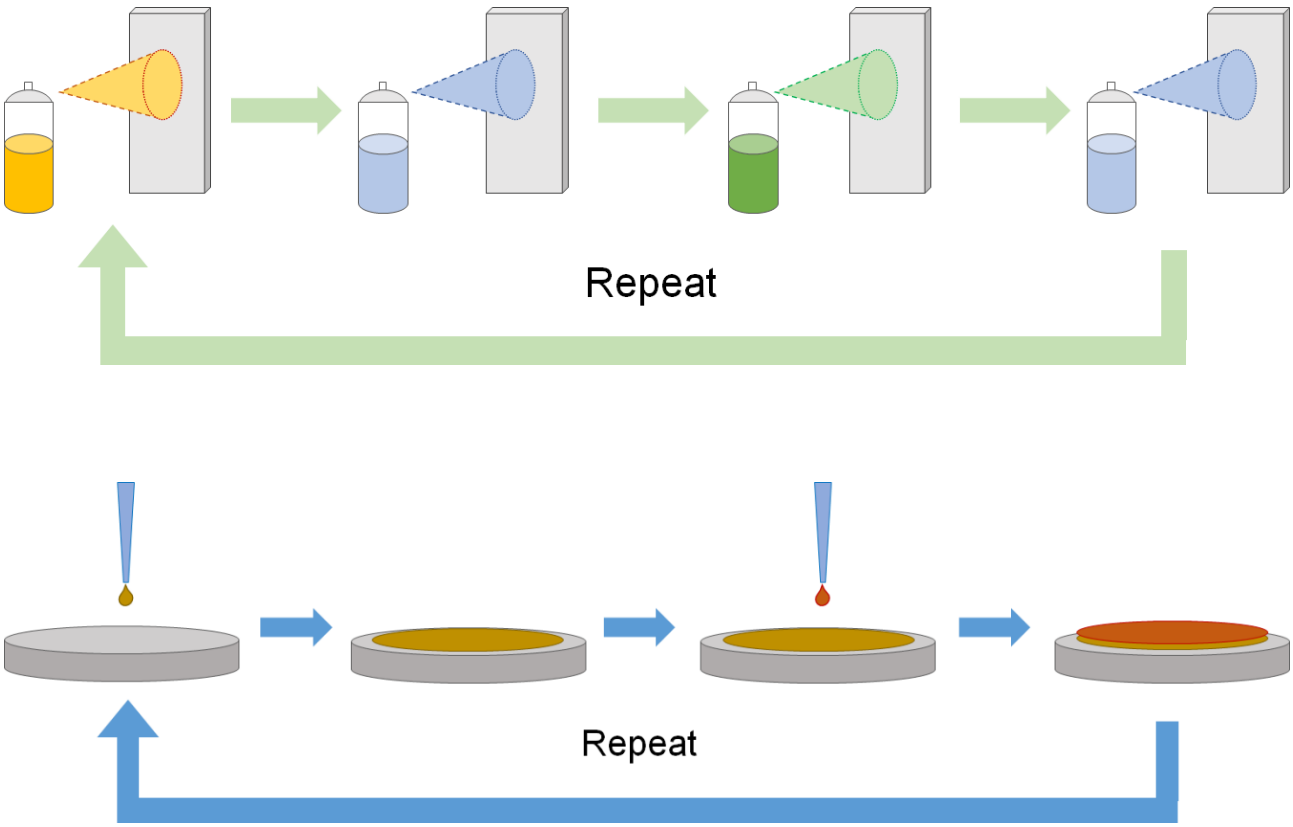

Figure 1.5. LbL with spray-coting and spin-coting methods.

1.2.2 Successive ionic layer adsorption and reaction (SILAR)

Research using the LbL method has a long history, and a wide variety of methods have been established to date. Recently, not only conventional LbL methods but also quasi-LbL methods such as unconventional LbL and pseudo-LbL have been developed[55]. In SILAR that can be categorized in quasi-LbL, two kinds of solutions, aqueous metal salt solutions and anion solutions, are used for film fabrication[62-63]. The metal component of the film is dissolved in the metal salt solution, and the anion component of the film is dissolved in the anion solution. For example, NaOH, KOH, and NH_4OH are used to fabricate hydroxide films, and NaS_2 is used to fabricate sulfide films. These solutions are used to grow the films by alternately immersing the substrate and cleaning the substrate in the middle of the process, similar to the LbL described above. Thus, one growth cycle consists of four steps, as shown in Figure 1.6. In the first step, the hydrophilic substrate is immersed in a metal salt solution to form a metal cation adlayer on the substrate surface. At the same time, an anion layer is formed on the outside of the metal cation adlayer. The bilayer, which is formed near the surface, is called a double layer or Helmholtz layer and is strongly adhered to the substrate surface. There is a diffusion layer with a mixture of cations and anions on the outside of the double layer. In the next step, the substrate is washed with water, so that only the immobile double layer adhered to the surface remains on the surface. Next, the substrate is immersed in an anion precursor solution. The anions in the solution diffuse to the substrate surface and react with the metal cations in the bilayer, forming a thin inorganic layer. In this way, the growth of the thin film takes place only on the surface of the substrate. Finally, the cation/anions in the diffusion layer are removed by substrate cleaning. Similar to electrostatic LbL, this process is repeated to form the desired thin film.

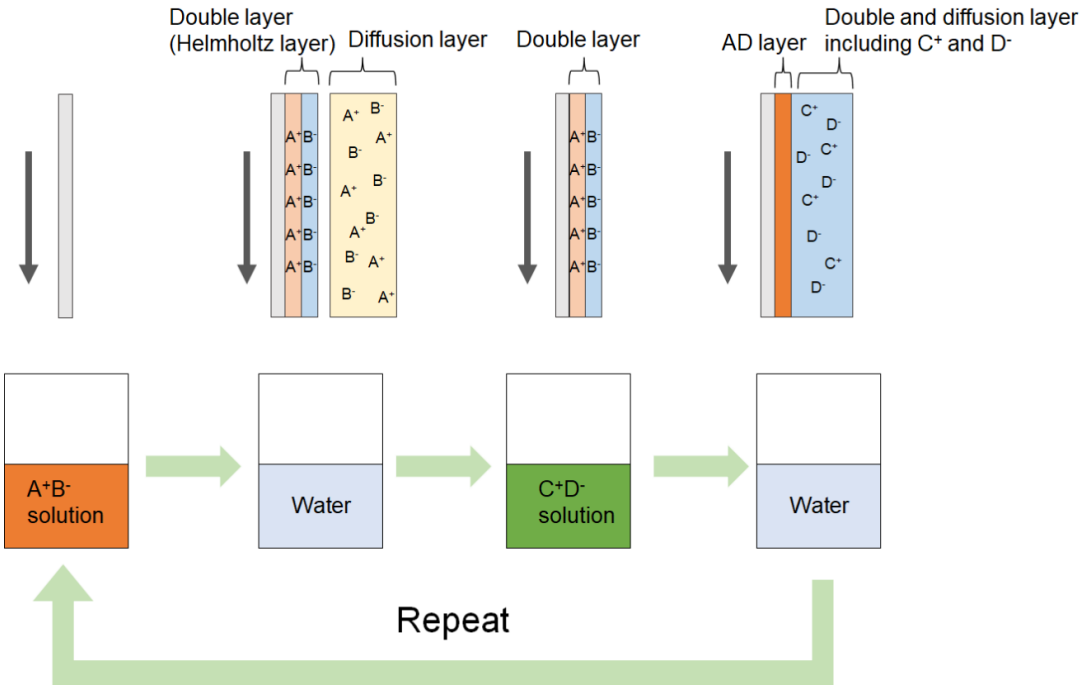

Figure 1.6. SILAR deposition method.

The historical background of the SILAR deposition began in 1985 when Y. F. Nicolau reported the deposition of ZnS and CdS using the SILAR method[64], and almost in parallel, M. Ristov *et al*. reported the deposition of polycrystalline copper oxide (Cu_2O)[65]. Y. F. Nicolau used $CdSO_4$ or $ZnSO_4$ as a metal source, Na_2S as a sulfide source. M. Ristov *et al.* used $CuSO_4$ and NaOH and as metal salt and anion sources, respectively. Since then, SILAR has been applied to the deposition of a wide variety of inorganic layers such chalcogenides[66], oxide[67], fluorides[68]. Similar to CBD, SILAR deposition is conducted from room temperature to near the boiling point of the solution. Thus, SILAR can directly deposit functional thin films on substrates with poor heat resistance such as plastics and ITO. SILAR will contribute to the development of functional thin films as a simple and inexpensive method allowing nanoscale engineering.

1.3 Hydrogen production by water-splitting

1.3.1 Electrochemical water-splitting

The current global issue to be addressed by the entire scientific and technological community is the drastic reduction of CO_2 emissions. To achieve this goal, breakthrough technologies are being developed in a variety of fields with vigorous efforts. Hydrogen (H_2) is recognized as an ideal energy source that is clean, renewable, and carbon-free because it does not emit carbon dioxide during the energy conversion process[69-70]. Fuel cells (FCs) and metal-air batteries are typical applications of hydrogen fuel, and if they are practicality used as a fundamental technology, clean energy consumption can be realized[71-72]. Among the many hydrogen production technologies, electrochemical water splitting has been attracting attention. Surplus electricity at night can be stored as H_2 fuel with this system, and when combined with renewable energy technologies such as solar cells, it is possible to produce H_2 fuel without CO_2 production[73]. The half-reactions in water electrolysis are the hydrogen evolution reaction (HER) at the cathode and the oxygen evolution reaction (OER) at the

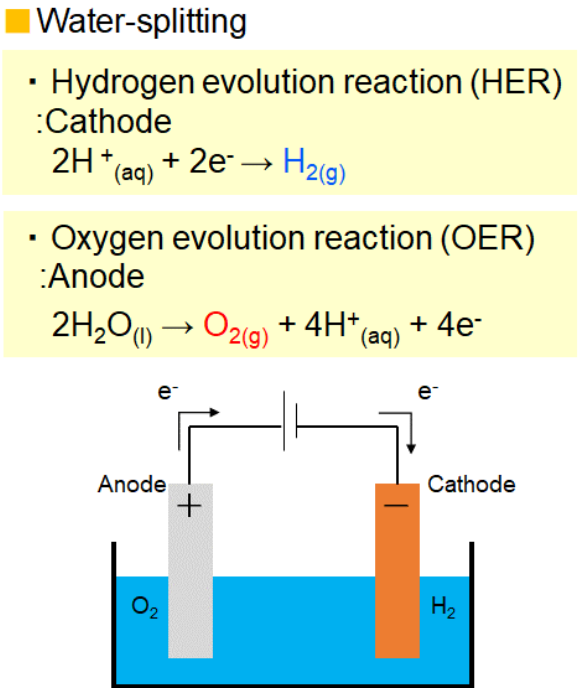

Figure 1.7. Water-electrolysis.

anode (Figure 1.7). The oxygen evolution reaction (OER) is based on a four-electron reaction and has a slow kinetic reaction and high overvoltage. In addition, its mechanism is relatively complex, making rational catalyst design difficult. Therefore, OER is the rate-limiting reaction of water electrolysis[74-76].

It is known that catalysts containing precious metals such as Pt, Ru, Ir, etc. have excellent HER and OER catalytic activities, but to use the water electrolysis for a large-scale H_2 production, the use of these precious metals must be greatly reduced or precious metal-free catalysts must be developed[77-78]. To improve the catalytic activity, it is necessary to understand the reaction mechanism between OER and HER. The following are the mechanisms of HER in water electrolysis. It should be noted that the HER reaction is pH dependent[76, 79].

(In acidic media)

Step 1 : $H^+ + e^- \rightarrow H_{ads}$

Step 2 : $H_2O + H_{ads} + e^- \rightarrow H_2 + OH^-$

(In alkaline or neutral media)

Step 1 : $H_2O + e^- \rightarrow H_{ads} + OH^-$

Step 2 : $H^+ + H_{ads} + e^- \rightarrow H_2$

As shown above, in acidic conditions, hydrogen ions (protons) bond directly with electrons and chemically adsorb on the surface of the electrocatalyst to produce H_{ads}, while in alkaline conditions, water molecules are cleaved to produce hydrogen ions (H_{ads}, an adsorbed type hydrogen intermediate). Next, in step 2, a reaction occurs in which a proton combines with the H_{ads} formed in step 1 to produce H_2 (Heyrovsky step) and two H_{ads} combine (Tafel step). For this reason, HER is generally easier to perform in acidic solutions than in alkaline solutions. A typical HER catalyst is platinum, which can initiate the HER reaction with almost no overvoltage. In recent years, many new catalysts have been developed such as MoS_2, which shows the same level of catalytic activity as Pt. Although factors other than overvoltage, such as durability and cost, need to be taken into consideration for practical use, research and development for the practical use of precious metal-free HER catalysts are progressing steadily.

As mentioned above, OER is a four-electron reaction, and the theoretical equilibrium voltage is 1.23 V. The fact that it is a multi-step and complex four-electron reaction makes the catalyst design difficult. Because of the difficulty in detecting intermediates, the mechanism of OER is not completely clear. For this reason, various reaction routes have been proposed, but the most commonly accepted one will be used as an example in this chapter[76, 80].

(In acidic media)

Step 1 : $* + H_2O \rightarrow *OH + H^+ + e^-$

Step 2 : $*OH \rightarrow *O + H^+ + e^-$

Step 3 : $*O + H_2O \rightarrow *OOH + H^+ + e^-$

Step 4 : *OOH → O_2 + H^+ +e^-

(In alkaline or neutral media)

Step 1 : OH^- → *OH + e^-

Step 2 : *OH + OH^- → *O + H_2O + e^-

Step 3 : *O + OH^- → *OOH + e^-

Step 4 : *OOH + OH^- → O_2 + H_2O + e^-

(* is the active site of the electrocatalyst)

In this four-step process, there are three reaction intermediates (*OH, *O, *OOH) representing oxygen-related species adsorbed on the catalyst surface. In this four-step process, there are three reaction intermediates (*OH, *O, *OOH) representing oxygen-related species adsorbed on the catalyst surface. Usually, water/hydroxyl ions are oxidized to produce *OH, followed by deprotonation and further oxidation to produce the intermediates *O and *OOH, and finally O_2. In acidic electrolytes, water molecules are the oxygen source, and in neutral and alkaline electrolytes, hydroxyl ions are the oxygen source. Figure 1.8 shows the polarization curve of the OER reaction. the two reactions are opposites (one is the oxidation of water, the other is the reduction of water), and the extra potential value above the equilibrium potential (1.23 V for OER[75], 0 V for HER[79]) is the result of the OER/HER reaction. The extra potential value above the equilibrium potential (1.23 V for OER and 0 V for HER) is called the overpotential (η). The smaller this overpotential is, the higher the catalytic activity is in each catalytic reaction. Therefore, in this paper, I also evaluate the catalytic activity by comparing the value of this overvoltage.

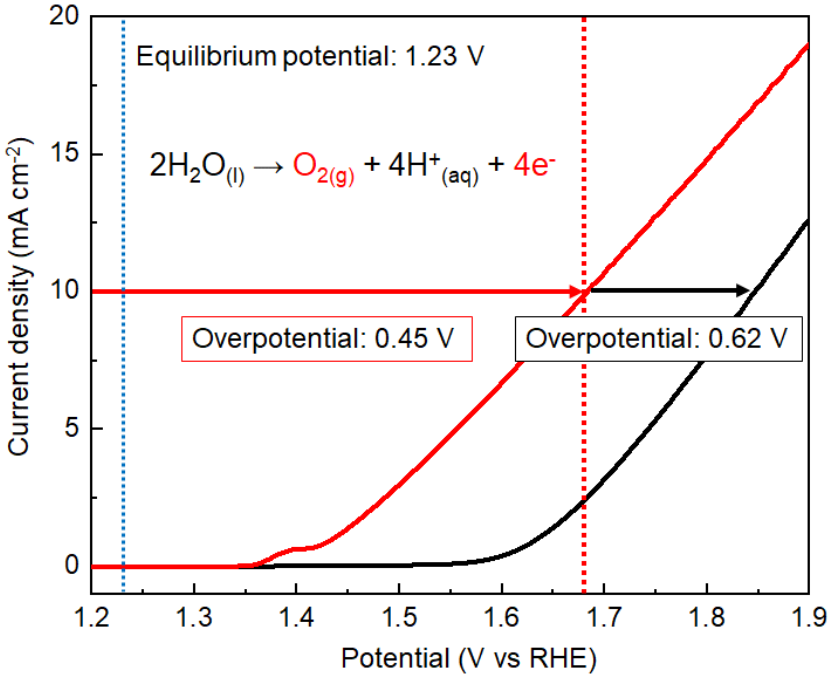

Figure 1.8. Definition of overpotential for OER.

1.3.2 OER catalysis

As for OER catalysts, it has long been known that Ru and Ir catalysts exhibit relatively low overvoltage under acidic conditions[78]. OER catalysts functioning under acidic conditions are suitable for water electrolysis systems using polymer electrolyte water electrolyzers (PEWEs), which can produce pure hydrogen at high current densities and high pressures[81]. Therefore, the system is reasonable in the operation cost. However, Ru- and Ir-based catalysts are scarce in resources and expensive. Moreover, their prices are expected to be higher when they are used for large-scale production, and there are concerns that they will be greatly affected by the economic and political circumstances of the countries of origin. Therefore, a lot of research has been conducted to develop various alternative catalysts to precious metals, such as oxides, hydroxides, chalcogenides, phosphides, nitrides, carbides, and carbons[76, 78], which are abundant on earth, and to improve the catalytic reaction rate. However, no non-precious metal catalyst that is as stable under acidic conditions and as active as precious metal catalysts have been found. On the other hand, there is an abundance of transition metal-based catalysts that exhibit excellent catalytic activity and stability under alkaline conditions. Thus, hydrogen production systems using alkaline water electrolysis (AWE) are becoming more and more promising[82-84]. In this thesis, I aim to prepare non-precious metal OER catalysts, such as iron oxides and iron-nickel hydroxides, which show high catalytic activity and are expected to be applied to AWE.

Recent progress in the development of hydroxide catalysts is summarized below[78, 84]. First of all, hydroxides and oxyhydroxides containing mainly transition metals (Fe, Co, Ni, etc.) have attracted a great deal of attention in recent years as extremely important electrocatalysts for improving the efficiency of OER. Typical examples of such non-precious metal hydroxides as OER catalysts are $Ni(OH)_2$, $Co(OH)_2$, FeOOH, or their solid solutions. Improvements in the catalytic performance of these catalysts have been achieved through compositional control, crystal structure, crystal shape, nanostructure control, and hybridization.

While IrO_2 and RuO_2 show metallic conductivity and can function as electrochemical catalysts in bulk, many hydroxides are poor conductors, so it is important to control the nanostructure to increase the efficiency of electron transport from the active site to the electrode. In addition, the layered structure of hydroxides prevents the exposure of the active sites. In this regard, how to control the nanostructure and how to increase the density of active sites are also important considerations for enhancing the catalytic activity. From both of the above perspectives, the use of single- or multi-layered hydroxide nanosheets as catalysts is a reasonable approach. For example, Liu *et al.*[85] focused on enhancing the catalytic OER activity of CoFe layered double hydroxides (LDHs) nanosheets and developed two effective exfoliation methods, liquid-phase and gas-phase, using plasma. When the water/plasma coupled exfoliation method was applied to CoFe LDHs nanosheets, ultrathin CoFe LDHs nanosheets with highly exposed active sites and a large concentration of defects and vacancies were obtained, which led to excellent OER catalytic activity (232 mV at 10 mA cm^{-2}). In addition, McAteer *et al.*[86] synthesized $Co(OH)_2$ nanosheets of various sizes by liquid-phase exfoliation of layered hydroxides and found that the catalytic activity increased as the $Co(OH)_2$ nanosheet size decreased, suggesting that the edges of the nanosheets are the active sites for OER. Zhou *et al.*[87] found that Fe was introduced into $Ni(OH)_2$ nanosheets by cation exchange method to obtain meshed $Ni_{0.83}Fe_{0.17}(OH)_2$ nanosheets with nanopores. They confirmed the uniform elemental distribution and proved that this cation exchange

method is effective for uniform Fe doping into $Ni(OH)_2$ nanosheets. In fact, $Ni_{0.83}Fe_{0.17}(OH)_2$ showed the highest OER catalytic activity compared to other metal ratios of $Ni(OH)_2$, NiFe LDH, and $Ni_xFe_{1-x}(OH)_2$[87]. This excellent OER activity can be attributed to the abundant active surface sites, abundant defects, and enhanced surface wettability. Besides exfoliation, nanosheet structures can also be obtained by other chemical reaction routes. For example, Ni nanoprisms as self-sacrificial templates were converted to Ni-Fe LDH nanosheets after hydrolysis reaction with a $FeSO_4$ solution. The Ni-Fe LDH electrocatalyst was found to exhibit excellent catalytic activity towards OER, with an overpotential as small as 280 mV at 10 mA cm^{-2}[88]. Since NiFe oxyhydroxides are probably the most active OER catalysts under alkaline conditions, the development of such nanosheet-focused catalysts is very important for understanding the factors controlling the activity of hydroxide-based catalysts.

In addition to the research on the synthesis of new materials mentioned above, mechanistic studies are also active in trying to unravel the mechanisms behind such high activity and have yielded many important insights for catalyst design. As has long been known, hydroxides are transformed into oxyhydroxides by electrochemical oxidation reactions under catalytic operating conditions[89]. Therefore, realistically, the active site of OER must be considered to involve cations with higher valence state (or oxidation state), such as Fe^{3+}, Fe^{4+}, Co^{3+}, Co^{4+}, and Mn^{3+}, rather than divalent cations. This makes it even more difficult to understand the reaction mechanism.

Enman *et al.*[90] investigated the mechanism of catalytic activity development of CoFe hydroxides using DFT calculations and operando XAS measurement techniques, and pointed out that Fe ions doped in CoFe oxyhydroxide (CoFeOOH) produced under OER operating conditions are partially oxidized and the Fe-O bond is contracted. This result strongly suggests that the Fe ion functions as an active site. To further enhance the catalytic activity, a third metal, such as W or V, has been co-doped in CoFeOOH. For example, incorporation of W resulted in an overpotential as low as 223 mV at 10 mA cm^{-2} on a glassy carbon electrode. Zhang *et al.*[91] used DFT calculations to find that co-doping of Fe and W optimizes the OH adsorption energy on Co oxyhydroxides, theoretically demonstrating a significant increase in catalytic activity for OER. The catalyst was also found to be more stable than the other catalysts. They also pointed out that the local compressive strain around large W atoms and the resulting modulated 3d electronic structure contribute to the enhanced OER activity.

1.4 Objective of this thesis

Based on the two research frameworks indicated above, I started my thesis study. This thesis is composed of five chapters: **Chapter 1**, "Introduction" describes the functional thin film fabrication methods and water splitting. **Chapter 2**, "Solution-mediated alternate reaction technique (SMART) toward nanometric growth of hematite thin films" demonstrates a novel SILAR approach to produce crystalline α-Fe_2O_3 thin films. In this study, I developed "Solution-mediated alternate reaction technique (SMART)" for hematite nanofilm deposition at low-temperature (75 ºC) with extremely simple operations. Here, I investigated the deposition mechanism as well as OER activity controlled by post-annealing and subsequent $Ni(OH)_2$ loading, where I found that the formation $Ni(OH)_2/Fe_2O_3$ heterointerface offers dramatical enchantment of the catalytic activity.

Then, in **Chapter 3**, "Nanoscale $Ni(OH)_2$/FeOOH heterostructures fabricated via an alternative deposition process and their catalytic activity", I developed a powerful method to rationally design such heterointerfaces, using the principle of SILAR. In this chapter, I demonstrate a deposition-sequence controlled route based on a SILAR to fabricate $Ni(OH)_2$/FeOOH heterostructures. The heterostructures exhibited much better catalytic activity for oxygen evolution reactions in comparison with the single component hydroxides. The result indicates the synergy of Ni/Fe ions expressed through the hetero-interface. **Chapter 4** describes "Facile and rapid formation of $Ni(OH)_2$/FeOOH heterostructures by electrochemical deposition". This study aims to develop electrochemical deposition of $Ni(OH)_2$/FeOOH catalyst in a more convenient and controllable manner than SILAR. The thickness of each layer was controlled with the deposition times. The bilayer system significantly enhanced catalytic activity for oxygen evolution reactions in comparison with FeOOH and $Ni(OH)_2$ single component layers. **Chapter 5**, "Conclusion" summarizes the achievements obtained throughout the thesis study.

References

1. Du, Y.; Zhang, Y.; Zhang, R.; Lin, S., Synthesis of Ultrathin Functional Boron Nitride Nanosheets and Their Application in Anticorrosion. *ACS Applied Nano Materials* **2021,** *4* (10), 11088-11096.

2. Nurdiwijayanto, L.; Nishijima, H.; Miyake, Y.; Sakai, N.; Osada, M.; Sasaki, T.; Taniguchi, T., Solution-Processed Two-Dimensional Metal Oxide Anticorrosion Nanocoating. *Nano Letters* **2021,** *21* (16), 7044-7049.

3. Karakaya, C.; Solati, N.; Savacı, U.; Keleş, E.; Turan, S.; Çelebi, S.; Kaya, S., Mesoporous Thin-Film NiS2 as an Idealized Pre-Electrocatalyst for a Hydrogen Evolution Reaction. *ACS Catalysis* **2020,** *10* (24), 15114-15122.

4. Farhat, R.; Dhainy, J.; Halaoui, L. I., OER Catalysis at Activated and Codeposited NiFe-Oxo/Hydroxide Thin Films Is Due to Postdeposition Surface-Fe and Is Not Sustainable without Fe in Solution. *ACS Catalysis* **2020,** *10* (1), 20-35.

5. Waikar, M. R.; Raste, P. M.; Sonker, R. K.; Gupta, V.; Tomar, M.; Shirsat, M. D.; Sonkawade, R. G., Enhancement in NH3 sensing performance of ZnO thin-film via gamma-irradiation. *Journal of Alloys and Compounds* **2020,** *830*, 154641.

6. Şahin, B.; Kaya, T., Facile preparation and characterization of nanostructured ZnO/CuO composite thin film for sweat concentration sensing applications. *Materials Science in Semiconductor Processing* **2021,** *121*, 105428.

7. Li, X.; Meng, X.; Liu, J.; Geng, D.; Zhang, Y.; Banis, M. N.; Li, Y.; Yang, J.; Li, R.; Sun, X.; Cai, M.; Verbrugge, M. W., Tin Oxide with Controlled Morphology and Crystallinity by Atomic Layer Deposition onto Graphene Nanosheets for Enhanced Lithium Storage. *Advanced Functional Materials* **2012,** *22* (8), 1647-1654.

8. Sun, X.; Zhou, C.; Xie, M.; Sun, H.; Hu, T.; Lu, F.; Scott, S. M.; George, S. M.; Lian, J., Synthesis of ZnO quantum dot/graphene nanocomposites by atomic layer deposition with high lithium storage capacity. *Journal of Materials Chemistry A* **2014,** *2* (20), 7319-7326.

9. Du, Q.; Wu, J.; Yang, H., Pt@Nb-TiO_2 Catalyst Membranes Fabricated by Electrospinning and Atomic Layer Deposition. *ACS Catalysis* **2014,** *4* (1), 144-151.

10. Xie, J.; Yang, X.; Han, B.; Shao-Horn, Y.; Wang, D., Site-Selective Deposition of Twinned Platinum Nanoparticles on $TiSi_2$ Nanonets by Atomic Layer Deposition and Their Oxygen Reduction Activities. *ACS Nano* **2013,** *7* (7), 6337-6345.
11. Nienhaus, L.; Correa-Baena, J.-P.; Wieghold, S.; Einzinger, M.; Lin, T.-A.; Shulenberger, K. E.; Klein, N. D.; Wu, M.; Bulović, V.; Buonassisi, T.; Baldo, M. A.; Bawendi, M. G., Triplet-Sensitization by Lead Halide Perovskite Thin Films for Near-Infrared-to-Visible Upconversion. *ACS Energy Letters* **2019,** *4* (4), 888-895.
12. Wu, M.; Lin, T.-A.; Tiepelt, J. O.; Bulović, V.; Baldo, M. A., Nanocrystal-Sensitized Infrared-to-Visible Upconversion in a Microcavity under Subsolar Flux. *Nano Letters* **2021,** *21* (2), 1011-1016.
13. Liang, Y.; Yong, J.; Yu, Y.; Nirmalathas, A.; Ganesan, K.; Evans, R.; Nasr, B.; Skafidas, E., Direct Electrohydrodynamic Patterning of High-Performance All Metal Oxide Thin-Film Electronics. *ACS Nano* **2019,** *13* (12), 13957-13964.
14. Jo, J.-W.; Kim, K.-H.; Kim, J.; Ban, S. G.; Kim, Y.-H.; Park, S. K., High-Mobility and Hysteresis-Free Flexible Oxide Thin-Film Transistors and Circuits by Using Bilayer Sol–Gel Gate Dielectrics. *ACS Applied Materials & Interfaces* **2018,** *10* (3), 2679-2687.
15. Hoseinpur, A.; Andersson, S.; Tang, K.; Safarian, J., Selective Vacuum Evaporation by the Control of the Chemistry of Gas Phase in Vacuum Refining of Si. *Langmuir* **2021,** *37* (24), 7473-7485.
16. Zhang, X.; Liu, X.; Sun, B.; Ye, H.; He, C.; Kong, L.; Li, G.; Liu, Z.; Liao, G., Ultrafast, Self-Powered, and Charge-Transport-Layer-Free Ultraviolet Photodetectors Based on Sequentially Vacuum-Evaporated Lead-Free $Cs_2AgBiBr_6$ Thin Films. *ACS Applied Materials & Interfaces* **2021,** *13* (30), 35949-35960.
17. Kim, N.; Shin, M.; Jun, S.; Choi, B.; Kim, J.; Park, J.; Kim, H.; Jung, W.; Lee, J.-Y.; Cho, Y.-H.; Shin, B., Highly Efficient Vacuum-Evaporated $CsPbBr_3$ Perovskite Light-Emitting Diodes with an Electrical Conductivity Enhanced Polymer-Assisted Passivation Layer. *ACS Applied Materials & Interfaces* **2021,** *13* (31), 37323-37330.
18. Najafi-Ashtiani, H.; Akhavan, B.; Jing, F.; Bilek, M. M., Transparent Conductive Dielectric−Metal−Dielectric Structures for Electrochromic Applications Fabricated by High-Power Impulse Magnetron Sputtering. *ACS Applied Materials & Interfaces* **2019,** *11* (16), 14871-14881.
19. Ishida, Y.; Corpuz, R. D.; Yonezawa, T., Matrix Sputtering Method: A Novel Physical Approach for Photoluminescent Noble Metal Nanoclusters. *Accounts of Chemical Research* **2017,** *50* (12), 2986-2995.
20. Alvi, S.; Jarzabek, D. M.; Kohan, M. G.; Hedman, D.; Jenczyk, P.; Natile, M. M.; Vomiero, A.; Akhtar, F., Synthesis and Mechanical Characterization of a CuMoTaWV High-Entropy Film by Magnetron Sputtering. *ACS Applied Materials & Interfaces* **2020,** *12* (18), 21070-21079.
21. Wang, Y.; Liu, Q.; Liu, J.; Zhang, L.; Cheng, L., Deposition Mechanism for Chemical Vapor Deposition of Zirconium Carbide Coatings. *Journal of the American Ceramic Society* **2008,** *91* (4), 1249-1252.
22. Ding, Z.; Hu, X.; Lu, G. Q.; Yue, P.-L.; Greenfield, P. F., Novel Silica Gel Supported TiO_2 Photocatalyst Synthesized by CVD Method. *Langmuir* **2000,** *16* (15), 6216-6222.
23. Garg, R.; Rajagopalan, N.; Pyeon, M.; Gönüllü, Y.; Fischer, T.; Khanna, A. S.; Mathur, S., Plasma CVD grown Al2O3 and $MgAl_2O_4$ coatings for corrosion protection applications. *Surface and Coatings Technology* **2018,** *356*, 49-55.

24. Almeida, F. A.; Salgueiredo, E.; Oliveira, F. J.; Silva, R. F.; Baptista, D. L.; Peripolli, S. B.; Achete, C. A., Interfaces in Nano-/Microcrystalline Multigrade CVD Diamond Coatings. *ACS Applied Materials & Interfaces* **2013,** *5* (22), 11725-11729.

25. Shima, K.; Otaka, Y.; Sato, N.; Funato, Y.; Fukushima, Y.; Momose, T.; Shimogaki, Y., Conformal and Stoichiometric Chemical Vapor Deposition of Silicon Carbide onto Ultradeep Heterogeneous Micropores by Controlling the Initial Nucleation Stage. *ACS Applied Materials & Interfaces* **2021,** *13* (44), 53009-53020.

26. Street, R. A.; Ng, T. N.; Lujan, R. A.; Son, I.; Smith, M.; Kim, S.; Lee, T.; Moon, Y.; Cho, S., Sol–Gel Solution-Deposited InGaZnO Thin Film Transistors. *ACS Applied Materials & Interfaces* **2014,** *6* (6), 4428-4437.

27. Chen, G.-H.; Chen, H.-S., Nanometer-Thick Sol–Gel Silica–Titania Film Infused with Superparamagnetic Fe_3O_4 Nanoparticles for Electromagnetic Interference Shielding. *ACS Applied Nano Materials* **2020,** *3* (9), 8858-8865.

28. Lee, W.-J.; Choi, J.-G.; Sung, S.; Kim, C.-H.; Na, S.; Joo, Y.-C.; Park, S.; Yoon, M.-H., Rapid and Reliable Formation of Highly Densified Bilayer Oxide Dielectrics on Silicon Substrates via DUV Photoactivation for Low-Voltage Solution-Processed Oxide Thin-Film Transistors. *ACS Applied Materials & Interfaces* **2021,** *13* (2), 2820-2828.

29. Marje, S. J.; Deshmukh, P. R.; Gunjakar, J. L.; Lokhande, C. D.; Patil, U. M., Strategically Tuned Ultrathin Nickel Phosphate Nanosheet Thin-Film Electrode as Cathode for High-Power Hybrid Supercapacitor Device. *Energy & Fuels* **2021,** *35* (17), 14110-14121.

30. Kim, D.-S.; Park, G. S.; Kim, B.; Bae, S.; Park, S. Y.; Oh, H.-S.; Lee, U.; Ko, D.-H.; Kim, J.; Min, B. K., Achieving over 15% Efficiency in Solution-Processed $Cu(In,Ga)(S,Se)_2$ Thin-Film Solar Cells via a Heterogeneous-Formation-Induced Benign p–n Junction Interface. *ACS Applied Materials & Interfaces* **2021,** *13* (11), 13289-13300.

31. Li, J.; Gong, J.; Zhu, J.; Ma, Z.; Zhao, Y.; Kong, Y.; Chi, Z.; Chen, G.; Xiao, X., Double-Sided Heat-Exchange CBD System for Homogeneous Zn(O,S) Thin Films in Highly Efficient CIGS Solar Devices. *ACS Applied Energy Materials* **2020,** *3* (11), 11242-11248.

32. Schwartz, R. W.; Narayanan, M., Chemical Solution Deposition—Basic Principles. In *Solution Processing of Inorganic Materials*, 2008; pp 33-76.

33. Brinker, C. J.; Frye, G. C.; Hurd, A. J.; Ashley, C. S., Fundamentals of sol-gel dip coating. *Thin Solid Films* **1991,** *201* (1), 97-108.

34. Lu, Y.; Ganguli, R.; Drewien, C. A.; Anderson, M. T.; Brinker, C. J.; Gong, W.; Guo, Y.; Soyez, H.; Dunn, B.; Huang, M. H.; Zink, J. I., Continuous formation of supported cubic and hexagonal mesoporous films by sol–gel dip-coating. *Nature* **1997,** *389* (6649), 364-368.

35. Kayani, Z. N.; Rahim, S.; Sagheer, R.; Riaz, S.; Naseem, S., Assessment of antibacterial and optical features of sol-gel dip coated La doped TiO_2 thin films. *Materials Chemistry and Physics* **2020,** *250*, 123217.

36. Faustini, M.; Louis, B.; Albouy, P. A.; Kuemmel, M.; Grosso, D., Preparation of Sol−Gel Films by Dip-Coating in Extreme Conditions. *The Journal of Physical Chemistry C* **2010,** *114* (17), 7637-7645.

37. Soule, L. D.; Pajares Chomorro, N.; Chuong, K.; Mellott, N.; Hammer, N.; Hankenson, K. D.;

Chatzistavrou, X., Sol–Gel-Derived Bioactive and Antibacterial Multi-Component Thin Films by the Spin-Coating Technique. *ACS Biomaterials Science & Engineering* **2020,** *6* (10), 5549-5562.
38. Hassen, M.; Riahi, R.; Laatar, F.; Ezzaouia, H., Optical and surface properties of CdSe thin films prepared by sol-gel spin coating method. *Surfaces and Interfaces* **2020,** *18*, 100408.
39. Patil, N. B.; Nimbalkar, A. R.; Patil, M. G., ZnO thin film prepared by a sol-gel spin coating technique for NO_2 detection. *Materials Science and Engineering: B* **2018,** *227*, 53-60.
40. Vorotilov, K.; Petrovsky, V.; Vasiljev, V., Spin coating process of sol-gel silicate films deposition: Effect of spin speed and processing temperature. *Journal of Sol-Gel Science and Technology* **1995,** *5* (3), 173-183.
41. Danks, A. E.; Hall, S. R.; Schnepp, Z., The evolution of 'sol–gel' chemistry as a technique for materials synthesis. *Materials Horizons* **2016,** *3* (2), 91-112.
42. Niu, B.; Zhang, F.; Ping, H.; Li, N.; Zhou, J.; Lei, L.; Xie, J.; Zhang, J.; Wang, W.; Fu, Z., Sol-gel Autocombustion Synthesis of Nanocrystalline High-entropy Alloys. *Scientific Reports* **2017,** *7* (1), 3421.
43. Hench, L. L.; West, J. K., The sol-gel process. *Chemical Reviews* **1990,** *90* (1), 33-72.
44. Bhattacharya, R., Chemical Bath Deposition, Electrodeposition, and Electroless Deposition of Semiconductors, Superconductors, and Oxide Materials. In *Solution Processing of Inorganic Materials*, 2008; pp 199-237.
45. Strano, V.; Urso, R. G.; Scuderi, M.; Iwu, K. O.; Simone, F.; Ciliberto, E.; Spinella, C.; Mirabella, S., Double Role of HMTA in ZnO Nanorods Grown by Chemical Bath Deposition. *The Journal of Physical Chemistry C* **2014,** *118* (48), 28189-28195.
46. O'Brien, P.; McAleese, J., Developing an understanding of the processes controlling the chemical bath deposition of ZnS and CdS. *Journal of Materials Chemistry* **1998,** *8* (11), 2309-2314.
47. Yin, G.; Ma, J.; Jiang, H.; Li, J.; Yang, D.; Gao, F.; Zeng, J.; Liu, Z.; Liu, S. F., Enhancing Efficiency and Stability of Perovskite Solar Cells through Nb-Doping of TiO_2 at Low Temperature. *ACS Applied Materials & Interfaces* **2017,** *9* (12), 10752-10758.
48. Husham, M.; Hassan, Z.; Selman, A. M.; Allam, N. K., Microwave-assisted chemical bath deposition of nanocrystalline CdS thin films with superior photodetection characteristics. *Sensors and Actuators A: Physical* **2015,** *230*, 9-16.
49. Ullah, S.; Bouich, A.; Ullah, H.; Mari, B.; Mollar, M., Comparative study of binary cadmium sulfide (CdS) and tin disulfide (SnS_2) thin buffer layers. *Solar Energy* **2020,** *208*, 637-642.
50. El madani, A.; Essajai, R.; Qachaou, A.; Raidou, A.; Fahoume, M.; Lharch, M., The temperature effect on the physical properties of PbS thin films produced by the chemical bath deposition (CBD) technique. *Advances in Materials and Processing Technologies* **2021**, 1-12.
51. Bini, S.; Bindu, K.; Lakshmi, M.; Kartha, C. S.; Vijayakumar, K. P.; Kashiwaba, Y.; Abe, T., Preparation of $CuInS_2$ thin films using CBD CuxS films. *Renewable Energy* **2000,** *20* (4), 405-413.
52. Vidyadharan Pillai, P. K.; Vijayakumar, K. P., Characterization of $CuInSe_2$CdS thin-film solar cells prepared using CBD. *Solar Energy Materials and Solar Cells* **1998,** *51* (1), 47-54.
53. Decher, G., Fuzzy Nanoassemblies: Toward Layered Polymeric Multicomposites. *Science* **1997,** *277* (5330), 1232-1237.

54. Ariga, K.; Hill, J. P.; Ji, Q., Layer-by-layer assembly as a versatile bottom-up nanofabrication technique for exploratory research and realistic application. *Physical Chemistry Chemical Physics* **2007,** *9* (19), 2319-2340.
55. Richardson, J. J.; Cui, J.; Björnmalm, M.; Braunger, J. A.; Ejima, H.; Caruso, F., Innovation in Layer-by-Layer Assembly. *Chemical Reviews* **2016,** *116* (23), 14828-14867.
56. Izquierdo, A.; Ono, S. S.; Voegel, J. C.; Schaaf, P.; Decher, G., Dipping versus Spraying: Exploring the Deposition Conditions for Speeding Up Layer-by-Layer Assembly. *Langmuir* **2005,** *21* (16), 7558-7567.
57. Matsuba, K.; Wang, C.; Saruwatari, K.; Uesusuki, Y.; Akatsuka, K.; Osada, M.; Ebina, Y.; Ma, R.; Sasaki, T., Neat monolayer tiling of molecularly thin two-dimensional materials in 1 min. *Science Advances* **2017,** *3* (6), e1700414.
58. Ariga, K.; Yamauchi, Y.; Rydzek, G.; Ji, Q.; Yonamine, Y.; Wu, K. C.-W.; Hill, J. P., Layer-by-layer Nanoarchitectonics: Invention, Innovation, and Evolution. *Chemistry Letters* **2014,** *43* (1), 36-68.
59. Stockton, W. B.; Rubner, M. F., Molecular-Level Processing of Conjugated Polymers. 4. Layer-by-Layer Manipulation of Polyaniline via Hydrogen-Bonding Interactions. *Macromolecules* **1997,** *30* (9), 2717-2725.
60. Shimazaki, Y.; Mitsuishi, M.; Ito, S.; Yamamoto, M., Preparation of the Layer-by-Layer Deposited Ultrathin Film Based on the Charge-Transfer Interaction. *Langmuir* **1997,** *13* (6), 1385-1387.
61. Lvov, Y.; Ariga, K.; Ichinose, I.; Kunitake, T., Layer-by-layer architectures of concanavalin A by means of electrostatic and biospecific interactions. *Journal of the Chemical Society, Chemical Communications* **1995,** (22), 2313-2314.
62. Lindroos, S.; Leskelä, M., Successive Ionic Layer Adsorption and Reaction (SILAR) and Related Sequential Solution-Phase Deposition Techniques. In *Solution Processing of Inorganic Materials*, 2008; pp 239-282.
63. Ratnayake, S. P.; Ren, J.; Colusso, E.; Guglielmi, M.; Martucci, A.; Della Gaspera, E., SILAR Deposition of Metal Oxide Nanostructured Films. *Small* **2021,** *17* (49), 2101666.
64. Nicolau, Y. F., Solution deposition of thin solid compound films by a successive ionic-layer adsorption and reaction process. *Applications of Surface Science* **1985,** *22-23*, 1061-1074.
65. Ristov, M.; Sinadinovski, G.; Grozdanov, I., Chemical deposition of Cu_2O thin films. *Thin Solid Films* **1985,** *123* (1), 63-67.
66. Pathan, H. M.; Lokhande, C. D., Deposition of metal chalcogenide thin films by successive ionic layer adsorption and reaction (SILAR) method. *Bulletin of Materials Science* **2004,** *27* (2), 85-111.
67. Jana, M.; Saha, S.; Samanta, P.; Murmu, N. C.; Kim, N. H.; Kuila, T.; Lee, J. H., A successive ionic layer adsorption and reaction (SILAR) method to fabricate a layer-by-layer (LbL) MnO_2-reduced graphene oxide assembly for supercapacitor application. *Journal of Power Sources* **2017,** *340*, 380-392.
68. Tolstoy, V. P.; Altangerel, B., A new "fluoride" synthesis route for successive ionic layer deposition of the $Zn_xZr(OH)_yF_z \cdot nH_2O$ nanolayers. *Materials Letters* **2007,** *61* (1), 123-125.
69. Seh, Z. W.; Kibsgaard, J.; Dickens, C. F.; Chorkendorff, I.; Nørskov, J. K.; Jaramillo, T. F., Combining theory and experiment in electrocatalysis: Insights into materials design. *Science* **2017,** *355* (6321), eaad4998.
70. Cook, T. R.; Dogutan, D. K.; Reece, S. Y.; Surendranath, Y.; Teets, T. S.; Nocera, D. G., Solar Energy

Supply and Storage for the Legacy and Nonlegacy Worlds. *Chemical Reviews* **2010,** *110* (11), 6474-6502.
71. Li, L.; Chang, Z.-w.; Zhang, X.-B., Recent Progress on the Development of Metal-Air Batteries. *Advanced Sustainable Systems* **2017,** *1* (10), 1700036.
72. Wang, H.-F.; Xu, Q., Materials Design for Rechargeable Metal-Air Batteries. *Matter* **2019,** *1* (3), 565-595.
73. Dresp, S.; Dionigi, F.; Klingenhof, M.; Strasser, P., Direct Electrolytic Splitting of Seawater: Opportunities and Challenges. *ACS Energy Letters* **2019,** *4* (4), 933-942.
74. Suntivich, J.; May, K. J.; Gasteiger, H. A.; Goodenough, J. B.; Shao-Horn, Y., A Perovskite Oxide Optimized for Oxygen Evolution Catalysis from Molecular Orbital Principles. *Science* **2011,** *334* (6061), 1383-1385.
75. Suen, N.-T.; Hung, S.-F.; Quan, Q.; Zhang, N.; Xu, Y.-J.; Chen, H. M., Electrocatalysis for the oxygen evolution reaction: recent development and future perspectives. *Chemical Society Reviews* **2017,** *46* (2), 337-365.
76. Yu, J.; He, Q.; Yang, G.; Zhou, W.; Shao, Z.; Ni, M., Recent Advances and Prospective in Ruthenium-Based Materials for Electrochemical Water Splitting. *ACS Catalysis* **2019,** *9* (11), 9973-10011.
77. Yuan, N.; Jiang, Q.; Li, J.; Tang, J., A review on non-noble metal based electrocatalysis for the oxygen evolution reaction. *Arabian Journal of Chemistry* **2020,** *13* (2), 4294-4309.
78. Wu, Z.-P.; Lu, X. F.; Zang, S.-Q.; Lou, X. W., Non-Noble-Metal-Based Electrocatalysts toward the Oxygen Evolution Reaction. *Advanced Functional Materials* **2020,** *30* (15), 1910274.
79. You, B.; Tang, M. T.; Tsai, C.; Abild-Pedersen, F.; Zheng, X.; Li, H., Enhancing Electrocatalytic Water Splitting by Strain Engineering. *Advanced Materials* **2019,** *31* (17), 1807001.
80. Guo, Y.; Park, T.; Yi, J. W.; Henzie, J.; Kim, J.; Wang, Z.; Jiang, B.; Bando, Y.; Sugahara, Y.; Tang, J.; Yamauchi, Y., Nanoarchitectonics for Transition-Metal-Sulfide-Based Electrocatalysts for Water Splitting. *Advanced Materials* **2019,** *31* (17), 1807134.
81. Babic, U.; Suermann, M.; Büchi, F. N.; Gubler, L.; Schmidt, T. J., Critical Review—Identifying Critical Gaps for Polymer Electrolyte Water Electrolysis Development. *Journal of The Electrochemical Society* **2017,** *164* (4), F387-F399.
82. Sun, Z.; Wang, G.; Koh, S. W.; Ge, J.; Zhao, H.; Hong, W.; Fei, J.; Zhao, Y.; Gao, P.; Miao, H.; Li, H., Solar-Driven Alkaline Water Electrolysis with Multifunctional Catalysts. *Advanced Functional Materials* **2020,** *30* (27), 2002138.
83. Kuckshinrichs, W.; Ketelaer, T.; Koj, J. C., Economic Analysis of Improved Alkaline Water Electrolysis. *Frontiers in Energy Research* **2017,** *5* (1).
84. Wang, J.; Gao, Y.; Kong, H.; Kim, J.; Choi, S.; Ciucci, F.; Hao, Y.; Yang, S.; Shao, Z.; Lim, J., Non-precious-metal catalysts for alkaline water electrolysis: operando characterizations, theoretical calculations, and recent advances. *Chemical Society Reviews* **2020,** *49* (24), 9154-9196.
85. Liu, R.; Wang, Y.; Liu, D.; Zou, Y.; Wang, S., Water-Plasma-Enabled Exfoliation of Ultrathin Layered Double Hydroxide Nanosheets with Multivacancies for Water Oxidation. *Advanced Materials* **2017,** *29* (30), 1701546.
86. McAteer, D.; Godwin, I. J.; Ling, Z.; Harvey, A.; He, L.; Boland, C. S.; Vega-Mayoral, V.; Szydłowska,

B.; Rovetta, A. A.; Backes, C.; Boland, J. B.; Chen, X.; Lyons, M. E. G.; Coleman, J. N., Liquid Exfoliated $Co(OH)_2$ Nanosheets as Low-Cost, Yet High-Performance, Catalysts for the Oxygen Evolution Reaction. *Advanced Energy Materials* **2018,** *8* (15), 1702965.

87. Zhou, Q.; Chen, Y.; Zhao, G.; Lin, Y.; Yu, Z.; Xu, X.; Wang, X.; Liu, H. K.; Sun, W.; Dou, S. X., Active-Site-Enriched Iron-Doped Nickel/Cobalt Hydroxide Nanosheets for Enhanced Oxygen Evolution Reaction. *ACS Catalysis* **2018,** *8* (6), 5382-5390.

88. Yu, L.; Yang, J. F.; Guan, B. Y.; Lu, Y.; Lou, X. W., Hierarchical Hollow Nanoprisms Based on Ultrathin Ni-Fe Layered Double Hydroxide Nanosheets with Enhanced Electrocatalytic Activity towards Oxygen Evolution. *Angewandte Chemie International Edition* **2018,** *57* (1), 172-176.

89. Burke, M. S.; Enman, L. J.; Batchellor, A. S.; Zou, S.; Boettcher, S. W., Oxygen Evolution Reaction Electrocatalysis on Transition Metal Oxides and (Oxy)hydroxides: Activity Trends and Design Principles. *Chemistry of Materials* **2015,** *27* (22), 7549-7558.

90. Enman, L. J.; Stevens, M. B.; Dahan, M. H.; Nellist, M. R.; Toroker, M. C.; Boettcher, S. W., Operando X-Ray Absorption Spectroscopy Shows Iron Oxidation Is Concurrent with Oxygen Evolution in Cobalt–Iron (Oxy)hydroxide Electrocatalysts. *Angewandte Chemie International Edition* **2018,** *57* (39), 12840-12844.

91. Zhang, B.; Zheng, X.; Voznyy, O.; Comin, R.; Bajdich, M.; García-Melchor, M.; Han, L.; Xu, J.; Liu, M.; Zheng, L.; Arquer, F. P. G. d.; Dinh, C. T.; Fan, F.; Yuan, M.; Yassitepe, E.; Chen, N.; Regier, T.; Liu, P.; Li, Y.; Luna, P. D.; Janmohamed, A.; Xin, H. L.; Yang, H.; Vojvodic, A.; Sargent, E. H., Homogeneously dispersed multimetal oxygen-evolving catalysts. *Science* **2016,** *352* (6283), 333-337.

Chapter 2: Solution-mediated alternate reaction technique (SMART) toward nanometric growth of hematite thin films

Overview

This chapter describes a simple, low-temperature, and environmentally friendly aqueous route for the layer-by-layer nanometric growth of crystalline α-Fe_2O_3. The formation mechanism involves alternative sequences of the electrostatic adsorption of Fe^{2+} ions on the surface and the subsequent onsite oxidation to Fe^{3+}. A combined analysis of X-ray diffraction, scanning electron microscopy, UV-Vis spectroscopy, and X-ray photoelectron spectroscopy revealed that α-Fe_2O_3 is directly formed without post-growth annealing *via* designed chemical reactions with a growth rate of *ca.* 1.7 nm per deposition cycle. The obtained α-Fe_2O_3 layer exhibits electrocatalytic activity for water oxidation and, at the same time, insignificant photo-electrocatalytic response, indicating its defective nature. The electrocatalytic activity was tailored by annealing up to 500 °C in air, where thermal diffusion of Sn^{4+} into the α-Fe_2O_3 lattice from the substrate probably provides increased electrical conductivity. The subsequent surface modification with $Ni(OH)_2$ lowers the overpotential (250 mV at 0.5 mA/cm^2) in a 1M KOH solution.

2.1 Introduction

In this study, a solution-based alternative reaction method is designed and demonstrated for the growth of α-Fe_2O_3. In the introduction, the difficulties of direct solution growth of α-Fe_2O_3 are particularly described. Ceramics coating is a core technology that affords various functions to a substrate material. Metal oxides are particularly attractive for applications in anticorrosion[1], catalysis[2], sensing[3], energy storage[4] and conversion[5], optics[6], and electronics[7]. In an industry context, oxide materials are deposited by vacuum phase deposition techniques such as chemical vapor deposition[8], pulsed laser deposition[9], and sputtering[10]. Solution deposition techniques such as sol-gel[11], electrodeposition[12], and chemical bath deposition (CBD) methods[13] are potential alternatives to the above-mentioned vacuum processes as they utilize inexpensive and less toxic solution precursors as well as ambient pressure for oxide deposition, hence making the fabrication more environmentally friendly and more cost-effective.

Moreover, a solution process enables the direct deposition of crystalline oxides on the substrate without post-growth annealing. A low-temperature direct deposition is suitable for film formation on low heat-resistant substrates, expanding the potential scope of functional oxide materials as a component in flexible plastic devices and electrochemical devices with indium-tin-oxide substrates. Recent efforts have allowed the fabrication of various oxide (*e.g.*, ZnO[14], TiO_2[15], WO_3[16], and SnO_2[17]) *via* aqueous solution routes without the need for a post-annealing treatment. However, so far, the direct solution routes have been adopted for tiny members in the broad family of metal oxides. The major difficulty lies in the growth mechanism; according to classical aqueous chemistry, the metallic ions (M^{n+}) in an aqueous solution react with OH^- to precipitate

hydroxide nucleus on the substrate *via* a heterogenous nucleation process (2.1)[18]:

$$M^{n+} + nOH^- \rightarrow M(OH)_n \quad (2.1)$$

If the stability of hydroxide is sufficiently low for dehydration, the hydroxide spontaneously transforms into an oxide form during deposition (2.2)[18]:

$$M(OH)_n \rightarrow MO_{n/2} + n/2H_2O \quad (2.2)$$

However, hydroxides are often stable so that a post-annealing treatment is inevitable for oxide formation. For example, annealing temperatures over 500 ºC are necessary to yield Al_2O_3[19] and ZrO_2[20] from the hydroxides. This difficulty also applies to hematite (α-Fe_2O_3) (Figure 2.1), the target material in this study. Resultant products from classical precipitation reactions between ferric or ferrous precursors with an aqueous base are α-FeOOH, β-FeOOH, γ-FeOOH, σ-FeOOH, and $Fe_5OH_8 \cdot 4H_2O$[21-23], while one can find no direct solution route to α-Fe_2O_3 (Figure 2.2). Nevertheless, magnetite (Fe_3O_4) can be formed *via* a co-precipitation process of ferric and ferrous precursors, even at room temperature[21]. In other words, Fe-$(OH)_2$-Fe bonds can preferentially convert Fe-O-Fe bonding *via* dehydration in an aqueous solution, opening the possibility for direct solution deposition of crystalline α-Fe_2O_3 under suitable reaction conditions. In fact, using the above idea a spin-spray method was developed for the growth of the α-Fe_2O_3 layer *via* an onsite oxidation and dehydration pathway (Figure 2.3)[24]. In this method, a source solution containing Fe^{2+} and an oxidizing solution containing an oxidizer, $NaNO_2$, was simultaneously sprayed onto the substrates mounted on a rotating table heated to 95 ºC. It is proposed that the deposition mechanism involved alternative sequences of the absorption of Fe^{2+} ions onto the surface and the subsequent formation of Fe^{3+}-oxygen bonds through reactions with the source and oxidizing solutions, respectively (Figure 2.4). It is referred to this deposition process as solution mediated alternative reaction. Such a non-classical solution-mediated alternative reaction strategy may open direct growth pathways to functional metal oxide nanolayers *via* aqueous solution chemistry. However, the spin spray technique is available only in specialized laboratories.

In this study, it is explored that a solution-mediated alternate reaction technique, SMART, to further verify, simplify, and generalize the non-classical solution-mediated alternative reaction pathway (Figure 2.5). Briefly, film deposition in SMART proceeds simply by alternate immersion of the substrate in $FeCl_2$ and $NaNO_2$ precursor solutions. It is demonstrated that a primitive beaker process allows the direct growth of crystalline α-Fe_2O_3 films with a growth rate of *ca.* 1.7 nm per cycle. Resultant α-Fe_2O_3 thin films exhibit unexpected electrocatalytic activity for oxygen evolution reactions (OER). The origin of catalytic activity comes from the defective nature of SMART-derived α-Fe_2O_3 where OH^- species are present in the oxide lattice. Sn^{4+}-diffusion into the α-Fe_2O_3 lattice by annealing and surface modification with $Ni(OH)_2$ further enhance the OER activity, which is superior to state-of-the-art α-Fe_2O_3-based catalysts.

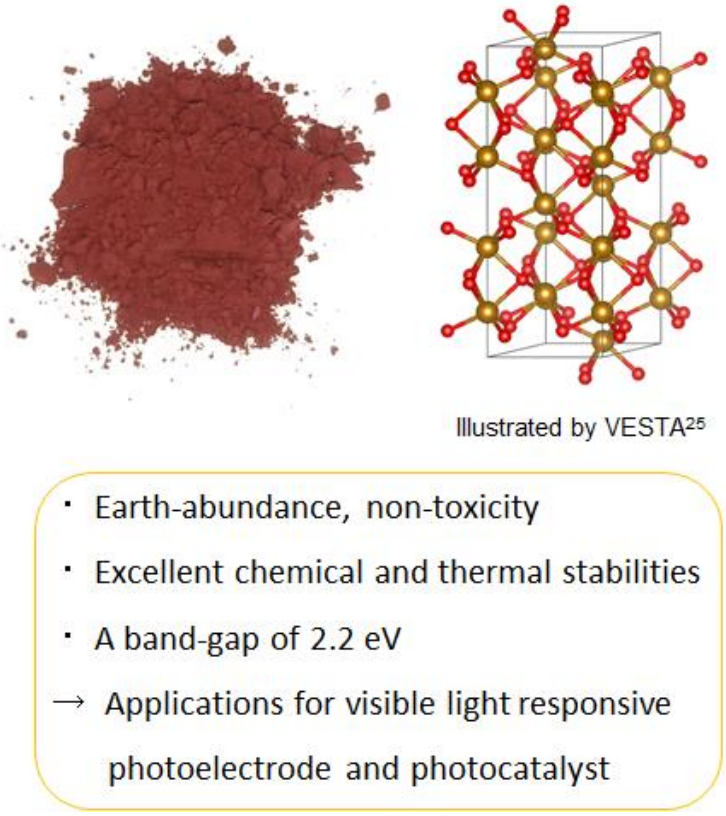

Figure 2.1. Hematite (α-Fe_2O_3) powder and the crystal structures drown by VESTA ver. 3.4.4[25].

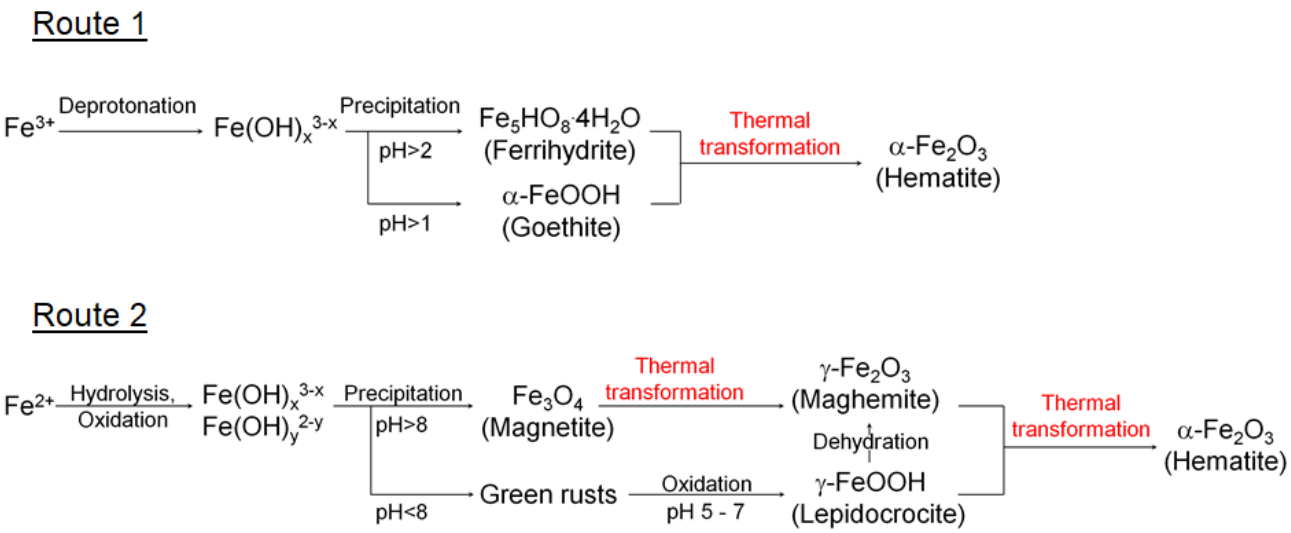

Figure 2.2. Formation of hematite *via* aqueous solution reactions. **Routes #1** and **#2** show the conventional precipitation reactions with Fe^{3+} and Fe^{2+} salts, respectively[24].

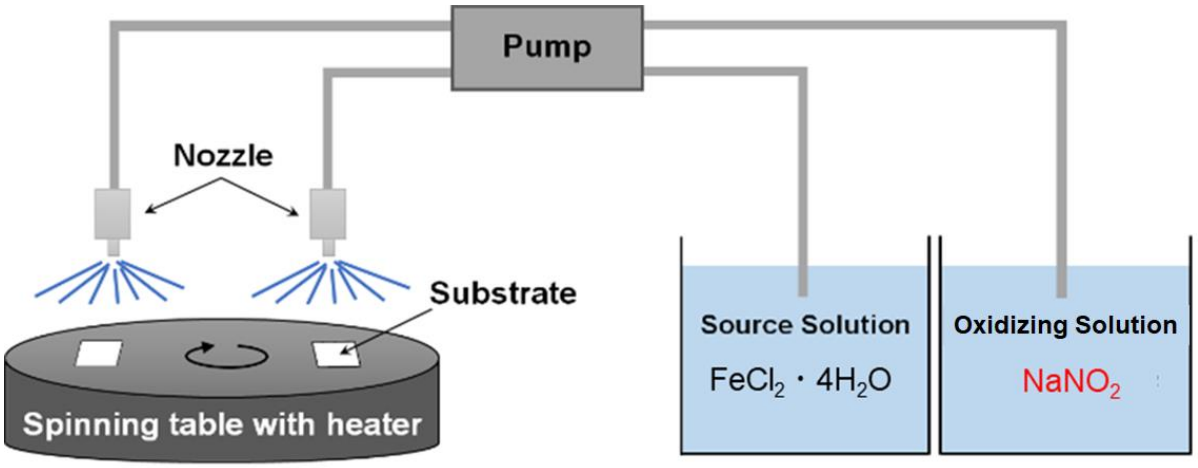

Figure 2.3. Schematic of the spin-spray setup. The source and oxidizing solutions containing an iron precursor and an oxidizing agent and a pH adjuster agent, respectively, were sprayed onto the substrates mounted on a temperature-controlled rotating table[24].

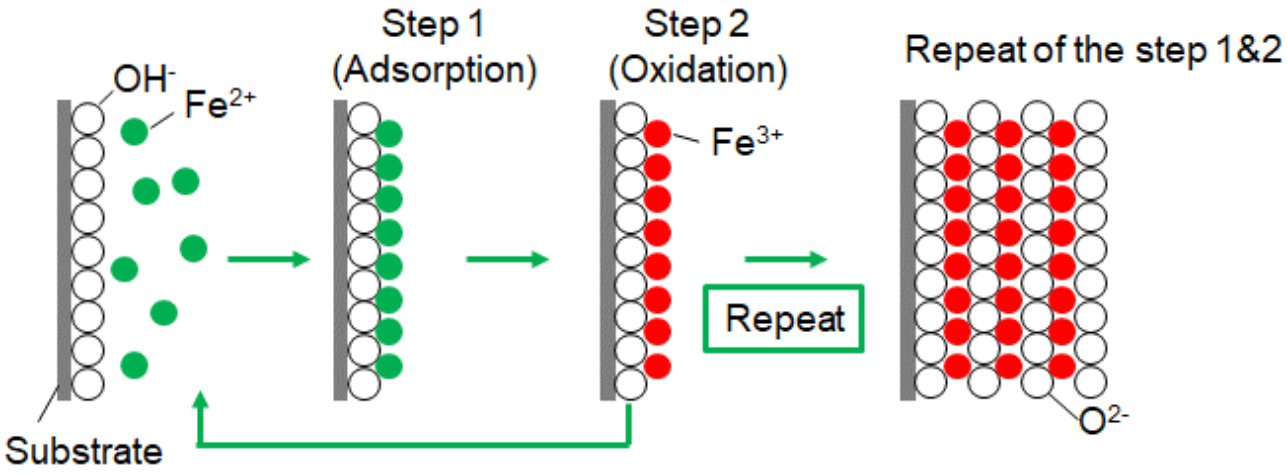

Figure 2.4. The proposed deposition mechanism of the spin-spray methods.

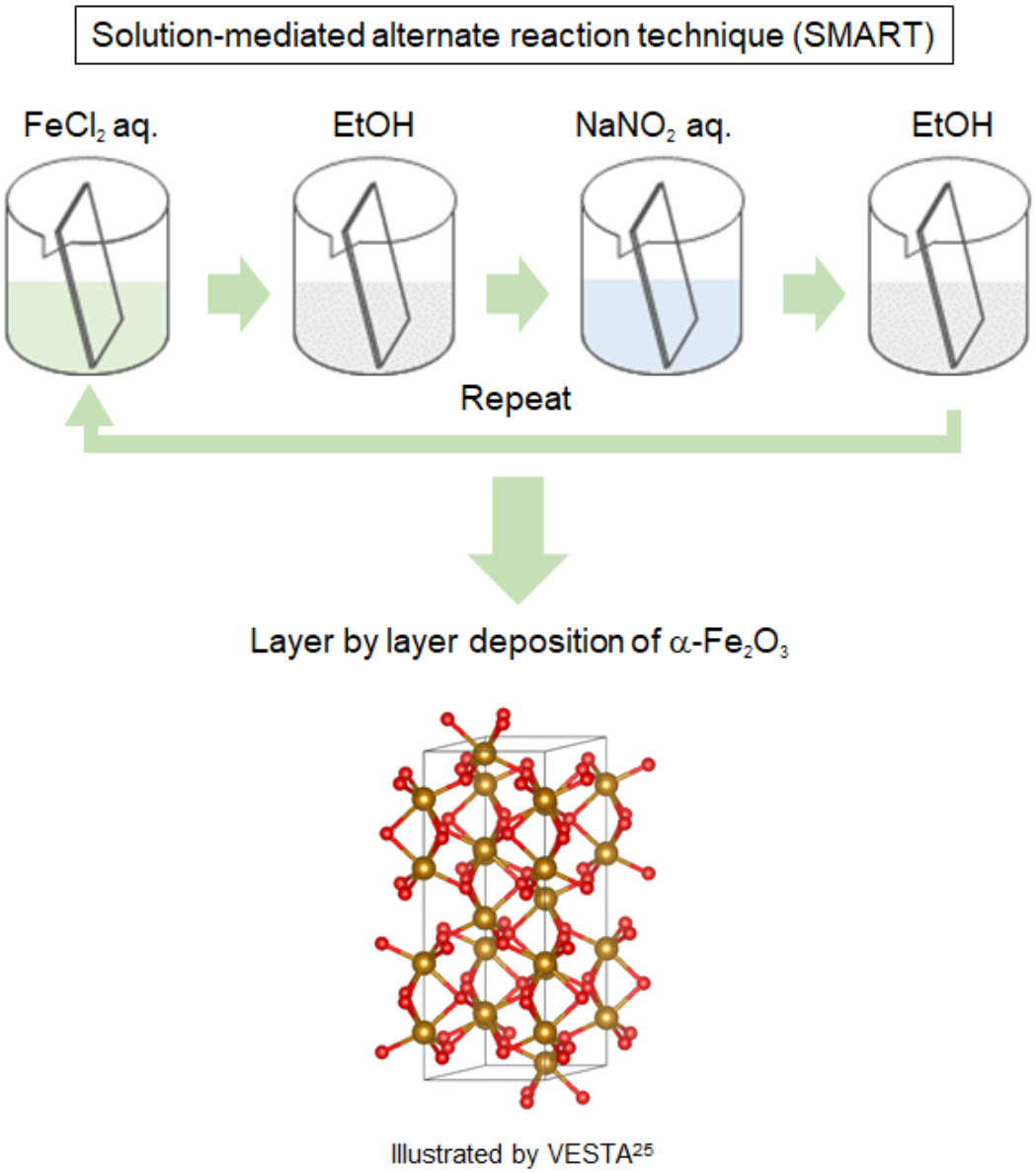

Figure 2.5. The procedure and concept of solution-mediated alternate reaction technique (SMART).

2.2 Experimental

2.2.1 Preparation of the source and oxidizing solutions.

$FeCl_2 \cdot 4H_2O$ (99.0-102.0 %, FUJIFILM Wako Pure Chemical Corp.) was used as the metal source precursor. The source solution was prepared by dissolving 20 mM of $FeCl_2 \cdot 4H_2O$ in 50 mL of distilled water. The oxidizing solution was prepared by dissolving 20 mM of sodium nitrite ($NaNO_2$, 98.5 %, FUJIFILM Wako Pure Chemical Corp.) in 50 mL of distilled water. Nitrogen gas was purged into the solutions at a rate of 1.0 L/min while stirring to prevent the oxidation of the reactants in the solution.

2.2.2 Deposition process in SMART.

A soda-lime glass substrate (25 mm × 25 mm × 1 mm) and a transparent conductive oxide (TCO) coated glass substrate (ITO/FTO, Type-0052, 10 Ω/sq, Geomatec Co., Ltd.) were cleaned in an ultrasonic bath with distilled water, ethanol, and acetone for 10 min each. The glass substrate was further cleaned by treatment in a bath of methanol (FUJIFILM Wako Pure Chemical Corp.)/HCl (FUJIFILM Wako Pure Chemical Corp.) (1/1 in volume) for 1 day to obtain a hydrophilic surface, while the TCO substrate was immersed in the 0.1 M HCl (Wako Pure Chemical Industries) for 1 day to obtain a hydrophilic surface.

The surface-modified substrate was first immersed in the source solution heated to 75 °C for 1 min, followed by rinsing with ethanol. Then the substrate was immersed in the oxidizing solution heated at 75 °C for 1 min and rinsed with ethanol again. A series of these operations were repeated from 1 to 90 times to control the film thickness (Figure 2.6).

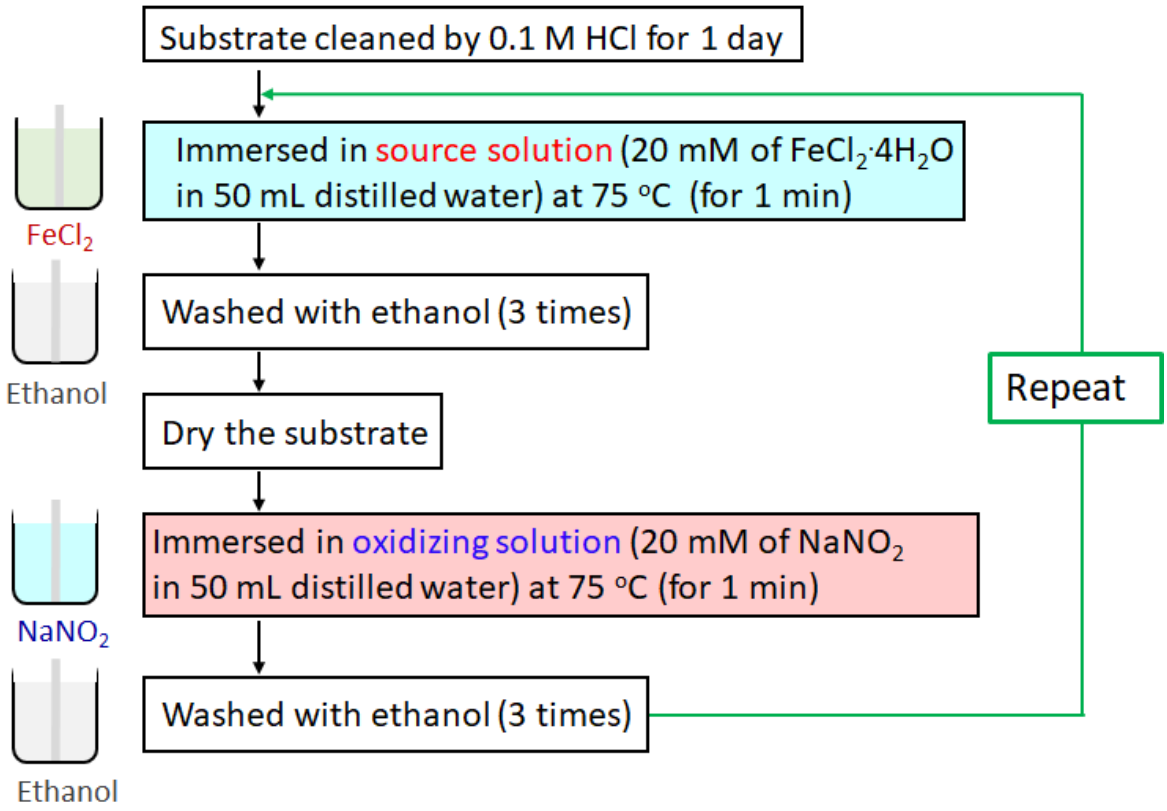

Figure 2.6. Flowchart of SMART procedure.

2.2.3 $Ni(OH)_2$ surface-modification.

α-Fe_2O_3 layer deposited on TCO was immersed in 0.1 M $Ni(NO_3)_2 \cdot 6H_2O$ aqueous solution (98.0 %, FUJIFILM Wako Pure Chemical Corp.) for 1 min without heating followed by rinsing with distilled water. Then, the substrate was immersed in 1 M KOH solution (FUJIFILM Wako Pure Chemical Corp.) without heating for 1 min, and then rinsed with distilled water (Figure 2.7).

2.2.4 Fabrication of $Ni(OH)_2$ layer by a successive ionic layer adsorption and reaction (SILAR).

The surface-modified substrate was first immersed in a 0.1 M $Ni(NO_3)_2 \cdot 6H_2O$ aqueous solution (98.0 %, FUJIFILM Wako Pure Chemical Corp.) heated to 75 °C for 1 min, followed by rinsing with water. Then the substrate was immersed in a 1 M KOH solution (FUJIFILM Wako Pure Chemical Corp.) heated at 75 °C for 1 min and rinsed with water. The process was repeated 30 times to obtain $Ni(OH)_2$ layer (Figure 2.8).

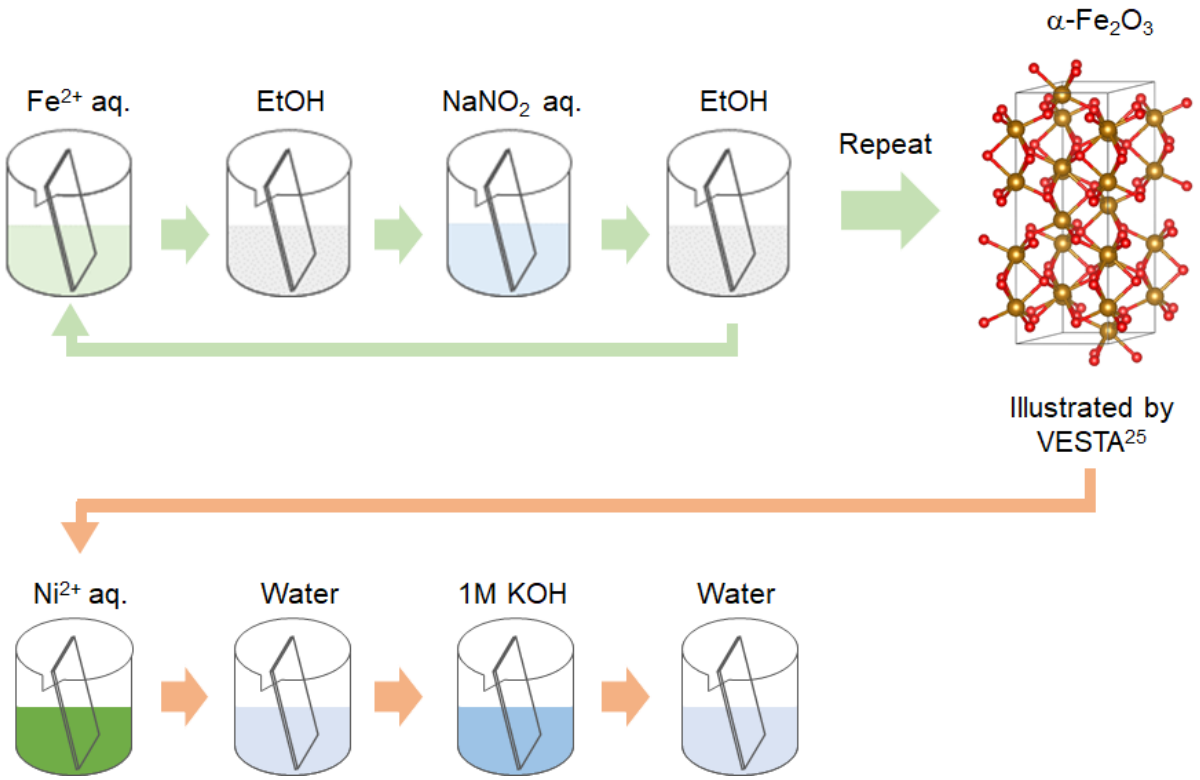

Figure 2.7. The procedure of $Ni(OH)_2$ modification of hematite surface.

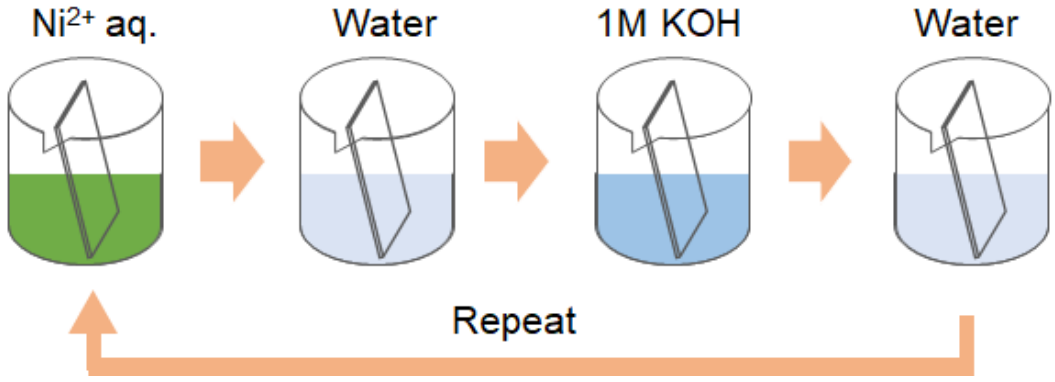

Figure 2.8. The procedure of $Ni(OH)_2$ deposition by SILAR.

2.2.5 Characterization.

The crystalline phases of the deposited films were identified by X-ray diffraction (XRD, MultiFlex, Cu Kα, 40 kV and 40 mA, Rigaku). The surface morphologies and textures of the films were observed using a scanning electron microscope (SEM, SU-8020, Hitachi High-Technologies). The elemental distribution was observed by energy-dispersive X-ray spectroscopy (EDS, JEOL, JSM-7600). The light absorbance of samples in the ultraviolet-visible (UV-Vis) region was evaluated by visible absorption spectroscopy (UV-Vis, UV-1280, Shimadzu). X-ray photoelectron spectroscopy (XPS, JPS 9010 TR, JEOL) was conducted to investigate the chemical state of the samples. All measured XPS spectra were calibrated corresponding to the value of the C 1s peak at 284.4 eV using Mg Kα X-ray source with 1253.6 eV. Raman spectroscopy measurements were made LabRam Armis, Horiba Jobin Yvon instrument equipped with 532 nm laser and a microscope to focus the laser light on the film surface.

2.2.6 Electrochemical and Photoelectrochemical Measurements.

The OER measurements were performed in 1 M KOH aqueous solution (FUJIFILM Wako Pure Chemical Corp.) using a three-electrode configuration, with a Pt wire counter electrode and an Ag/AgCl, KCl reference electrode (Figure 2.9). All potentials have been referenced to the reversible hydrogen electrode (RHE) by the expression: $V_{RHE} = V_{Ag/AgCl} + 0.197\ V + 0.059\ V \times pH$. The linear sweep voltammograms (LSV) were performed for 20 cycles with a scan rate of 5 mV s^{-1}.

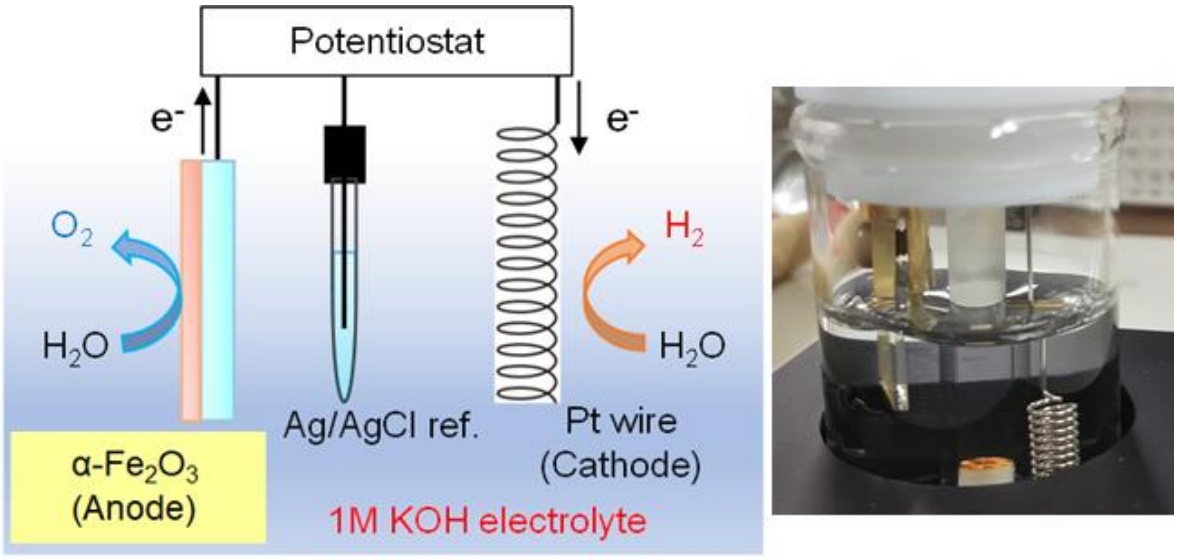

Figure 2.9. OER measurement conditions.

Photoelectrochemical measurements were performed at the same condition, while visible light (wavelength above 400 nm) was irradiated for the measurements (Figure 2.10). The 200 W Xeon lamp (Asahi Spectra. Co) was used for the measurements.

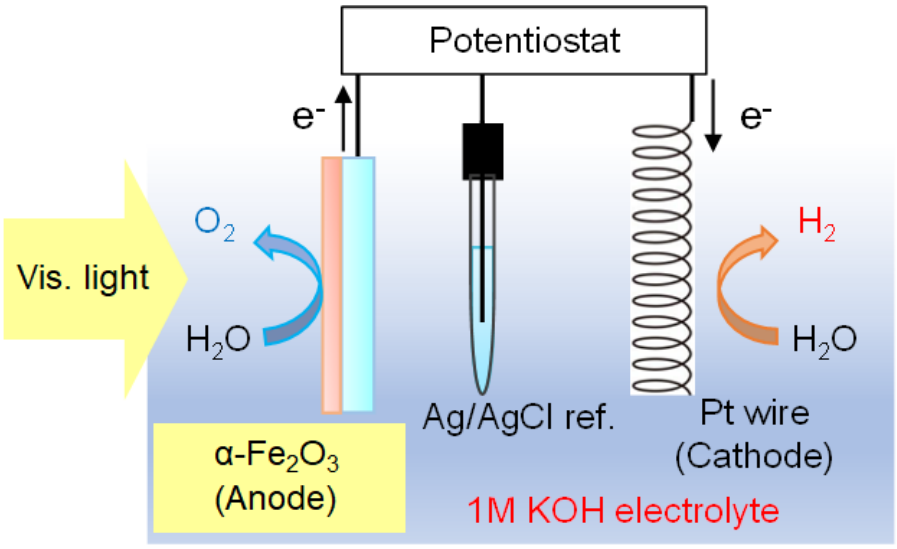

Figure 2.10. Conditions for the photoelectrochemical OER measurement.

2.3 Results and Discussion

2.3.1 Characterization of SMART-derived thin films.

The reaction pathway of SMART is designed as follows. In the first step, the substrate is immersed in a $FeCl_2$ solution with pH 4 to form a Fe^{2+} adlayer onto the substrate surface. When an oxide surface is negatively charged at the pH, a double layer is formed on the surface where Fe^{2+} forms an inner layer (Stern layer) and the Cl^- from the $FeCl_2$ precursor forms a charge-balancing outer layer. In the following step, the substrate is rinsed with ethanol so that only the immobile double-layer remains on the substrate surface. Subsequently, the substrate is immersed in the $NaNO_2$ solution and heated to 75 °C. The NO_2^- in the solution is diffused onto the surface to oxidize the adsorbed Fe^{2+} to the Fe^{3+} state. At this stage, hydrolysis and dehydration simultaneously occur onsite, resulting in the formation of the first O-Fe-O bonds. In the final step, the substrate is rinsed again to remove the ions from the diffusion layer. In principle, the repletion of these cycles leads to a layer-by-layer deposition of the α-Fe_2O_3 layer.

Figure 2.11 shows the X-ray diffraction pattern from the sample prepared by the SMART on the glass substrate after 90 cycles of deposition. The pattern displays broad peaks from the glass substrate and sharp peaks corresponding to 104 and 110 reflections of the α-Fe_2O_3 phase (JCPDS 33-0664) without an impurity phase such as $Fe(OH)_2$, $Fe(OH)_3$, FeOOH, Fe_3O_4, and γ-Fe_2O_3. According to Scherrer's equation using a 104 peak, the crystallite size is calculated to be 47.4 nm[26]. Raman spectroscopy was employed to further investigate the phase purity of the resultant films. As shown in Figure 2.12, all the detected peaks are assigned as two A_{1g} modes (231 and 473 cm^{-1}) and four E_g modes (255, 297, 411, and 576 cm^{-1})[27-28], in support of the film being composed of α-Fe_2O_3 domains. Note that Raman spectra up to 1400 cm^{-1} shown in Figure 2.12, also exclude the formation of iron-based impurity phases[29].

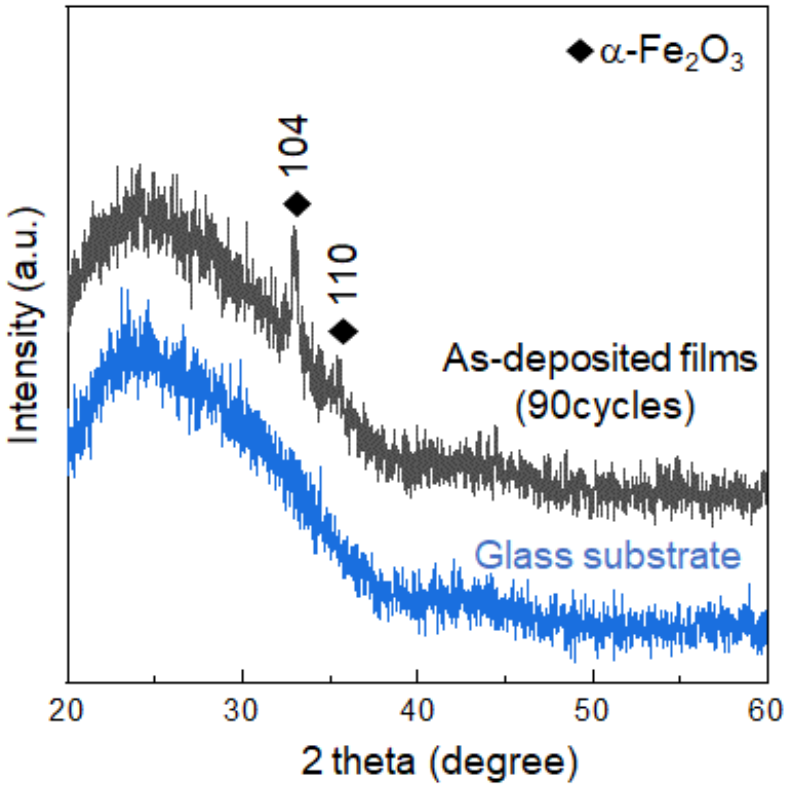

Figure 2.11. XRD pattern of SMART-derived α-Fe_2O_3 on a glass substrate deposited after 90 cycles.

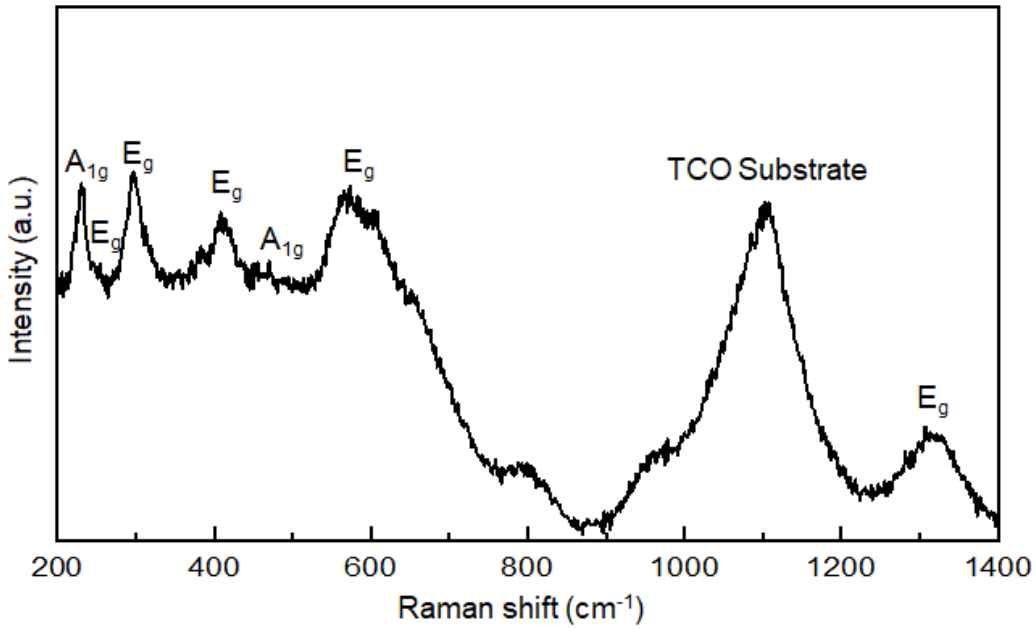

Figure 2.12. Wide-range Raman spectrum of SMART-derived α-Fe_2O_3 on a TCO substrate deposited after 90 cycles.

Figure 2.13 displays the cross-sectional and surface SEM images of the SMART-derived α-Fe_2O_3 film. The cross-sectional image reveals the formation of a dense layer with a relatively uniform thickness of 150 nm on average. Thus, the growth rate can be estimated at approximately 1.7 nm per deposition cycle, if the film thickness linearly increases in each deposition cycle. The surface image presents a continuous film consisting of dense grains with an average size of *ca.* 50 nm. The grain size roughly matches the calculated crystallite size (47.4 nm) from the XRD pattern, indicating that each grain consists of a single crystalline domain. Indeed, the SEM observation with a lower magnification confirms that the film is free from cracks (Figure 2.14). The film exhibited good adhesion to the substrate after scotch tape testing, indicating the presence of chemical bonds at the interface between the substrate and the α-Fe_2O_3 layer.

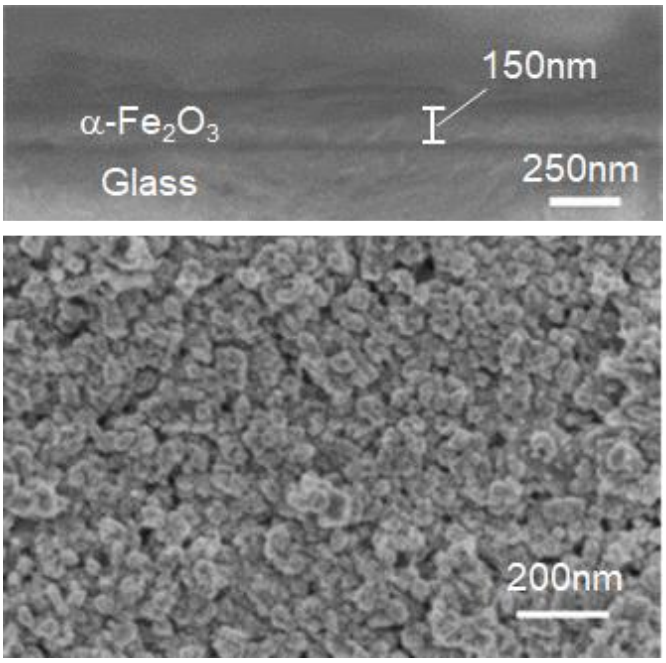

Figure 2.13. Cross-section and surface SEM images of SMART-derived α-Fe_2O_3 on a glass substrate deposited after 90 cycles.

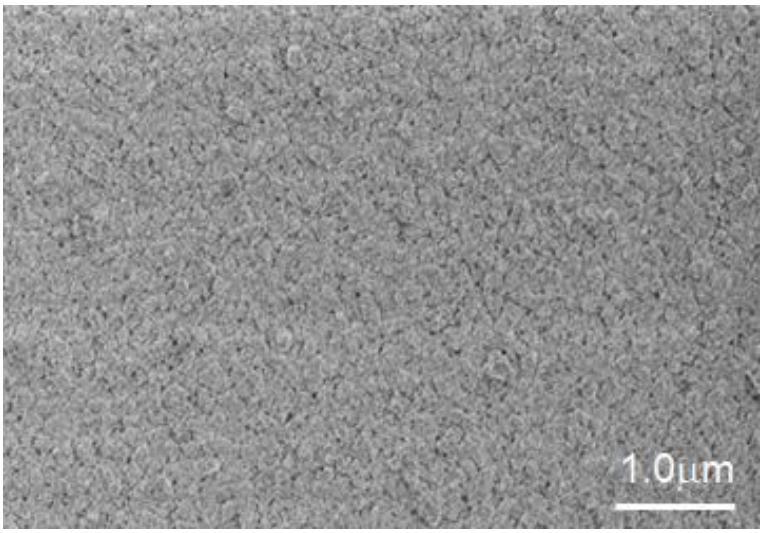

Figure 2.14. Low magnification SEM image of SMART-derived α-Fe_2O_3 layer on a glass substrate after 90 deposition cycles.

2.3.2 Growth rate and mechanism of SMART process.

The growth mechanism was verified by monitoring the change of UV-Vis spectra with an increase in the number of deposition cycles. Figure 2.15 (a) shows a change in the UV-Vis absorption spectra after 1, 3, 5, 10, 15, 20, 25, and 30 cycles on the glass substrate. In general, the absorption gradually intensified with the number of deposition cycles, while the spectral feature, *e.g.*, absorption onset, was not largely changed after at least 3 cycles, indicating that the α-Fe_2O_3 layer was deposited throughout the cycles. Figure 2.15 (b) displays plots of absorption intensity at 400 nm versus the number of deposition cycles. The plots were fitted with lines at a slope of ca. 0.01 per cycle. Note that the absorption coefficient for 90 cycles of deposited α-Fe_2O_3 was 1.12 at 400 nm (Figure 2.16). From this value, the slope was calculated to 0.012 per cycle, which accords well to the slope value obtained from up to 30 cycles. Thus, the UV-Vis absorption data supports that the α-Fe_2O_3 film is deposited in a layer-by-layer manner. The calculated crystallite size, 47.4 nm from the XRD pattern (Figure 2.11), was 28 times larger than the growth rate (*ca.* 1.7 nm). Thus, the Fe^{2+} species in the Stern layer was mainly consumed for crystal growth rather than the heterogeneous nucleation process. It is confirmed that the slope value that fitted with the UV-Vis data was unchanged when the TCO substrate was used as the substrate (Figure 2.15 (b)). This result is reproducible. The thickness of an α-Fe_2O_3 layer on a TCO was observed to approximately 50 nm after 30 deposition cycles (Figure 2.17). This further confirms that the growth rate was about 1.7 nm/cycle.

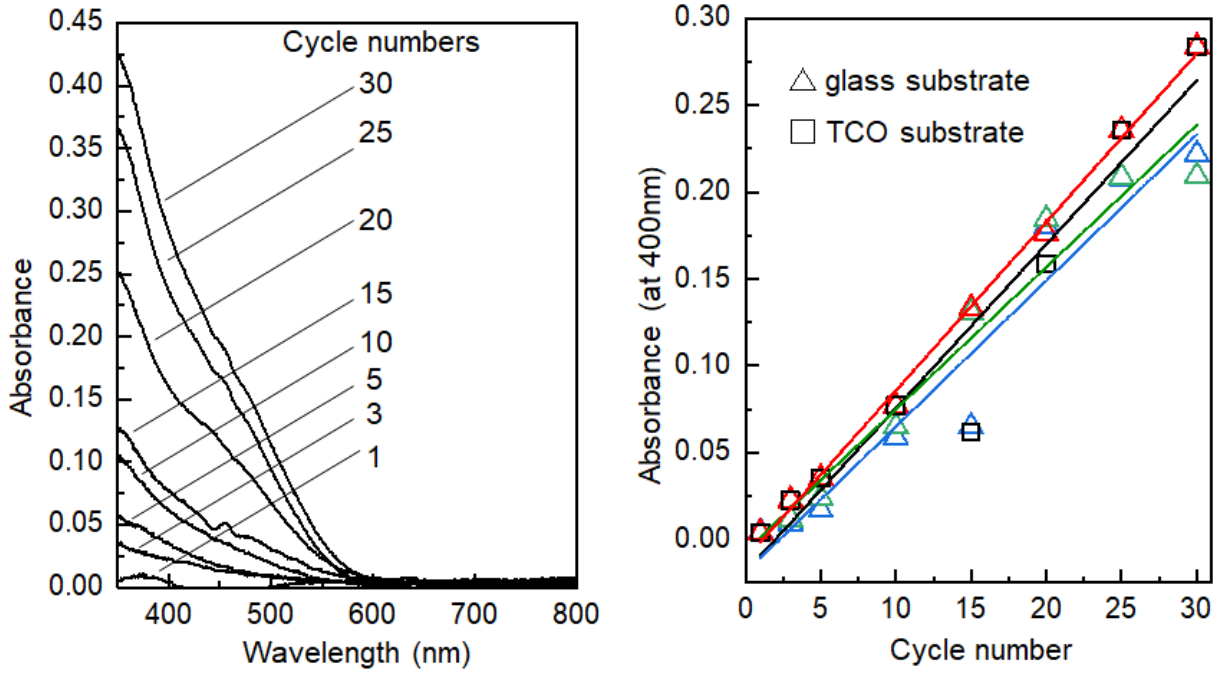

Figure 2.15. (a) UV-Vis spectra of SMART-derived α-Fe_2O_3 obtained after 1, 3, 5, 10, 15, 20, 25, and 30 deposition cycles, (b) plots of absorption intensity at 400 nm versus deposition cycles, where the △ and □ symbols denote the plots from the sample deposited on glass and TCO substrates, respectively.

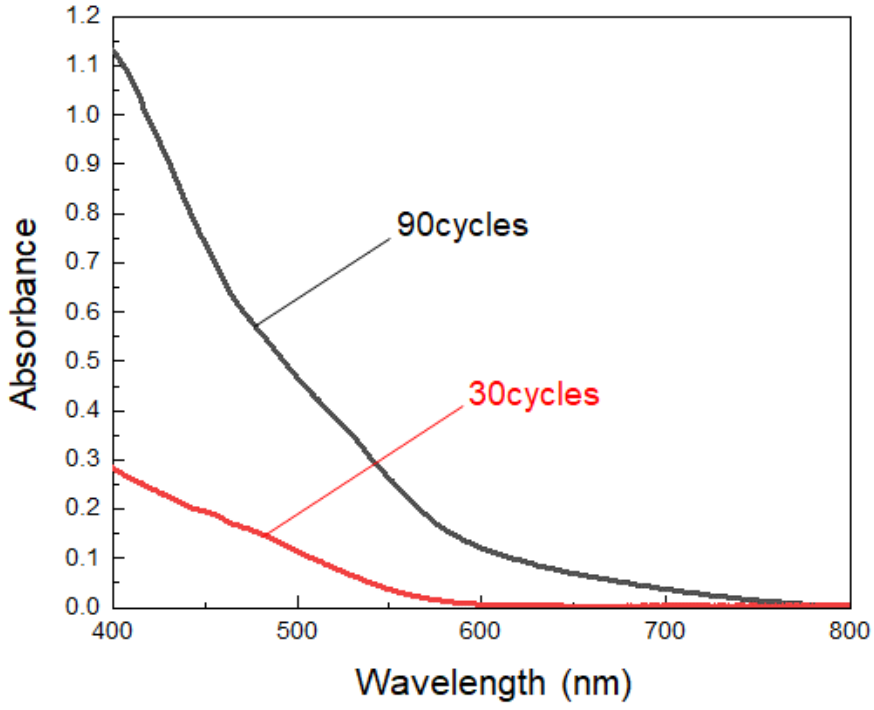

Figure 2.16. UV-vis spectra of SMART-derived α-Fe_2O_3 layer on a glass substrate after 30 and 90 deposition cycles.

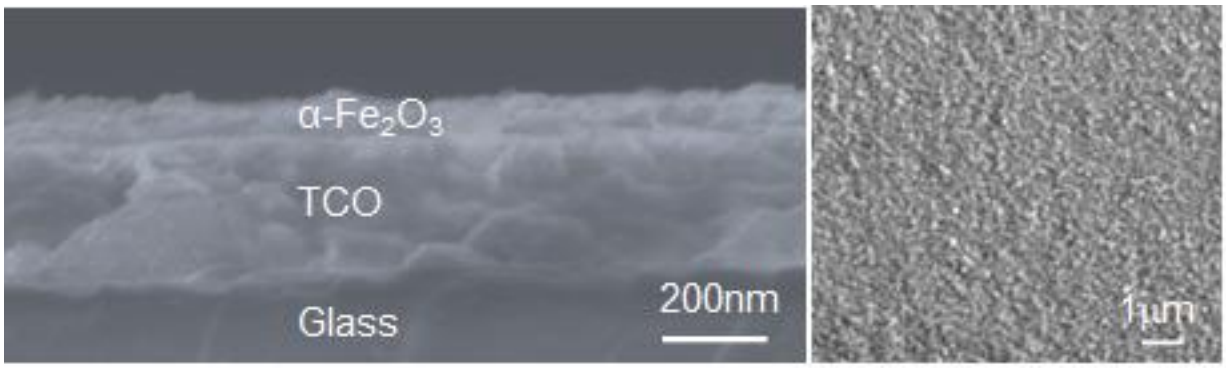

Figure 2.17. SEM images of SMART-derived α-Fe_2O_3 on a TCO substrate deposited after 30 cycles.

X-ray photoemission spectroscopy (XPS) was employed to detect the changes in surface states of the first cycle. Figure 2.18 (a) displays Fe 2p XPS spectra of the deposited layer after the reaction with $FeCl_2$ followed by the rinse step, and one subsequently reacted with the $NaNO_2$ solution followed by a second rinse step. Note that the Sn $3p_{3/2}$ background signal was extracted from the as-obtained data to better understand the Fe 2p spectra (see Figure 2.19).

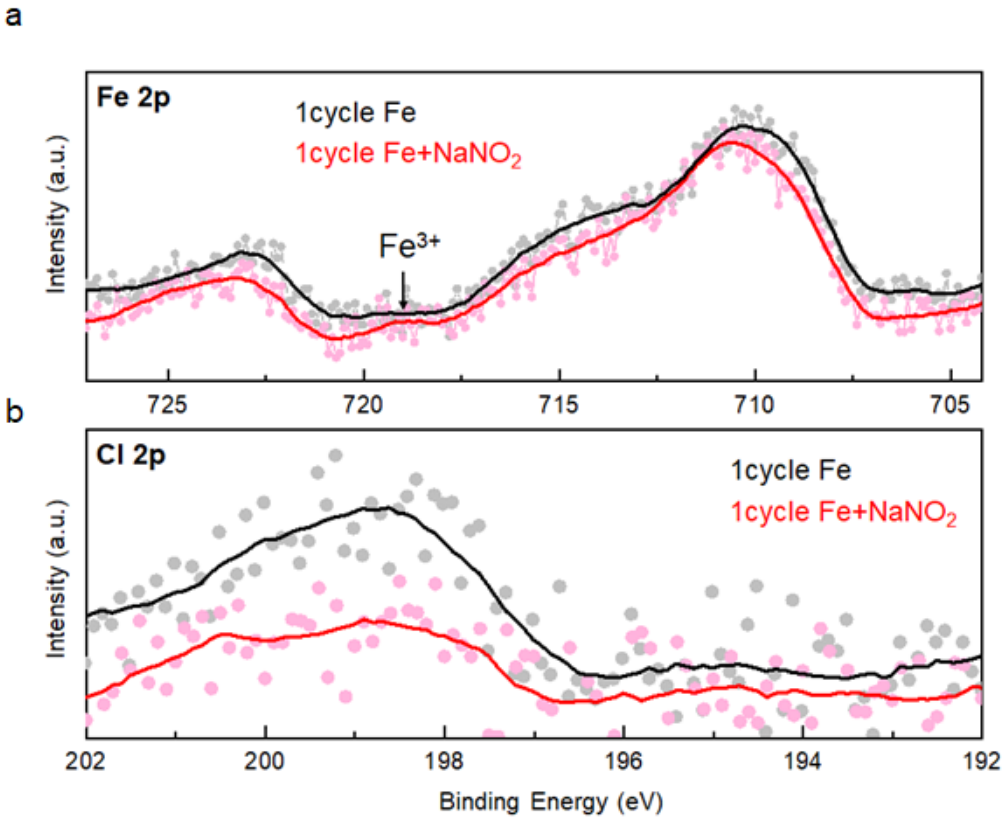

Figure 2.18. (a) Fe 2p and (b) Cl 2p XPS spectra of the deposited layer after the first step (black) and second step (red) in the first deposition cycle.

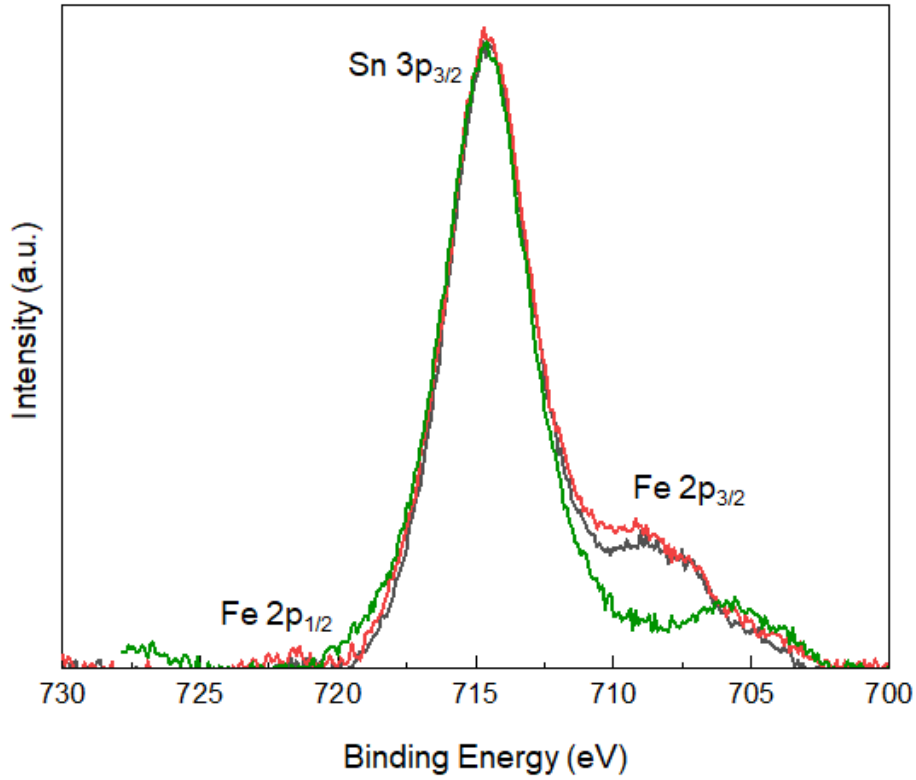

Figure 2.19. As-measured Fe 2p XPS spectra after the first step (black) and second step (red) in the first deposition cycle, and Sn 3p spectra of a bare TCO substrate (green).

The Fe 2p spectra involve multi-components including Fe $2p_{1/2}$, Fe $2p_{3/2}$, and their satellite peaks, while it can be quantitively described that the peaks shifted toward the higher energy side after reaction with $NaNO_2$. Indeed, a peak at around 719 eV, attributable to a Fe $2p_{1/2}$ satellite of Fe^{3+}, was pronounced after the reaction[30-31]. These changes demonstrate that the oxidation of Fe^{2+} occurred by reactions with the $NaNO_2$ solution. Besides, the intensity of the Cl 2p peak (Figure 2.18 (b)) decreased after the second step. This supports the notion that the Cl^- ions involved in the outer layer of the double-layer were replaced by O^{2-} or OH^- species binding with Fe^{3+} after the oxidation step. Thus, all the analytical results support that the α-Fe_2O_3 layer could be deposited, according to the designed SMART concept (Figure 2.5). The direct formation of α-Fe_2O_3 demonstrates that controlling surface redox reactions in the growth process plays a critical role in crystallization.

2.3.3 Electrocatalytic properties of SMART-derived thin films.

Subsequently, the electrochemical and photo-electrochemical catalytic performance of SMART-derived α-Fe_2O_3 for an oxygen evolution reaction (OER) was investigated to find any structure-performance correlations. As is well known, OER is the essence of renewable fuel generation in water electrolysis, and the development of stable, cost-effective, and environmentally-friendly OER catalysts is a key challenge[32-36]. This sheds light on α-Fe_2O_3 as one of the most suitable materials[37-38]. Figure 2.20 (a) shows plots of linear sweep voltammograms (LSV) of an α-Fe_2O_3 deposited TCO substrate after 30 cycles of SMART along with a bare-

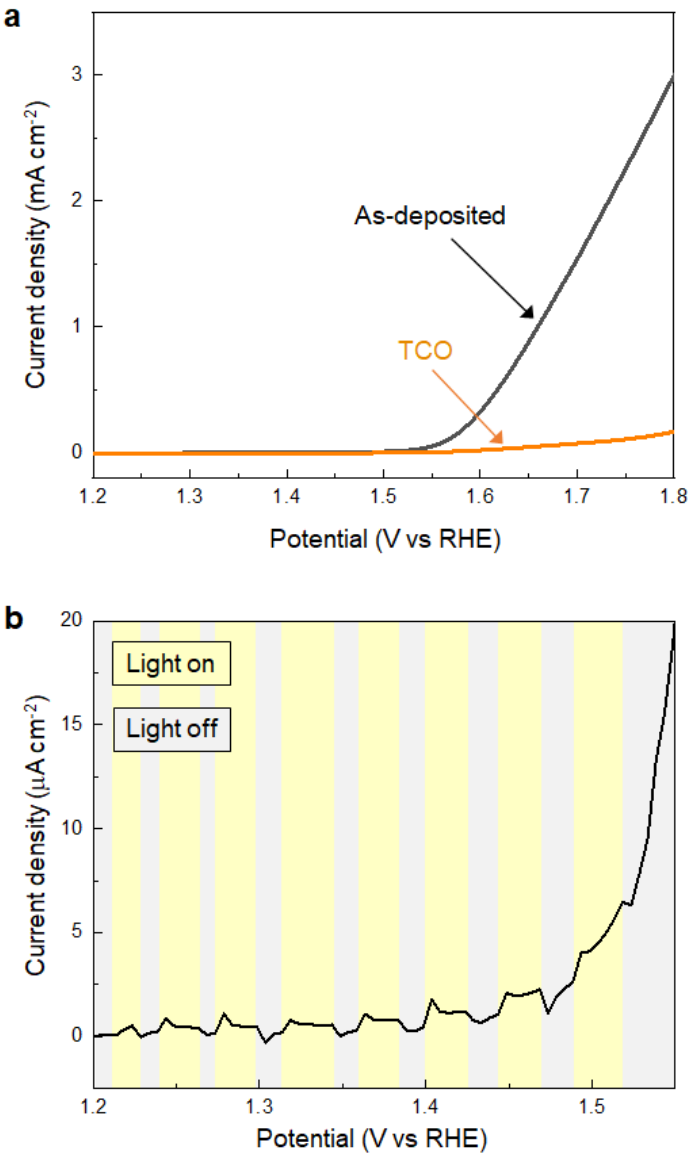

Figure 2.20. (a) LSV curves for SMART-derived α-Fe_2O_3 obtained after 30 deposition cycles on an TCO substrate and bare-TCO. (b) The effects of photoirradiation on the current density for SMART-derived α-Fe_2O_3 obtained after 30 deposition cycles on a TCO substrate.

TCO reference. In this case, the measurements were performed without light irradiation. A bare TCO shows a tiny cathodic current (0.18 mA/cm^2 at 1.8 V), while a current of more than one order of magnitude higher is gained at the same potential after α-Fe_2O_3 deposition. The overpotential is about 390 mV at 0.5 mA/cm^2.

Electrochemical measurements under light-irradiation were also performed to investigate the catalytic activity of photo-electrochemical water oxidation (Figure 2.20 (b)). As a result, a tiny increase of cathodic current in the μA/cm^2 range was observed, which demonstrates that most photogenerated electron/hole pairs were expensed for the recombination pathways rather than for water oxidation. To our knowledge, there has been no report of α-Fe_2O_3-based materials simultaneously exhibiting good electrocatalytic activity (measured without light-irradiation) and photo-electrocatalytic activity (measured with light-irradiation) for water oxidation. This is most probably because they are in a trade-off relationship; namely, defects increase the electron conductivity required for the former catalysis, while they induce recombination pathways for the photogenerated carriers that are avoided for the latter. Considering that SMART was conducted at a low temperature of 75 ºC, a SMART-derived α-Fe_2O_3 layer would be more defective than those synthesized by high-temperature methods, which could be the main reason for the remarkable catalytic activity of SMART-derived α-Fe_2O_3.

Subsequently, the effects of thermal annealing in the air on the electrochemical properties of SMART-derived α-Fe_2O_3 were investigated to understand the correlation between the catalytic activity and local structures in α-Fe_2O_3 layers. Figure 2.21 (a) shows the LSV curves of the SMART-derived α-Fe_2O_3 layer, as-deposited and subsequently annealed at 300 ºC and 500 ºC. After annealing at 300 ºC, the cathodic current density increased slightly. The catalytic activity was significantly enhanced with the overpotential of 370 mV at 0.5 mA/cm^2 after annealing at 500 ºC. It was assumed that the activity would decrease after the annealing in the air due to the elimination of defects. However, the trend of the experimental results was the opposite of our expectations, indicating that the α-Fe_2O_3 layer remained defective after annealing. The photo-response remained negligible after annealing at 500 ºC (Figure 2.21 (b)).

XRD analyses were performed to collect information about the local structure changes of α-Fe_2O_3 layers after annealing (Figure 2.22 (a) and 2.22 (b)). First, no additional peaks emerged after annealing up to 500 ºC, supporting that the as-deposited films were mainly composed of crystalline α-Fe_2O_3. Second, the average crystallite size slightly increased to 54.6 nm from 47.4 nm after annealing at 500 ºC. Third, the *d*-value calculated from the 104 peak position corresponded to 2.719 Å, 2.709 Å, and 2.707 Å for the as-deposited film and ones subsequently annealed at 300 ºC and 500 ºC, respectively, while the d-value obtained from a reference bulk crystalline α-Fe_2O_3 was 2.703 Å (Figure 2.23). Thus, the lattice expansion occurred in as-deposited α-Fe_2O_3, and the lattice shrank to the bulk value after the annealing.

XPS was performed to detect the change in chemical states of the α-Fe_2O_3 after annealing. Figures 2.24 (a)-(d) show Fe 2p and O 1s spectra of SMART-derived α-Fe_2O_3 with and without annealing at 300 ºC and 500 ºC. In the Fe 2p spectra, an Sn $3p_{3/2}$ peak located at 716 eV appeared after annealing at 500 ºC. It was also found that Sn 3d peaks in the wide-scan spectrum were pronounced after the annealing (Figure 2.25). Thus, Sn^{4+} ions, involved in the conducting substrate, would be thermally diffused in the α-Fe_2O_3 lattice. In fact, this phenomenon can be found in the literatures[39-41]. Sn^{4+} exhibits a similar ionic radius and Pauling

electronegativity to Fe^{3+} ions, which facilitates the substitution of Fe^{3+} to Sn^{4+} in α-Fe_2O_3. Importantly, Sn^{4+}-doping has been found to be an effective approach for tailoring the electronic properties of α-Fe_2O_3[42-44]. In the present case, the catalytic activity was likely enhanced by an increased electron conductivity by Sn^{4+}-doping[44]. Two binding energies of O 1s (529.5 eV and 531.0 eV) were assigned to the O^{2-} and OH^-, respectively[45-46]. The ratio of OH^-/O^{2-} decreased after annealing at 300 ºC. Thus, it was suggested that the observed lattice expansion in the as-deposited α-Fe_2O_3 layer was caused by the OH species[47-48]. Finally, the intensity of the Cl 2p was quite weak in the as-deposited sample. The peak was almost undetectable after annealing at 300 ºC, excluding the significant contributions of Cl^- to change the catalytic activity upon annealing (Figure 2.26).

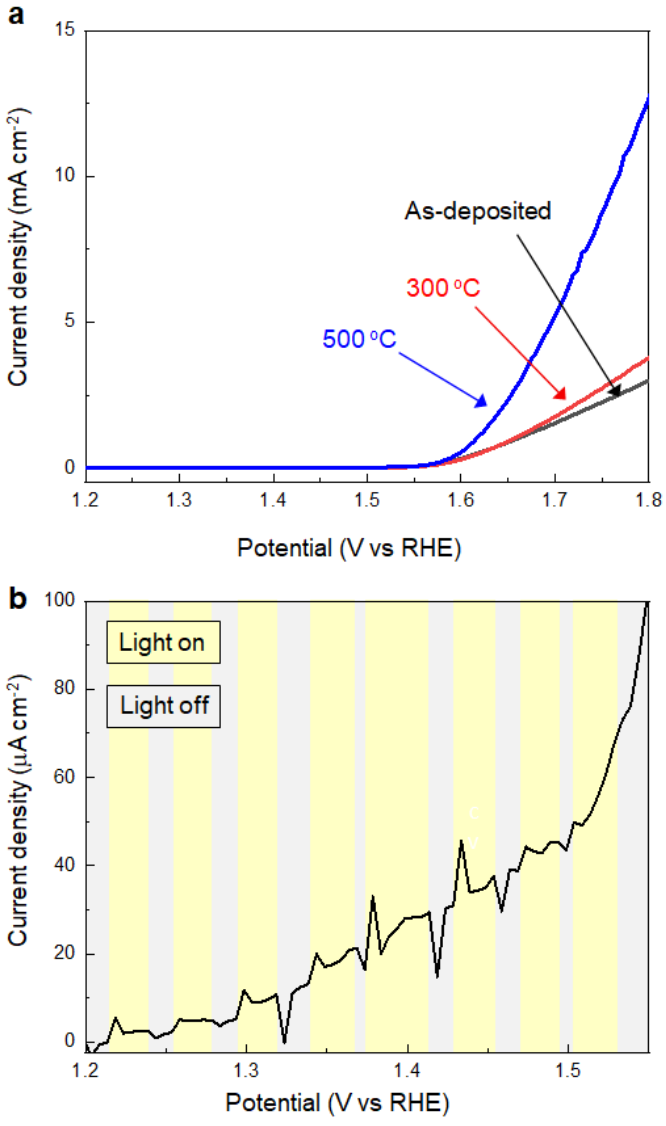

Figure 2.21. (a) LSV curves for SMART-derived α-Fe_2O_3 obtained after 30 deposition cycles on an TCO substrate; as-deposited, and subsequently annealed at 300 ºC and 500 ºC. (b) The effects of photoirradiation on the current density for SMART-derived α-Fe_2O_3 obtained after 30 deposition cycles on an TCO substrate (annealed 500 ºC).

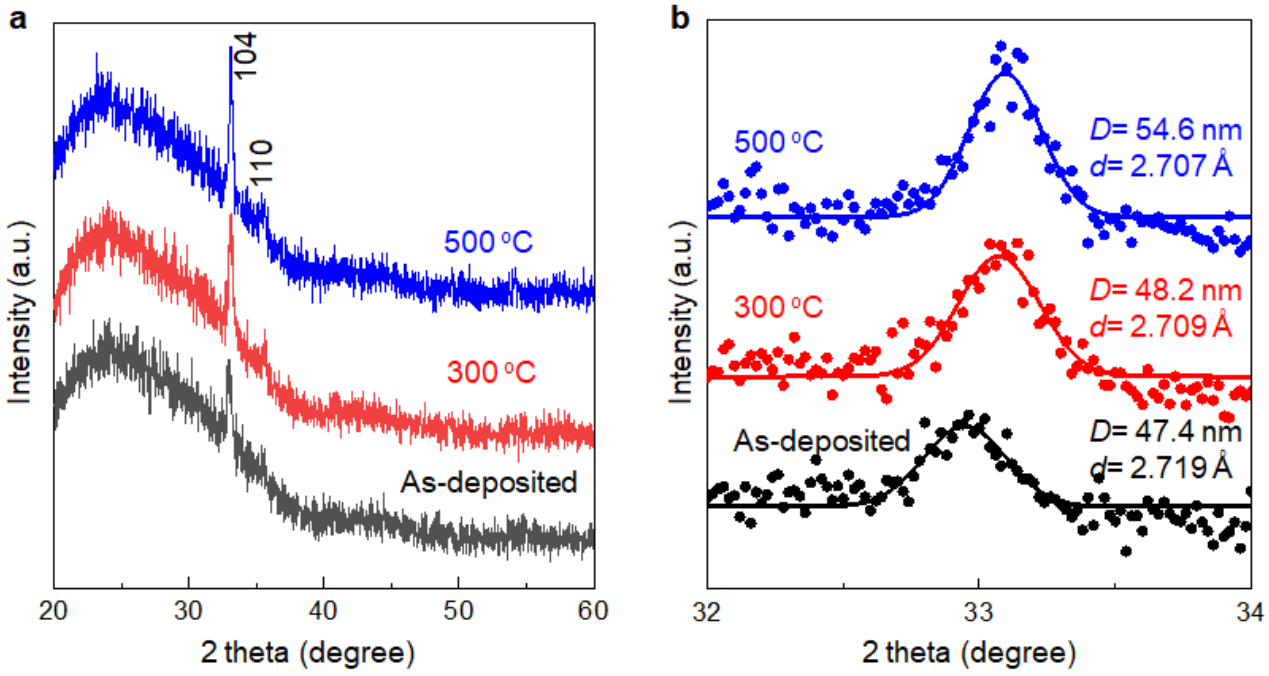

Figure 2.22. (a) Total and (b) Selected angle XRD patterns of the SMART-derived α-Fe_2O_3 deposited on a glass substrate.

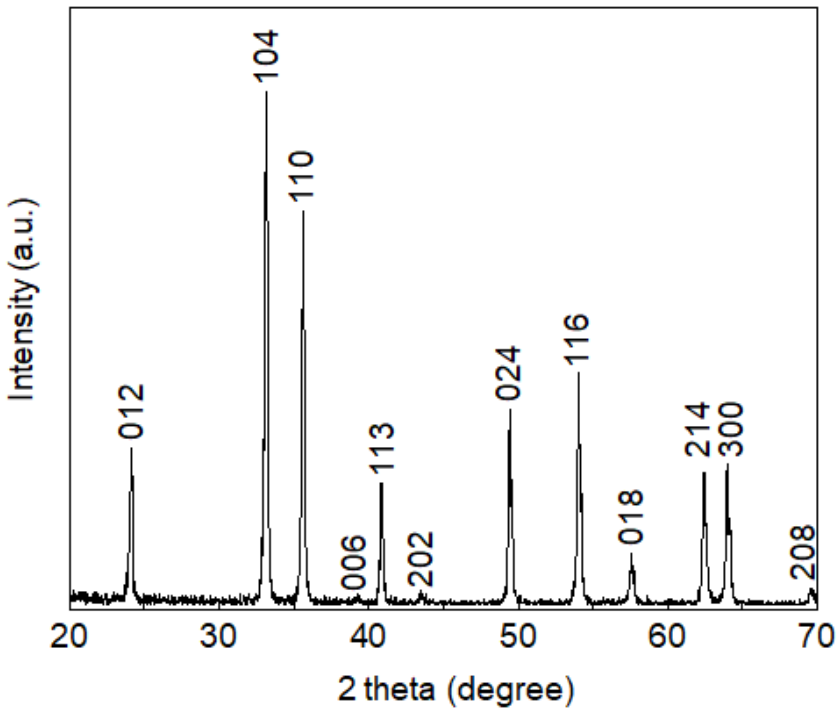

Figure 2.23. XRD pattern of reference α-Fe_2O_3 powder.

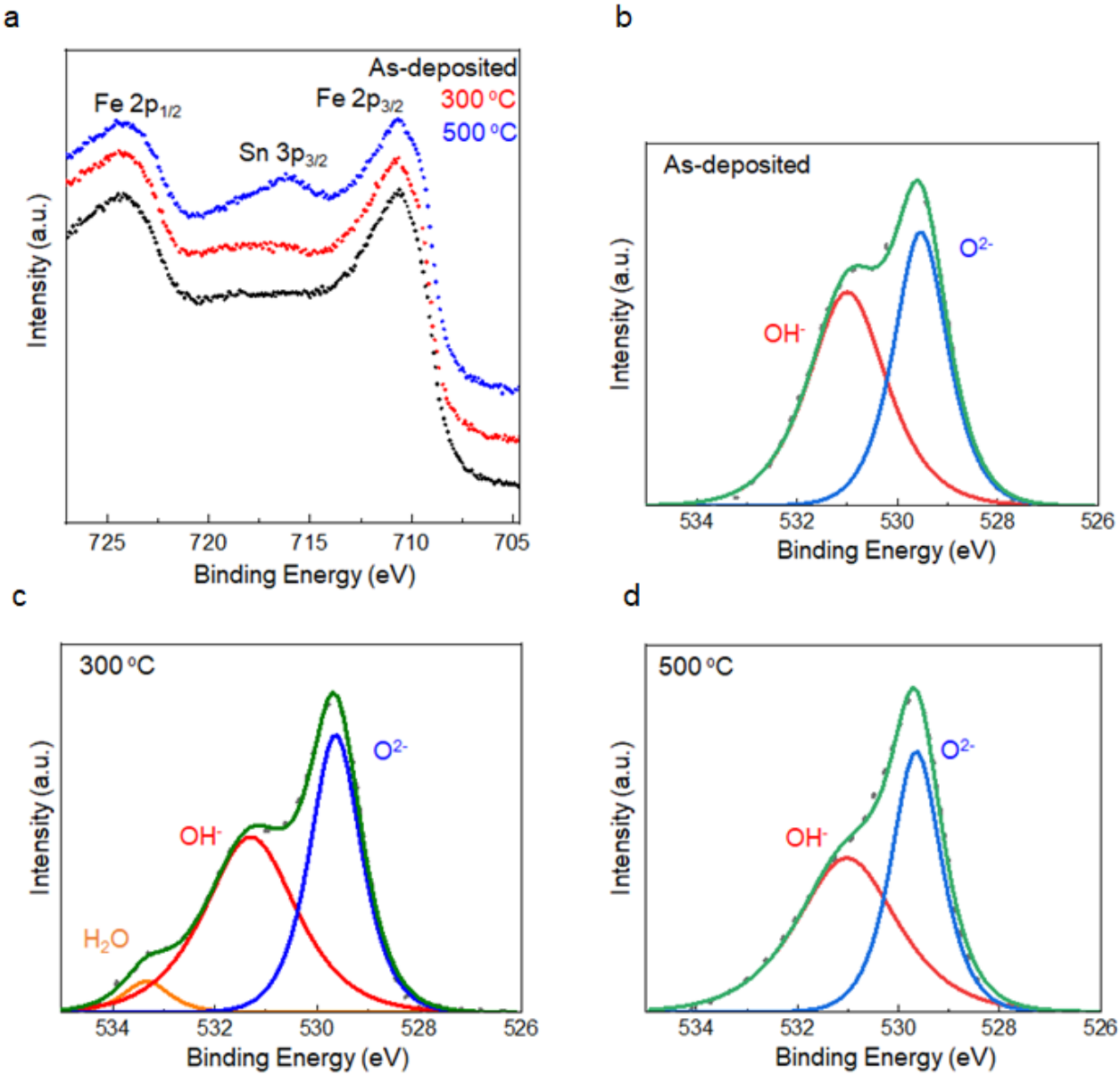

Figure 2.24. (a) Fe 2p XPS spectra of the SMART-derived α-Fe_2O_3 deposited on a TCO substrate, as-deposited, and subsequently annealed at 300 °C and 500 °C. O 1s XPS spectra of the SMART-derived α-Fe_2O_3 deposited on a TCO substrate, (b) as-deposited, and subsequently annealed at (c) 300 °C and (d) 500 °C.

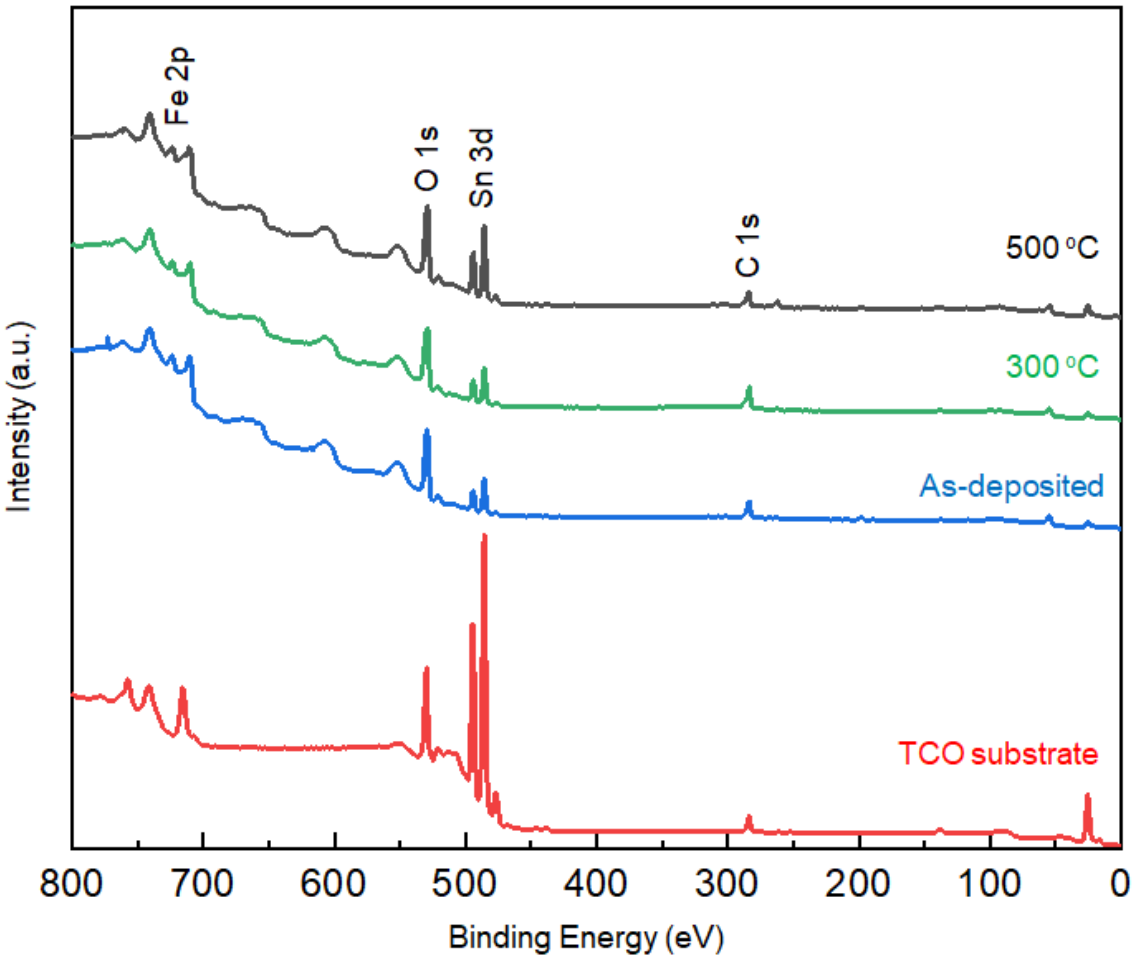

Figure 2.25. Wide-scan XPS spectrum of the SMART-derived α-Fe_2O_3 deposited on an TCO substrate, as-deposited, and subsequently annealed at 300 °C and 500 °C. Wide-scan XPS spectrum of TCO substrate is shown as a reference.

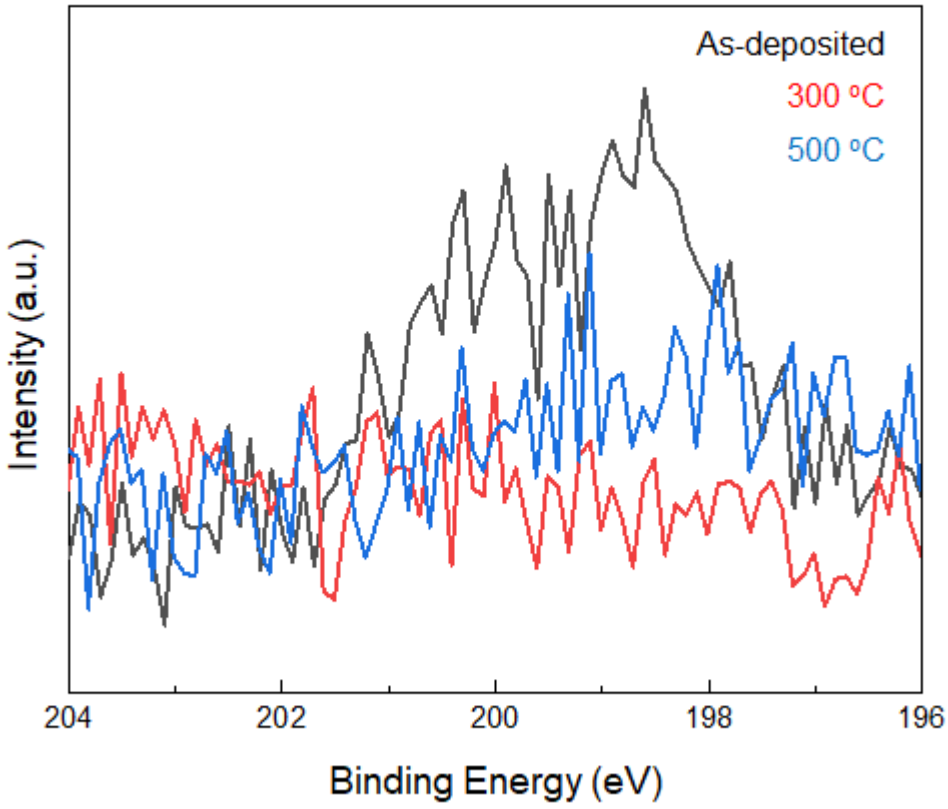

Figure 2.26. Cl 2p spectra of the SMART-derived α-Fe_2O_3 deposited on a TCO substrate, as-deposited, and after annealing at 300 °C and 500 °C.

2.3.4 Enhanced catalytic activity at $Ni(OH)_2$/α-Fe_2O_3 heterointerface.

It was revealed that defect-engineering by annealing is effective in enhancing the electrocatalytic activity of α-Fe_2O_3. Here, the alternative reaction concept was further extended to tailor the catalytic activity, where the $Ni(OH)_2$ layer was decorated onto the surface of the α-Fe_2O_3 film after annealing at 500 °C. The $Ni(OH)_2$ layer was deposited SILAR method[18, 49], referred to as the most relevant deposition technique to SMART. In SILAR, metal ions were adsorbed onto the surface followed by rinsing with water. In the next step, metal cations reacted with an alkaline solution to form a metal hydroxide layer via classical precipitation reactions (eq. 2.1). In fact, this attempt significantly improved the OER activity; as shown in Figure 2.27 (a), the overpotential was lowered to 250 mV at 0.5 mA/cm^2 after the $Ni(OH)_2$-modification. The overpotential at the same current density was ca. 50 mV lower than those from the best α-Fe_2O_3-based catalysts, Ni- or Zn-doped α-Fe_2O_3, reported so far[37]. No degradation of catalytic performance was observed after 100 scans, which indicated the high catalytic durability. The $Ni(OH)_2$-modified α-Fe_2O_3 showed better catalytic activity than SILAR-derived $Ni(OH)_2$, where the overpotential of a $Ni(OH)_2$ layer obtained after 30 deposition cycles was 320 mV at 0.5 mA/cm^2. Figures 2.27 (b) and 2.27 (c) show the Fe 2p and Ni 2p XPS spectra of $Ni(OH)_2$-

modified α-Fe_2O_3, respectively. There is no remarkable change in the features of the Fe 2p spectra, indicating that the Fe-O-Fe framework containing oxygen vacancies was not altered by $Ni(OH)_2$-modification.

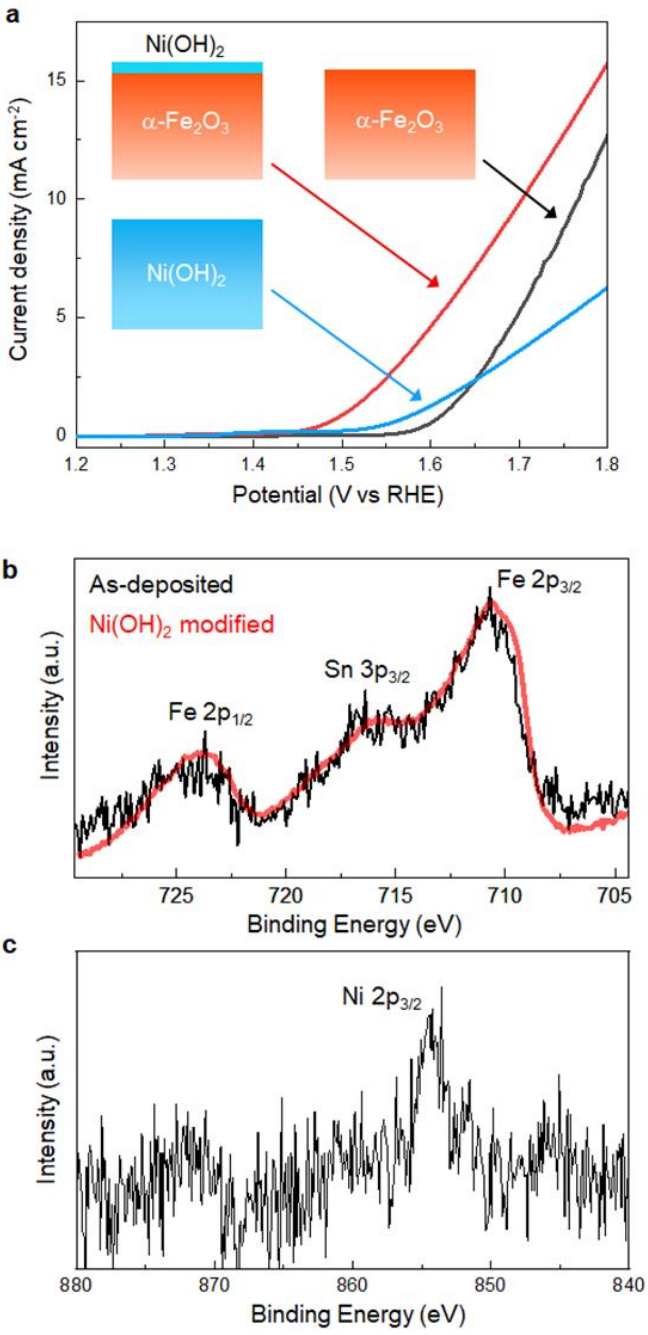

Figure 2.27. (a) LSV-curves of the SMART-derived α-Fe_2O_3 (annealed at 500 °C) before/after $Ni(OH)_2$ surface-modification and SILAR-derived $Ni(OH)_2$ (b) Fe 2p and (c) Ni 2p XPS spectra of the SMART-derived α-Fe_2O_3 (annealed at 500 °C) after $Ni(OH)_2$ surface modification.

Based on the relative peak intensity of the Ni 2p and Fe 2p spectra, the Ni: Fe atomic ratio is approximately 1:3. Considering the analytical depth of the XPS (ca. 4 nm), the thickness of the $Ni(OH)_2$ layer is estimated to be 1 nm. Besides, SEM-EDX analysis revealed that Ni signal was homogenously detected on the whole surface of the α-Fe_2O_3 layer, while there was no morphological change on the surface (Figure 2.28).

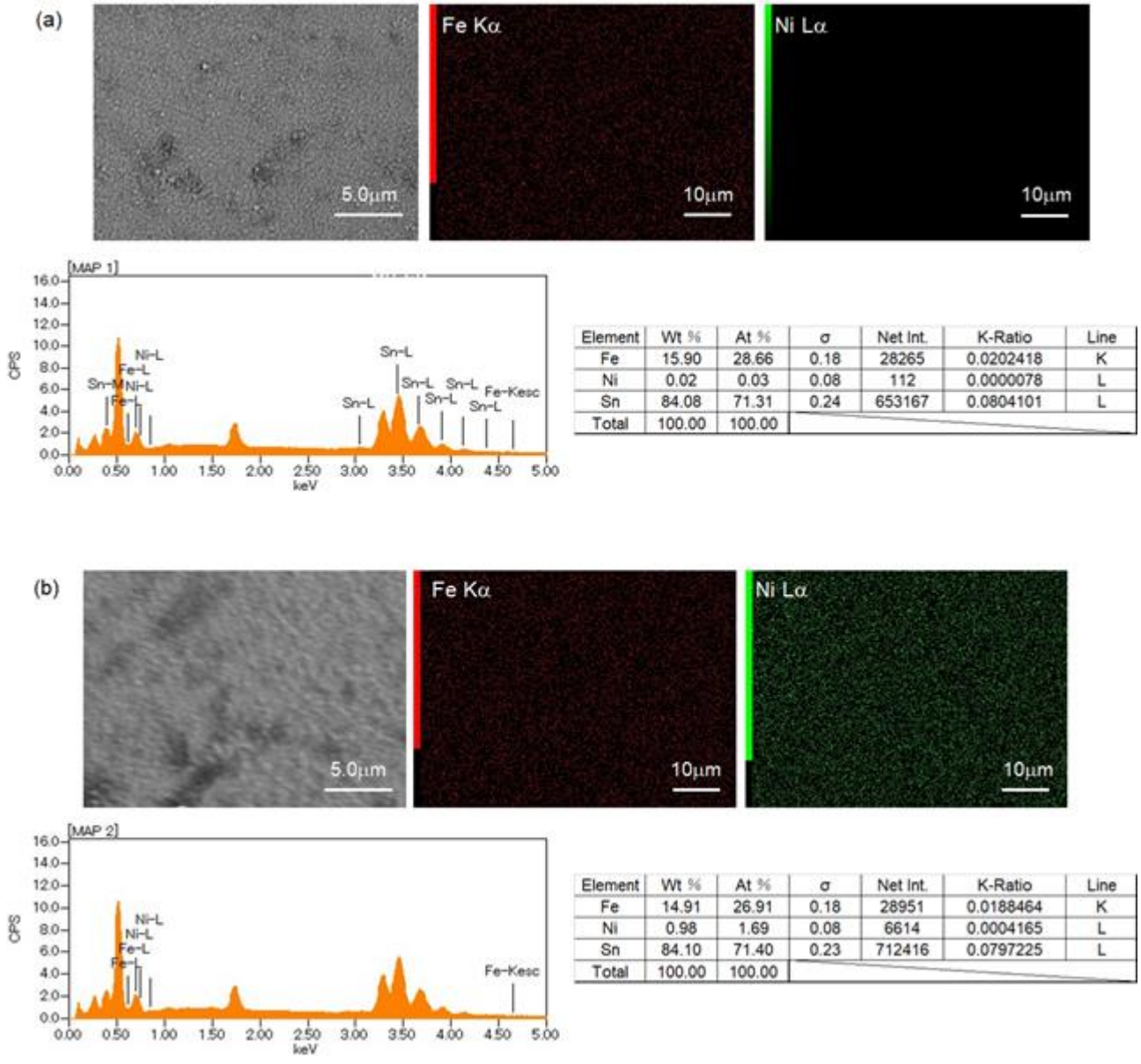

Figure 2.28. SEM images and Fe/Ni distributions obtained by EDS elemental mapping of SMART-derived α-Fe_2O_3 (a) before and (b) after $Ni(OH)_2$ surface-modification.

In addition, no additional reflection peaks from Ni-based phases were detected in the XRD pattern of the $Ni(OH)_2$-modified sample(Figure 2.29). This indicates that particulate $Ni(OH)_2$ was not formed, while $Ni(OH)_2$ would be uniformly formed on the α-Fe_2O_3 surface. These results support that catalytic activity was modified through the formation of $Ni(OH)_2$/α-Fe_2O_3 heterointerface.

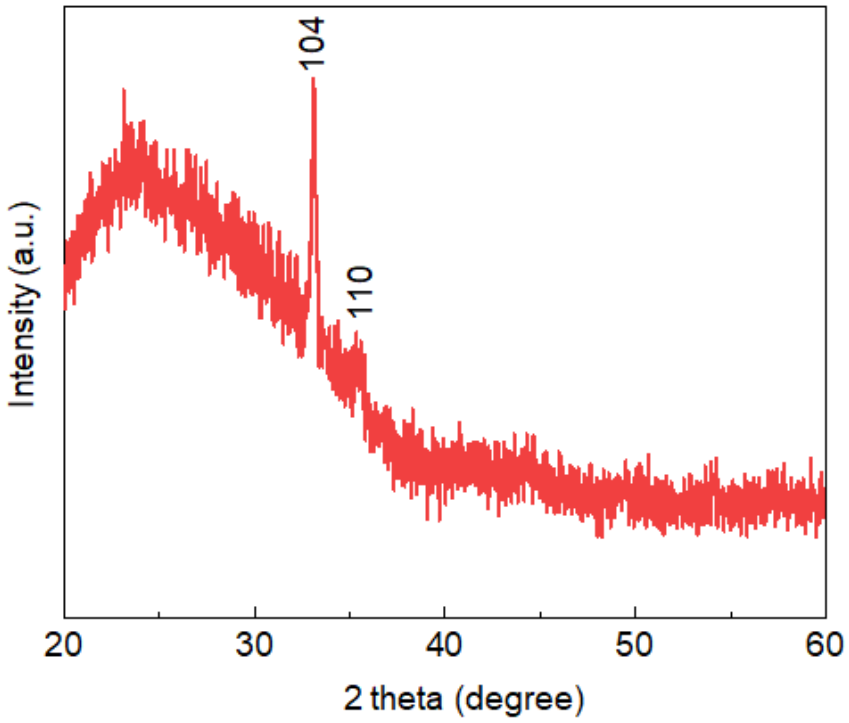

Figure 2.29. XRD pattern of the SMART-derived α-Fe_2O_3 (annealed at 500 ºC) after $Ni(OH)_2$ surface-modification. Note that α-Fe_2O_3 layer was deposited after 90 cycles.

Finally, for perspective, it was proposed that the alternative reaction process could provide a platform to create artificial two-dimensional (2D) heterostructures. 2D heterostructures such as $BaTiO_3$/$SrTiO_3$ superlattice were initially fabricated by a vacuum process[50], and recently, hetero-assembly of 2D nanomaterials such as graphene, as well as 2D transition metal dichalcogenides and 2D oxides have attracted considerable attention for tuning functionalities by interface coupling[51-52]. Although alternative reaction, including SILARs and solution-ALD[53], has only been employed for the deposition of inorganic layers with single components, the layer-by-layer deposition principle is applicable to produce such 2D heterostructures. The $Ni(OH)_2$/ α-Fe_2O_3 heterointerface with excellent OER activity, found in the present study, partially demonstrate the above strategy. However, a true understanding of the enhancement of the heterointerface remains challenging because of the complex nature of the surface system, and thus is beyond the scope of this current study. For example, it was found that enhancement of OER activity was less significant, when $Ni(OH)_2$ was deposited on the as-deposited α-Fe_2O_3 layer (Figure 2.30). Presently, it is expected that the periodical 2D heterostructures, such as alternately stacked $Ni(OH)_2$/ α-Fe_2O_3 layers, would serve rich chemistry, affording superior catalytic activity.

This will be the target of our next study.

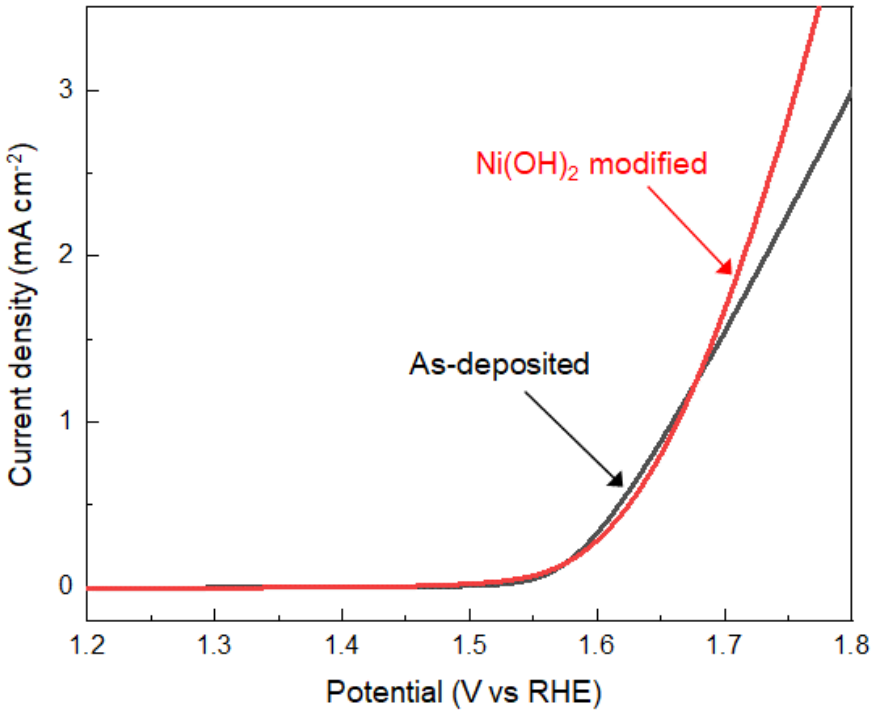

Figure 2.30. LSV-curves of the SMART-derived α-Fe_2O_3 before/after $Ni(OH)_2$ surface-modification.

2.4 Conclusion

In conclusion, SMART was established for the direct solution deposition of α-Fe_2O_3 layers on oxide substrates. This method yielded an α-Fe_2O_3 layer with a 150 nm thickness and a crystalline size of 47.4 nm after 90 deposition cycles. The growth rate was ca. 1.7 nm per deposition cycle, in which Fe^{2+} cations in a Stern layer were oxidized by $NaNO_2$ to form Fe^{3+} followed by consumption by crystal growth. Thus, the designed reaction route for the α-Fe_2O_3 layer was experientially demonstrated. OH^- species were introduced in the lattice of α-Fe_2O_3 crystallites, probably associating with the low-temperature aqueous process. The defective feature of SMART-derived α-Fe_2O_3 activated and deactivated electrochemical and photoelectrochemical activity for water oxidation, respectively. The annealing in air introduced the Sn^{4+} ions in the α-Fe_2O_3 layer by the thermal diffusion from the substrate, which enhanced the electrocatalytic activity. Finally, it was found that $Ni(OH)_2$/ α-Fe_2O_3 heterointerface provided excellent OER activity, which would be crucial to developing stable, cost-effective, and environmentally-friendly OER catalysts.

Most part of this chapter has been published in Nanoscale Advances, 2, 3933, 2020[54].
DOI: 10.1039/d0na00345j

References

1. Tatsuma, T.; Saitoh, S.; Ohko, Y.; Fujishima, A., TiO_2−WO_3 Photoelectrochemical Anticorrosion System with an Energy Storage Ability. *Chemistry of Materials* **2001,** *13* (9), 2838-2842.

2. Smith, R. D. L.; Prévot, M. S.; Fagan, R. D.; Trudel, S.; Berlinguette, C. P., Water Oxidation Catalysis: Electrocatalytic Response to Metal Stoichiometry in Amorphous Metal Oxide Films Containing Iron, Cobalt, and Nickel. *Journal of the American Chemical Society* **2013,** *135* (31), 11580-11586.

3. Zhang, S.; Zhang, P.; Wang, Y.; Ma, Y.; Zhong, J.; Sun, X., Facile Fabrication of a Well-Ordered Porous Cu-Doped SnO_2 Thin Film for H2S Sensing. *ACS Applied Materials & Interfaces* **2014,** *6* (17), 14975-14980.

4. Tong, S.; Ma, B.; Narayanan, M.; Liu, S.; Koritala, R.; Balachandran, U.; Shi, D., Lead Lanthanum Zirconate Titanate Ceramic Thin Films for Energy Storage. *ACS Applied Materials & Interfaces* **2013,** *5* (4), 1474-1480.

5. Pandya, S.; Wilbur, J.; Kim, J.; Gao, R.; Dasgupta, A.; Dames, C.; Martin, L. W., Pyroelectric energy conversion with large energy and power density in relaxor ferroelectric thin films. *Nature Materials* **2018,** *17* (5), 432-438.

6. Wu, J.; Fu, S.; Zhang, X.; Wu, C.; Wang, A.; Li, C.; Shan, G.; Liu, Y., Bidirectional Photochromism via Anchoring of Carbon Dots to TiO_2 Porous Films. *ACS Applied Materials & Interfaces* **2020,** *12* (5), 6262-6267.

7. Kim, M.-G.; Kanatzidis, M. G.; Facchetti, A.; Marks, T. J., Low-temperature fabrication of high-performance metal oxide thin-film electronics via combustion processing. *Nature Materials* **2011,** *10* (5), 382-388.

8. Alotaibi, A. M.; Sathasivam, S.; Williamson, B. A. D.; Kafizas, A.; Sotelo-Vazquez, C.; Taylor, A.; Scanlon, D. O.; Parkin, I. P., Chemical Vapor Deposition of Photocatalytically Active Pure Brookite TiO_2 Thin Films. *Chemistry of Materials* **2018,** *30* (4), 1353-1361.

9. Serrano, A.; Rubio-Zuazo, J.; López-Sánchez, J.; Arnay, I.; Salas-Colera, E.; Castro, G. R., Stabilization of Epitaxial α-Fe_2O_3 Thin Films Grown by Pulsed Laser Deposition on Oxide Substrates. *The Journal of Physical Chemistry C* **2018,** *122* (28), 16042-16047.

10. Kment, S.; Schmuki, P.; Hubicka, Z.; Machala, L.; Kirchgeorg, R.; Liu, N.; Wang, L.; Lee, K.; Olejnicek, J.; Cada, M.; Gregora, I.; Zboril, R., Photoanodes with Fully Controllable Texture: The Enhanced Water Splitting Efficiency of Thin Hematite Films Exhibiting Solely (110) Crystal Orientation. *ACS Nano* **2015,** *9* (7), 7113-7123.

11. Sun, Y.; Seo, J. H.; Takacs, C. J.; Seifter, J.; Heeger, A. J., Inverted Polymer Solar Cells Integrated with a Low-Temperature-Annealed Sol-Gel-Derived ZnO Film as an Electron Transport Layer. *Advanced Materials* **2011,** *23* (14), 1679-1683.

12. Guerin, V. M.; Magne, C.; Pauporté, T.; Le Bahers, T.; Rathousky, J., Electrodeposited Nanoporous versus Nanoparticulate ZnO Films of Similar Roughness for Dye-Sensitized Solar Cell Applications. *ACS Applied Materials & Interfaces* **2010,** *2* (12), 3677-3685.

13. Shi, Z.; Walker, A. V., Chemical Bath Deposition of ZnO on Functionalized Self-Assembled Monolayers: Selective Deposition and Control of Deposit Morphology. *Langmuir* **2015,** *31* (4), 1421-1428.

14. Shin, S. S.; Yang, W. S.; Noh, J. H.; Suk, J. H.; Jeon, N. J.; Park, J. H.; Kim, J. S.; Seong, W. M.; Seok, S. I., High-performance flexible perovskite solar cells exploiting Zn_2SnO_4 prepared in solution below 100 °C. *Nature Communications* **2015,** *6* (1), 7410.

15. Peiró, A. M.; Peral, J.; Domingo, C.; Domènech, X.; Ayllón, J. A., Low-Temperature Deposition of TiO_2 Thin Films with Photocatalytic Activity from Colloidal Anatase Aqueous Solutions. *Chemistry of Materials* **2001,** *13* (8), 2567-2573.

16. Stubhan, T.; Li, N.; Luechinger, N. A.; Halim, S. C.; Matt, G. J.; Brabec, C. J., High Fill Factor Polymer Solar Cells Incorporating a Low Temperature Solution Processed WO_3 Hole Extraction Layer. *Advanced Energy Materials* **2012,** *2* (12), 1433-1438.

17. Shirahata, N.; Shin, W.; Murayama, N.; Hozumi, A.; Yokogawa, Y.; Kameyama, T.; Masuda, Y.; Koumoto, K., Reliable Monolayer-Template Patterning of SnO_2 Thin Films from Aqueous Solution and Their Hydrogen-Sensing Properties. *Advanced Functional Materials* **2004,** *14* (6), 580-588.

18. Niesen, T. P.; De Guire, M. R., Review: deposition of ceramic thin films at low temperatures from aqueous solutions. *Solid State Ionics* **2002,** *151* (1), 61-68.

19. Tokudome, Y.; Fujita, K.; Nakanishi, K.; Miura, K.; Hirao, K., Synthesis of Monolithic Al_2O_3 with Well-Defined Macropores and Mesostructured Skeletons via the Sol−Gel Process Accompanied by Phase Separation. *Chemistry of Materials* **2007,** *19* (14), 3393-3398.

20. Chang, S.-m.; Doong, R.-a., Chemical-Composition-Dependent Metastability of Tetragonal ZrO_2 in Sol−Gel-Derived Films under Different Calcination Conditions. *Chemistry of Materials* **2005,** *17* (19), 4837-4844.

21. LaGrow, A. P.; Besenhard, M. O.; Hodzic, A.; Sergides, A.; Bogart, L. K.; Gavriilidis, A.; Thanh, N. T. K., Unravelling the growth mechanism of the co-precipitation of iron oxide nanoparticles with the aid of synchrotron X-Ray diffraction in solution. *Nanoscale* **2019,** *11* (14), 6620-6628.

22. Crystal Structure. In *The Iron Oxides*, 2003; pp 9-38.

23. Li, B.; Chen, J.; Han, L.; Bai, Y.; Fan, Q.; Wu, C.; Wang, X.; Lee, M.; Xin, H. L.; Han, Z.; Yin, Y., Ligand-Assisted Solid-State Transformation of Nanoparticles. *Chemistry of Materials* **2020,** *32* (7), 3271-3277.

24. Taniguchi, A.; Taniguchi, T.; Wagata, H.; Katsumata, K.-i.; Okada, K.; Matsushita, N., Liquid-phase atomic layer deposition of crystalline hematite without post-growth annealing. *CrystEngComm* **2019,** *21* (28), 4184-4191.

25. Momma, K.; Izumi, F., VESTA 3 for three-dimensional visualization of crystal, volumetric and morphology data. *Journal of Applied Crystallography* **2011,** *44* (6), 1272-1276.

26. Holzwarth, U.; Gibson, N., The Scherrer equation versus the 'Debye-Scherrer equation'. *Nature Nanotechnology* **2011,** *6* (9), 534-534.

27. Chamritski, I.; Burns, G., Infrared- and Raman-Active Phonons of Magnetite, Maghemite, and Hematite: A Computer Simulation and Spectroscopic Study. *The Journal of Physical Chemistry B* **2005,** *109* (11), 4965-4968.

28. de Faria, D. L. A.; Venâncio Silva, S.; de Oliveira, M. T., Raman microspectroscopy of some iron oxides and oxyhydroxides. *Journal of Raman Spectroscopy* **1997,** *28* (11), 873-878.

29. Jiang, X.; Zhang, Z.; Mei, J.; Han, D.; Xie, M.; Wang, F.; Xie, E.; Han, W., Carbon quantum dots based charge bridge between photoanode and electrocatalysts for efficiency water oxidation. *Electrochimica Acta* **2018,** *273*, 208-215.
30. Cho, E. S.; Kang, M. J.; Kang, Y. S., Enhanced photocurrent density of hematite thin films on FTO substrates: effect of post-annealing temperature. *Physical Chemistry Chemical Physics* **2015,** *17* (24), 16145-16150.
31. Herrmann-Geppert, I.; Bogdanoff, P.; Radnik, J.; Fengler, S.; Dittrich, T.; Fiechter, S., Surface aspects of sol–gel derived hematite films for the photoelectrochemical oxidation of water. *Physical Chemistry Chemical Physics* **2013,** *15* (5), 1389-1398.
32. Wu, Z.-P.; Lu, X. F.; Zang, S.-Q.; Lou, X. W., Non-Noble-Metal-Based Electrocatalysts toward the Oxygen Evolution Reaction. *Advanced Functional Materials* **2020,** *30* (15), 1910274.
33. Lv, L.; Yang, Z.; Chen, K.; Wang, C.; Xiong, Y., 2D Layered Double Hydroxides for Oxygen Evolution Reaction: From Fundamental Design to Application. *Advanced Energy Materials* **2019,** *9* (17), 1803358.
34. Shi, Q.; Zhu, C.; Du, D.; Lin, Y., Robust noble metal-based electrocatalysts for oxygen evolution reaction. *Chemical Society Reviews* **2019,** *48* (12), 3181-3192.
35. Gonçalves, J. M.; Ireno da Silva, M.; Angnes, L.; Araki, K., Vanadium-containing electro and photocatalysts for the oxygen evolution reaction: a review. *Journal of Materials Chemistry A* **2020,** *8* (5), 2171-2206.
36. Zhang, T.; Zhu, Y.; Lee, J. Y., Unconventional noble metal-free catalysts for oxygen evolution in aqueous systems. *Journal of Materials Chemistry A* **2018,** *6* (18), 8147-8158.
37. Nguyën, H. C.; Garcés-Pineda, F. A.; de Fez-Febré, M.; Galán-Mascarós, J. R.; López, N., Non-redox doping boosts oxygen evolution electrocatalysis on hematite. *Chemical Science* **2020,** *11* (9), 2464-2471.
38. Wu, H.; Yang, T.; Du, Y.; Shen, L.; Ho, G. W., Identification of Facet-Governing Reactivity in Hematite for Oxygen Evolution. *Advanced Materials* **2018,** *30* (52), 1804341.
39. Sivula, K.; Zboril, R.; Le Formal, F.; Robert, R.; Weidenkaff, A.; Tucek, J.; Frydrych, J.; Grätzel, M., Photoelectrochemical Water Splitting with Mesoporous Hematite Prepared by a Solution-Based Colloidal Approach. *Journal of the American Chemical Society* **2010,** *132* (21), 7436-7444.
40. Ling, Y.; Wang, G.; Wheeler, D. A.; Zhang, J. Z.; Li, Y., Sn-Doped Hematite Nanostructures for Photoelectrochemical Water Splitting. *Nano Letters* **2011,** *11* (5), 2119-2125.
41. Li, M.; Yang, Y.; Ling, Y.; Qiu, W.; Wang, F.; Liu, T.; Song, Y.; Liu, X.; Fang, P.; Tong, Y.; Li, Y., Morphology and Doping Engineering of Sn-Doped Hematite Nanowire Photoanodes. *Nano Letters* **2017,** *17* (4), 2490-2495.
42. Xi, L.; Chiam, S. Y.; Mak, W. F.; Tran, P. D.; Barber, J.; Loo, S. C. J.; Wong, L. H., A novel strategy for surface treatment on hematite photoanode for efficient water oxidation. *Chemical Science* **2013,** *4* (1), 164-169.
43. Yang, X.; Liu, R.; Lei, Y.; Li, P.; Wang, K.; Zheng, Z.; Wang, D., Dual Influence of Reduction Annealing on Diffused Hematite/FTO Junction for Enhanced Photoelectrochemical Water Oxidation. *ACS Applied Materials & Interfaces* **2016,** *8* (25), 16476-16485.

44. Tian, C. M.; Li, W. W.; Lin, Y. M.; Yang, Z. Z.; Wang, L.; Du, Y. G.; Xiao, H. Y.; Qiao, L.; Zhang, J. Y.; Chen, L.; Qi, D.-C.; MacManus-Driscoll, J. L.; Zhang, K. H. L., Electronic Structure, Optical Properties, and Photoelectrochemical Activity of Sn-Doped Fe_2O_3 Thin Films. *The Journal of Physical Chemistry C* **2020,** *124* (23), 12548-12558.

45. Lu, X.-F.; Chen, X.-Y.; Zhou, W.; Tong, Y.-X.; Li, G.-R., α-Fe2O3@PANI Core–Shell Nanowire Arrays as Negative Electrodes for Asymmetric Supercapacitors. *ACS Applied Materials & Interfaces* **2015,** *7* (27), 14843-14850.

46. Cao, C.-Y.; Qu, J.; Yan, W.-S.; Zhu, J.-F.; Wu, Z.-Y.; Song, W.-G., Low-Cost Synthesis of Flowerlike α-Fe_2O_3 Nanostructures for Heavy Metal Ion Removal: Adsorption Property and Mechanism. *Langmuir* **2012,** *28* (9), 4573-4579.

47. Sohlberg, K.; Pantelides, S. T.; Pennycook, S. J., Interactions of Hydrogen with CeO_2. *Journal of the American Chemical Society* **2001,** *123* (27), 6609-6611.

48. Andersson, A. K. E.; Selbach, S. M.; Knee, C. S.; Grande, T., Chemical Expansion Due to Hydration of Proton-Conducting Perovskite Oxide Ceramics. *Journal of the American Ceramic Society* **2014,** *97* (8), 2654-2661.

49. Abel, A. J.; Patel, A. M.; Smolin, S. Y.; Opasanont, B.; Baxter, J. B., Enhanced photoelectrochemical water splitting via SILAR-deposited Ti-doped hematite thin films with an FeOOH overlayer. *Journal of Materials Chemistry A* **2016,** *4* (17), 6495-6504.

50. Bein, B.; Hsing, H.-C.; Callori, S. J.; Sinsheimer, J.; Chinta, P. V.; Headrick, R. L.; Dawber, M., In situ X-ray diffraction and the evolution of polarization during the growth of ferroelectric superlattices. *Nature Communications* **2015,** *6* (1), 10136.

51. Geim, A. K.; Grigorieva, I. V., Van der Waals heterostructures. *Nature* **2013,** *499* (7459), 419-425.

52. Osada, M.; Sasaki, T., Two-Dimensional Dielectric Nanosheets: Novel Nanoelectronics From Nanocrystal Building Blocks. *Advanced Materials* **2012,** *24* (2), 210-228.

53. Wu, Y.; Döhler, D.; Barr, M.; Oks, E.; Wolf, M.; Santinacci, L.; Bachmann, J., Atomic Layer Deposition from Dissolved Precursors. *Nano Letters* **2015,** *15* (10), 6379-6385.

54. Taniguchi, A.; Kubota, Y.; Matsushita, N.; Ishii, K.; Uchikoshi, T., Solution-mediated nanometric growth of α-Fe_2O_3 with electrocatalytic activity for water oxidation. *Nanoscale Advances* **2020,** *2* (9), 3933-3941.

Chapter 3: Nanoscale $Ni(OH)_2$/FeOOH heterostructures fabricated via an alternative deposition process and their catalytic activity

Overview

The use of nanoscale heterostructures is an effective approach for developing catalysts that are free of precious metals for sustainable energy conversion. In this chapter, a sequenced successive ionic layer adsorption and reaction (sequenced-SILAR) method was developed for the fabrication of $Ni(OH)_2$/FeOOH heterostructures. In this method, the order of the deposition cycles of individual $Ni(OH)_2$ and FeOOH layers was programmed to control the thickness and stacking order of these layers in the heterostructure. The sequenced-SILAR process using a Fe^{2+} solution as the iron source produced dense heterojunctions offering overpotentials of 330 and 234 mV at 10 mA cm^{-2} for an oxygen evolution reaction (OER) on flat, conducting oxide substrate and porous Ni foam, respectively. Investigation of the deposition-sequence-dependent OER activity indicated that the $Ni(OH)_2$/FeOOH coupling effects may extend to the Ni^{2+} active sites located about 10 nm from the heterointerface. When a Fe^{3+} precursor was employed in the sequenced-SILAR process, dense heterojunctions were not produced because of the formation of isolated FeOOH particles. As a result, an excellent overpotential was not obtained. In principle, the sequenced-SILAR method can be extended to the fabrication of various types of heterostructures. However, the deposition conditions must be carefully designed to offer strong interfacial coupling effects.

3.1 Introduction

The widespread use of hydrogen (H_2) as a clean fuel is key to maintaining the sustainable development of modern society.[1-2] A practical way to massively produce H_2 fuels is via water electrolysis by using surplus electricity at night.[3] However, the anodic oxygen evolution reaction (OER) requires a huge overpotential to overcome the slow kinetics of OOH bond formation and OH bond breaking.[4-5] Noble metal oxides such as RuO_2 and IrO_2 are known to be highly active OER catalysts.[6-9] However, their high cost makes them unsuitable for large-scale industrial use. Thus, there is an urgent need for the development of precious-metal-free electrocatalysts for OER.

As mentioned in the chapter 1, since 1987, when Corrigan *et al.* reported that iron impurities dramatically enhanced the OER activity of $Ni(OH)_2$ electrodes in alkaline solutions,[10] intensive studies have been carried out on Ni/Fe bimetallic (oxy)hydroxides as promising candidates for practical OER electrocatalysts.[11-13] Along with acquiring a deeper mechanistic understanding, it was found that nanostructured Ni/Fe-based (oxy)hydroxides such as nanoparticles,[14-15] hollow nanoprism,[16] and nanosheets[17] exhibited catalytic activity superior to that of RuO_2- and IrO_2-based catalysts. In these studies, the nanostructures were designed, synthesized, and computed based on the hypothesis that the catalytic activity can be enhanced by the homogeneous doping of Fe ions in the $Ni(OH)_2$ and NiOOH phase matrix.

Apart from the above classic homogeneous doping approach, the heteroassembly of nanounits with different chemical compositions has attracted considerable interest for extending the catalyst design. For example, Li *et al*. have obtained a small overpotential of 330 mV at 10 mA cm^{-2} from a heterolayered nanostructures of Co/TaS_2.[18] Guan *et al.* showed that the NiS-MoS_2 hetero-nanosheet exhibits high catalytic activity with an overpotential of 203 mV at 10 mA cm^{-2}, as well as stability.[19] The synergistic coupling effects for enhancing the catalytic activity for OER have also been found in $NiMoO_x$/NiMoS,[20] NiO/Co_3O_4,[21] Fe-MoS_2/$CoMo_2S_4$,[22] and $NiPS_3$/Ni_2P,[23] ceria/Ni-transition metal oxides,[24] and MnO_2/NiFe LDH[25] systems. As summarized by Long *et al.*,[26] there would be several contributions of heterojunction to the enhanced catalytic activity, including (i) increasing electronic conductivity and active sites, (ii) modulating electronic configuration, (iii) charge redistribution effects, and (iv) reducing the interfacial contact resistance.

Recently, enhanced OER catalytic activity has been found in Ni/Fe (oxy)hydroxide heterostructures. These include β-$Ni(OH)_2$ nanosheets loaded with α-FeOOH nanoparticles.[27] β-FeOOH nanorods coated with $Ni(OH)_2$,[28] γ-FeOOH nanoparticle coated α-$Ni(OH)_2$ layer on Ni.[29] Considering that the catalytic activities are the result of the complex interplay among the crystalline phases of nickel hydroxide and iron oxyhydroxide, shape, and size of the products, the knowledge available through these previous studies has been insufficient yet to offer the origin of the catalytic activity and guideline of material design in this system.

In the present study, a sequenced successive ionic layer adsorption and reaction (sequenced-SILAR) method was developed for fabricating a Ni/Fe (oxy)hydroxide heterostructure. In the conventional SILAR process, the substrate is first immersed in a metal precursor solution.[30] Subsequently, the adsorbed metal ions on the substrate react with the anions from another solution to form an inorganic layer such as hydroxides,[31-32] sulfides,[31, 33] phosphates,[34-35] and fluorides.[36] The thickness obtained by one SILAR cycle is generally a few nanometers. The layer thickness can be controlled by the number of deposition cycles, similar to a layer-by-layer (LbL) assembly using anionic and cationic bipolar amphiphiles.[37] Although the SILAR process has thus far been limited to deposit single component films, the method can, in principle, be extended to produce nanoscale heterostructures. Namely, the composition of the deposited layer can be arbitrarily selected from cycle to cycle by arbitrarily making a selection from multiple metal and anion precursor solutions for each deposition step.

A sequenced-SILAR approach was applied for the nanoscale design of Ni/Fe (oxy)hydroxide heterostructures. In this study, first, the formation of the heterostructures by comprehensive microscopic and spectroscopic techniques was investigated. Linear sweep voltammetry (LSV) and chronoamperometry were employed to reveal the effects of the heterojunction on the catalytic activity and durability for OER, respectively. Finally, effects of the deposition sequences and iron precursor on the catalytic activity were investigated to produce an optimized Ni/Fe (oxy)hydroxide heterostructure. These results revealed that the sequenced-SILAR method using an Fe^{2+} solution as the Fe source produced dense $Ni(OH)_2$/FeOOH heterojunctions offering catalytic activity comparable or superior to those of state-of-the-art Ni/Fe binary (oxy)hydroxide catalysts. However, the use of an Fe^{3+} solution led to sparser heterointerfaces due to the formation of isolated FeOOH particles, which resulted in the weakened enhancement of catalytic activity. The dependence of the OER activity on the deposition sequence indicated that the interaction through the

heterojunction was not localized only at the interface but instead had a long-range influence on the electrochemical activity at the Ni^{2+} sites.

3.2 Experimental

3.2.1 Preparation of the precursor solutions.

The metal source precursors used in this study were $FeCl_2 \cdot 4H_2O$ (99.0-102.0 %), $FeCl_3 \cdot 6H_2O$ (99.0 %), and $Ni(NO_3)_2 \cdot 6H_2O$ (98.0 %) (all from FUJIFILM Wako Pure Chemical Corp.). The cation solution was prepared by dissolving 0.1 M of $FeCl_2 \cdot 4H_2O$, $FeCl_3 \cdot 6H_2O$, or $Ni(NO_3)_2 \cdot 6H_2O$ in 50 mL of distilled water. Nitrogen gas was purged into the solution for 5 min to prevent oxidation of the reactants in the solution.

3.2.2 Deposition process in a successive ionic layer adsorption and reaction (SILAR).

Substrates including fluorine-doped tin oxide coated glass substrate (FTO, 10 mm × 50 mm × 1.1 mm, FTN 1.1, 10 Ω/sq, AGC Inc.), quartz glass (10 mm × 50 mm × 1 mm, GL Sciences Inc.), and Ni foam (99.99 % purity, 1.6 mm thickness, 80–110 PPI pore size, MTI Co., Ltd.) were selected. The substrates were treated with UV/O_3 (ASM401N, Asumi Giken, Ltd.) for 15 min to obtain a hydrophilic surface. For the SILAR process, first, the substrates were immersed for 10 s in the source solution heated to 75 ℃, followed by rinsing with distilled water. Next, the substrate was immersed for 10 s in a 1 M KOH aqueous solution (FUJIFILM Wako Pure Chemical Corp.). heated to 75 ℃ and then rinsed with distilled water again. A series of these operations was repeated to obtain Ni or Fe hydroxide layers as well as Ni/Fe heterostructures under the programmed deposition sequences (Figure 3.1).

3.2.3 Characterization.

The crystalline phases of the deposited films were investigated by X-ray diffraction (XRD; X'Pert-Pro-MRD, CuKα, 45 kV and 40 mA, PANalytical). The surface morphologies and textures of the films were observed by scanning electron microscopy (SEM; SU-8020, Hitachi High-Technologies) and atomic force microscopy (AFM; S-image, Hitachi High-Tech Science Corporation). The cross-sectional morphologies of the films were observed by transmission electron microscopy (TEM; JEM-2010F, JEOL) at an acceleration voltage of 200 kV, and their elemental distribution was analyzed by EDS (GENESIS, Edax). Focused ion beam (FIB) etching was used to prepare a specimen for cross-sectional TEM analysis of a SILAR-derived layer on a FTO substrate. The light absorbance of the samples in the ultraviolet-visible (UV-Vis) region was evaluated by UV/Vis spectroscopy (V-770, JASCO). The absorption spectra of the deposited layer on a quartz substrate were measured using a quartz substrate as a reference. X-ray photoelectron spectroscopy (XPS; JPS 9010 TR, JEOL) was conducted to investigate the chemical state of the samples. All measured XPS spectra were calibrated corresponding to the value of the C 1s peak at 284.4 eV using a Mg Kα X-ray source at 1253.6 eV. Raman spectroscopy measurements were conducted using a Horiba XploRA PLUS equipped with a 532 nm laser and a microscope for focusing the laser light on the film surface.

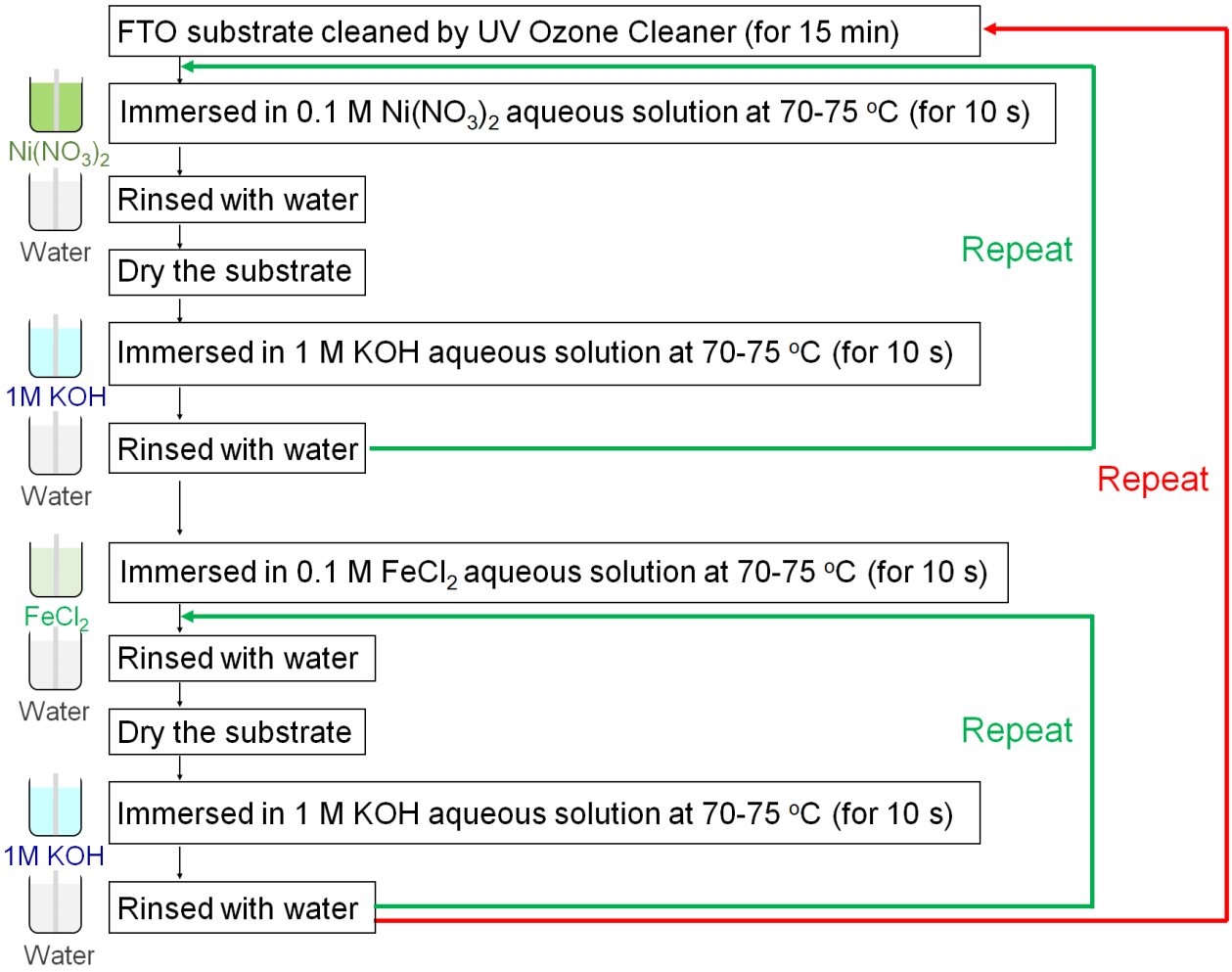

Figure 3.1. Flowchart of sequenced-SILAR procedure.

3.2.4 Electrochemical Measurement.

The OER measurements were performed in a 1 M KOH aqueous solution using a three-electrode configuration, with a Pt wire counter electrode and an Ag/AgCl, KCl reference electrode. All potentials were referenced to the reversible hydrogen electrode (RHE) by the following equation: $V_{RHE} = V_{Ag/AgCl} + 0.197\ V + 0.059\ V \times pH$. Cyclic voltammetry (CV) and linear sweep voltammetry (LSV) were performed at a scan rate of 20 mV s^{-1} (Figure 3.2).

3.3 Results and discussion

3.3.1 Design of Sequenced-SILAR deposition.

Figure 3.3 illustrates the sequenced-SILAR process proposed in the present study. In this process, the substrate is immersed in a Ni or Fe precursor solution to form the metallic cation adlayer on the substrate followed by the reaction with a KOH solution to convert it to a hydroxide (or oxyhydroxide) layer. Ni^{2+} solution

was used as the Ni precursor. However, Fe^{2+} and Fe^{3+} precursor solutions could be candidate as Fe sources. Previously, a liquid-phase deposition methods was developed liquid-phase to fabricate α-Fe_2O_3 thin films.[38-39] In those studies, Fe^{2+} ions were homogeneously adsorbed on the substrate to induce uniform film growth. Therefore, the sequenced-SILAR deposition with an Fe^{2+} precursor was first examined for fabricating the target heterostructures. As a preliminary experiment for fabricating a Ni/Fe-based heterostructure by the sequenced-SILAR method, the crystal structure of the precipitates formed by directly mixing the KOH solution with the Ni^{2+} or Fe^{2+} solution was analyzed by XRD. As shown in Figure 3.4, reflection peaks from the β-$Ni(OH)_2$ (JCPDS No. 14-0117)[40] and α-FeOOH (JCPDS No. 29-0713)[41] phases were detected when the Ni^{2+} and Fe^{2+} solutions were employed, respectively. Accordingly, it was assumed that the SILAR process using the Ni^{2+} and Fe^{2+} solutions would yield relevant products with these compounds.

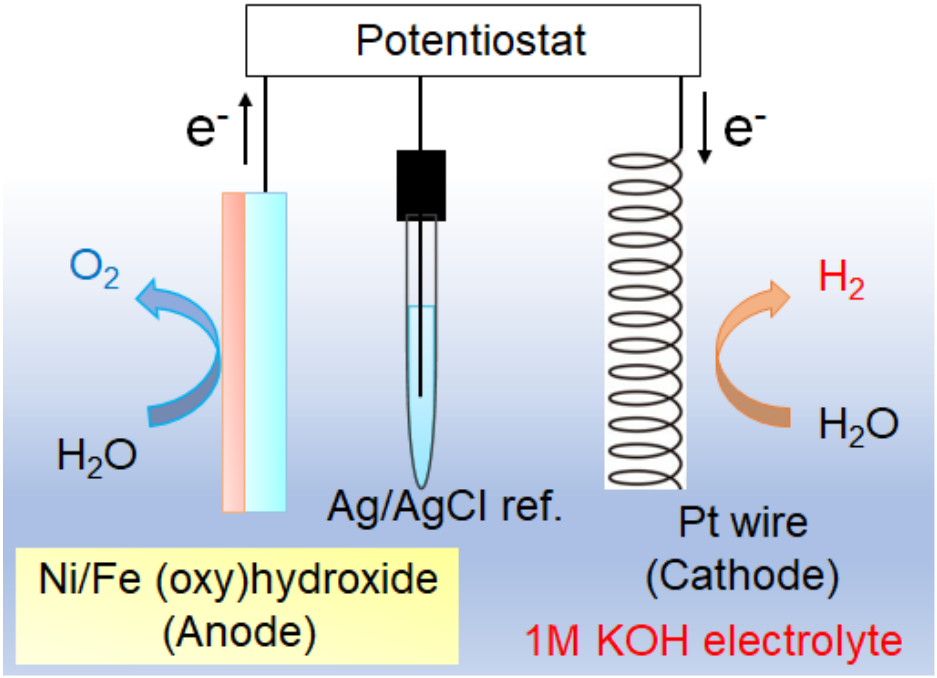

Figure 3.2. OER measurement conditions.

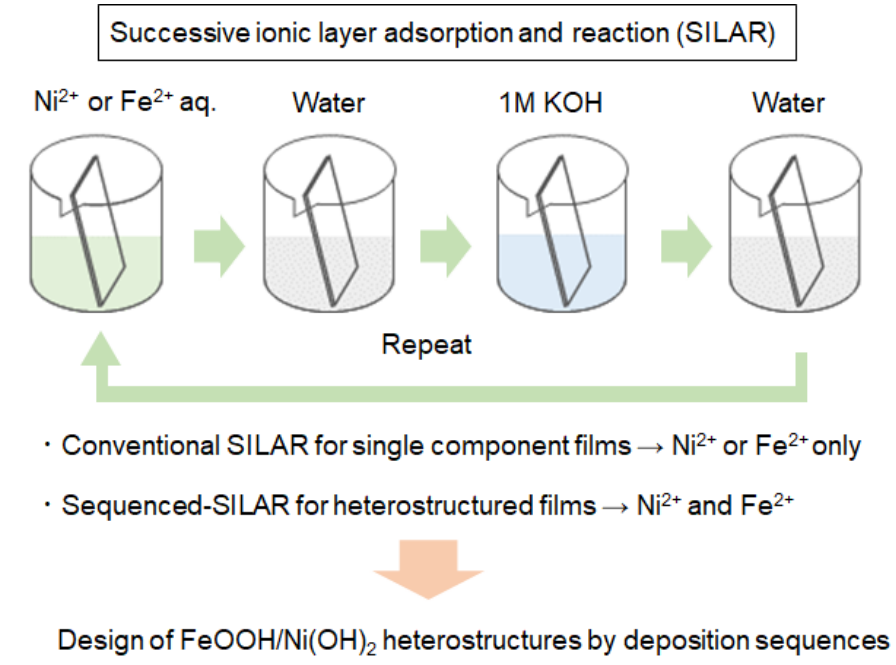

Figure 3.3. Sequenced-SILAR process.

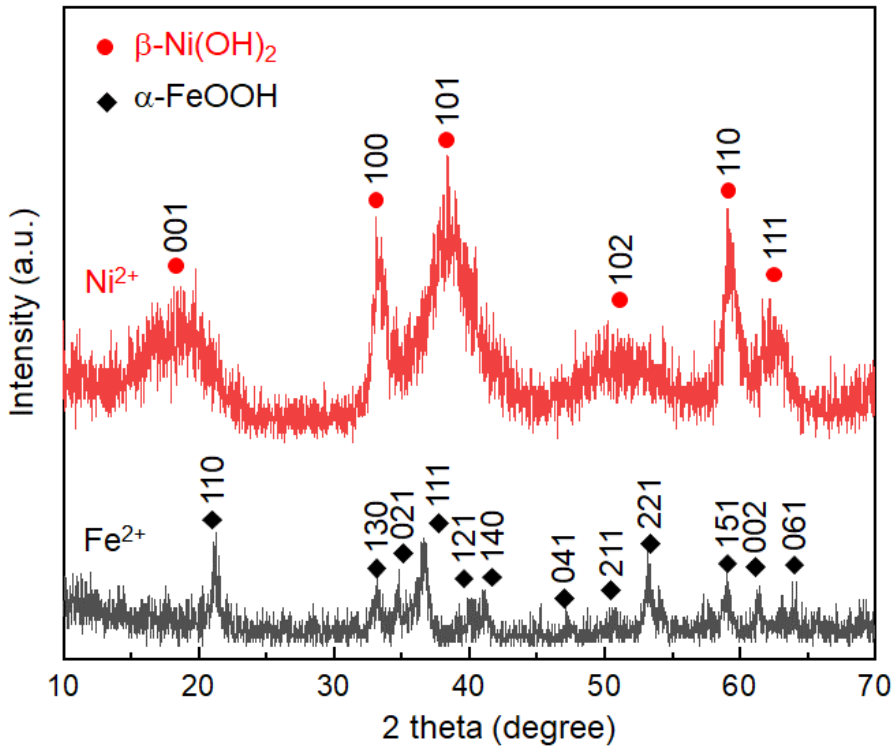

Figure 3.4. XRD patterns of the precipitates formed by directly mixing the KOH solution with the Ni^{2+} or Fe^{2+} solution.

3.3.2 Characterization of Sequenced-SILAR deposition.

First, the SILAR deposition using either the Ni^{2+} or Fe^{2+} solution was investigated. The samples with a single component layer were labeled **Ni*n*** and **Fe*n***, where *n* corresponds to the number of deposition cycles (Figure 3.5). As shown in Figure 3.6, **Ni25** and **Fe25** present an optical absorption edge around 300 and 700 nm, respectively. Subsequently, the sequenced-SILAR process using Ni^{2+} and Fe^{2+} dual precursors was conducted. In the sequence design, $Ni(OH)_2$ and FeOOH layers were alternately formed, where each layer was fabricated by the same deposition cycle number (*n*), yielding a **(Fe*n*/Ni*n*)** unit. Then, the deposition of the **(Fe*n*/Ni*n*)** unit was repeated *m* times to produce $\mathbf{(Fen/Nin)_m}$. The **Ni*n*** layer was always deposited at the last step. Therefore, the samples were labeled $\mathbf{Nin(Fen/Nin)_m}$. $\mathbf{Ni5(Fe5/Ni5)_2}$ was deposited on the quartz glass substrate. The resultant film exhibits the absorption features of both **Ni25** and **Fe25** (Figure 3.6). When the spectra of **Ni25** and **Fe25** were multiplied by 3/5 and 2/5, respectively, to match the total number of Ni and Fe deposition cycles for the fabrication of $\mathbf{Ni5(Fe5/Ni5)_2}$, and then those values were added, the resultant spectra were in good agreement with those of $\mathbf{Ni5(Fe5/Ni5)_2}$. This indicates that the thickness increment per deposition cycle was not significantly altered by the sequenced-SILAR process. Hence, this approach would allow us to control the thickness and order of individual $Ni(OH)_2$ and FeOOH layers in the deposited film.

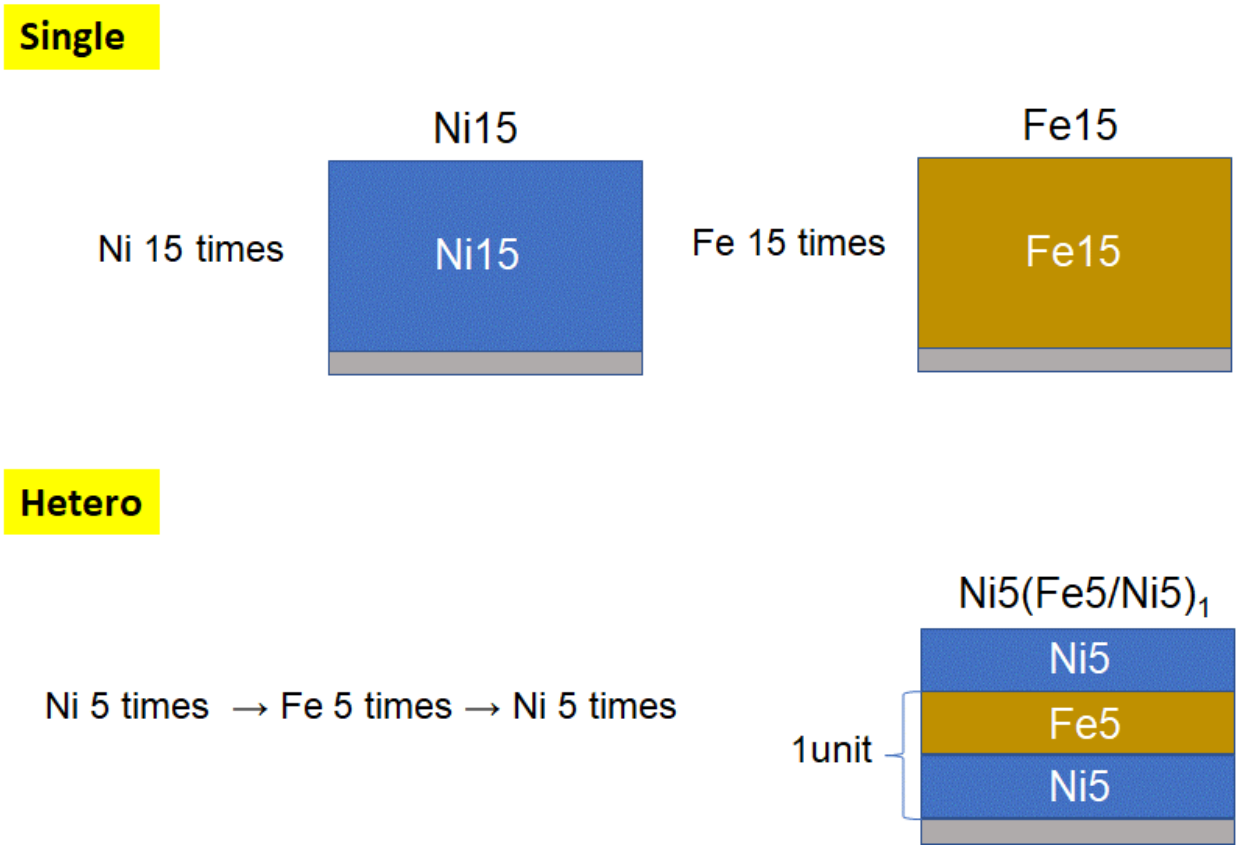

Figure 3.5. The deposition sequence and sample-naming.

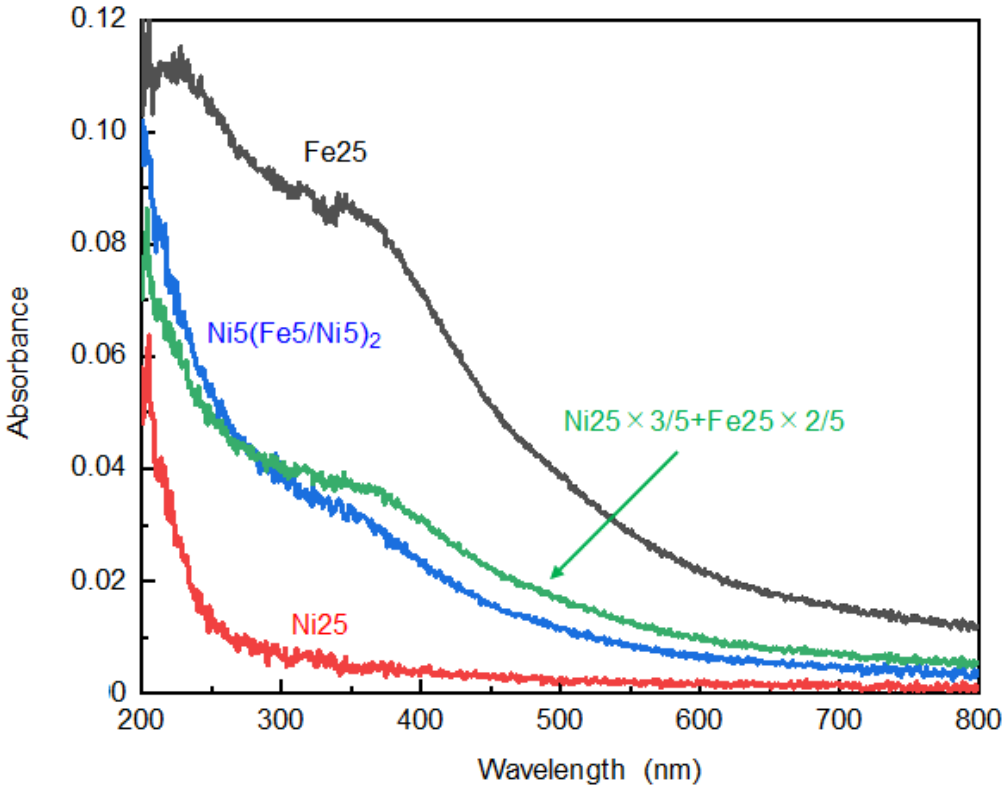

Figure 3.6. UV-vis absorption spectra of **Ni25**, **Fe25**, and **Ni5(Fe5/Ni5)$_2$** and the spectrum produced using the formula Ni25×3/5 + Fe25×2/5.

Next, the SILAR deposition was performed on the FTO substrate as a conducting substrate. These samples were optically transparent due to the ultrathin thickness and/or high uniformity (Figure 3.7).

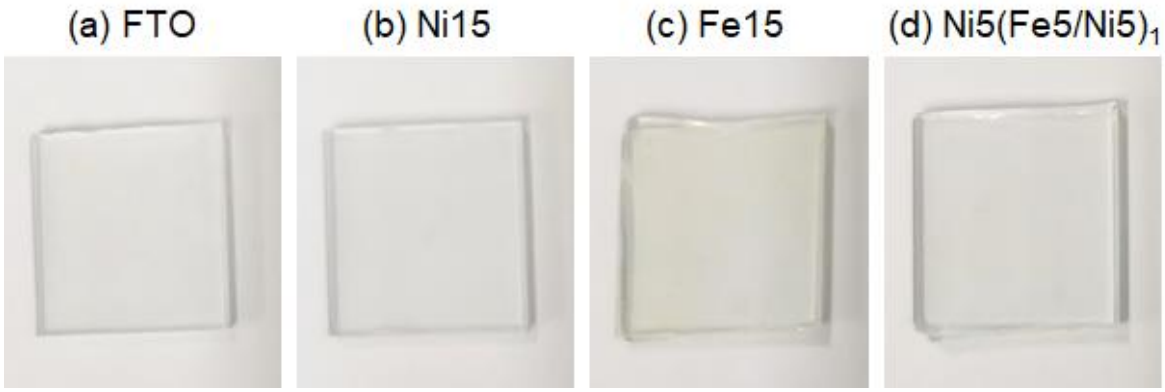

Figure 3.7. Digital photoimages of FTO and SILAR-derived samples on FTO.

SEM observations revealed that the surface morphology of **Ni15** and **Ni5(Fe5/Ni5)$_1$** was similar to that of the uncoated FTO substrate (Figure 3.8), while a thin layer was likely formed on the entire substrate. The result indicates that the deposited layer via the SILAR followed the uneven FTO surface, according to the LbL deposition principle.

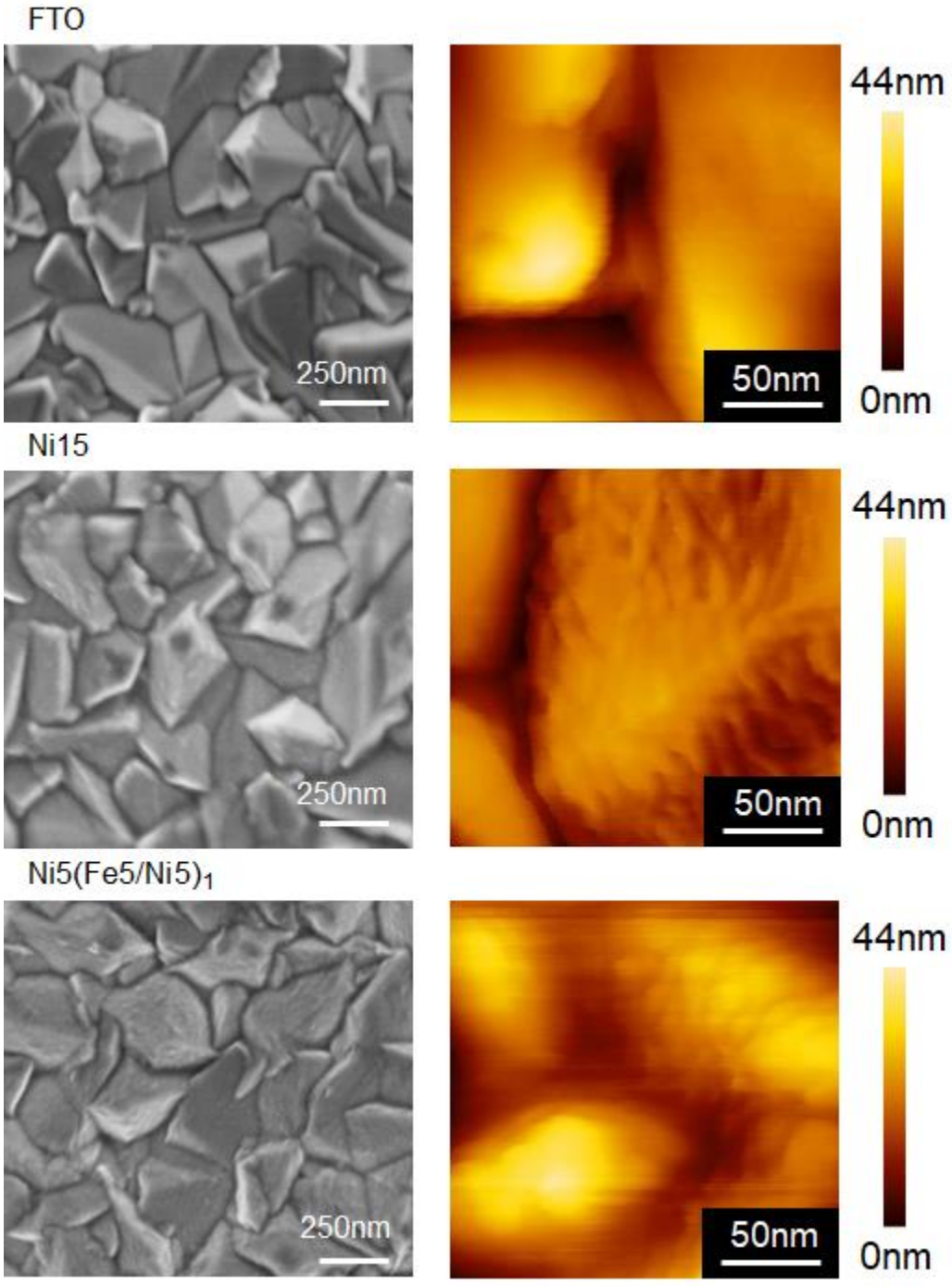

Figure 3.8. SEM and AFM images of the FTO substrate and **Ni15** and **Ni5(Fe5/Ni5)$_1$** deposited on the FTO substrate.

The height profile extracted from the AFM images provided the evidence that the deposited layers exhibited nanoscale roughness approximately up to 5 nm (Figure 3.9).

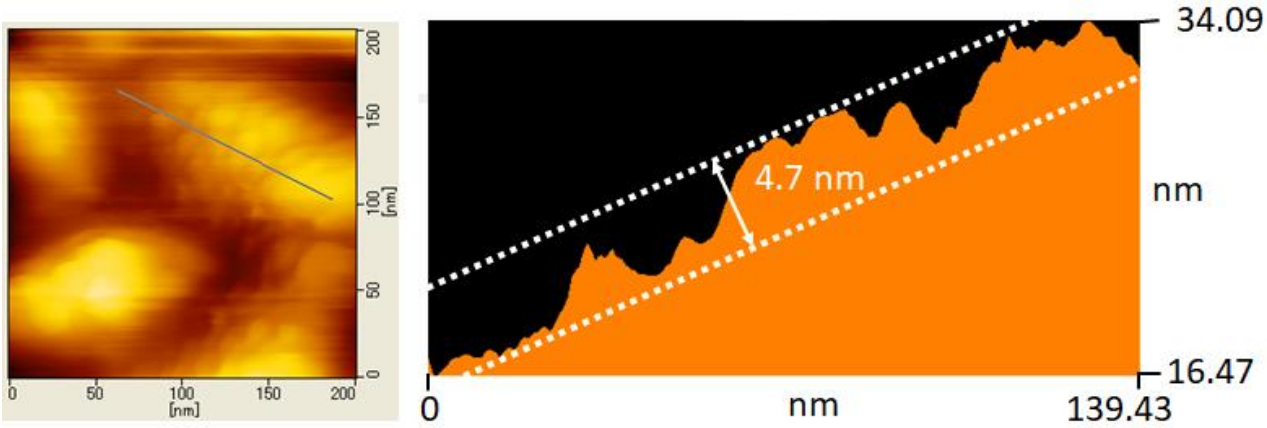

Figure 3.9. The cross-section height profile of the AFM image of **Ni5(Fe5/Ni5)$_1$**.

Figure 3.10 shows the Ni 2p XPS spectra for **Ni15** and **Ni5(Fe5/Ni5)$_1$**. In the Ni 2p spectra, Ni $2p_{1/2}$ and Ni $2p_{3/2}$ are detected for both samples. The peak positions of the Ni $2p_{1/2}$ and Ni $2p_{3/2}$ bands appear at 872 and 855 eV, respectively, which is consistent with the divalent nickel pattern and indicates that Ni is present as $Ni(OH)_2$.[42-43] The peak position of Fe $2p_{3/2}$ for **Ni5(Fe5/Ni5)$_1$** (710 eV) is attributable to the intermediate position of the Fe^{2+} and Fe^{3+} states.[44-45] Thus, Fe^{2+} remains in the as-deposited film, while partial oxidation to Fe^{3+} occurred during the deposition and/or after exposure to air. Thus, the actual chemical composition of the product deviates from FeOOH. Nevertheless, $Fe(OH)_2$ and $Fe(OH)_3$ are known to be unstable products in the reaction of iron species with a base so that they favor to undergo a transformation to the more stable FeOOH phase under given reaction conditions. Hence, the denotation of the product as FeOOH is kept throughout the present work. The calculated Ni:Fe atomic ratio for **Ni5(Fe5/Ni5)$_1$** was 3:1. The much higher Ni content compared to the Fe content indicates that a $Ni(OH)_2$-rich layer was deposited on the outermost surface region, as was designed.

An XPS depth-profile analysis was employed to prove the formation of heterointerfaces in **Ni5(Fe5/Ni5)$_1$** (Figure 3.11). Figure 3.12 summarizes the intensity ratio of the Ni $2p_{3/2}$/Fe $2p_{3/2}$/Sn $3p_{3/2}$ peak positions versus the analytical depth. First, the Ni $2p_{3/2}$ intensity ratio gradually decreased with an increase in the analytical depth, whereas the Fe $2p_{3/2}$ and Sn $3p_{3/2}$ peak intensity ratios increased. This trend confirms that the $Ni(OH)_2$ layer was formed on the FeOOH underlayer to give a $Ni(OH)_2$/FeOOH heterostructure. Second, the Fe $2p_{3/2}$ peak intensity ratio was maximized at a depth of around 20 nm. Thus, an FeOOH-dominant layer existed around this thickness region. The bottom $Ni(OH)_2$ layer would be formed between the FeOOH middle layer and the substrate surface. Third, the Sn $3p_{3/2}$ peak continuously increased up to an analytical depth of 50 nm. Thus, the total thickness was estimated to be ~50 nm. The thickness was approximately one order of magnitude larger than the surface roughness observed by AFM analysis (~5 nm), suggesting that the deposited layer could be rather homogeneous in thickness. It is noted that the surface of the FTO layer was not flat and

the heterostructures obtained by the sequenced SILAR would not be homogeneous, unlike ideal superlattice structures obtained by pulse laser deposition. Thus, the available information from the depth profile is only limited to probe the overall elemental distribution of the hetero-structures fabricated.

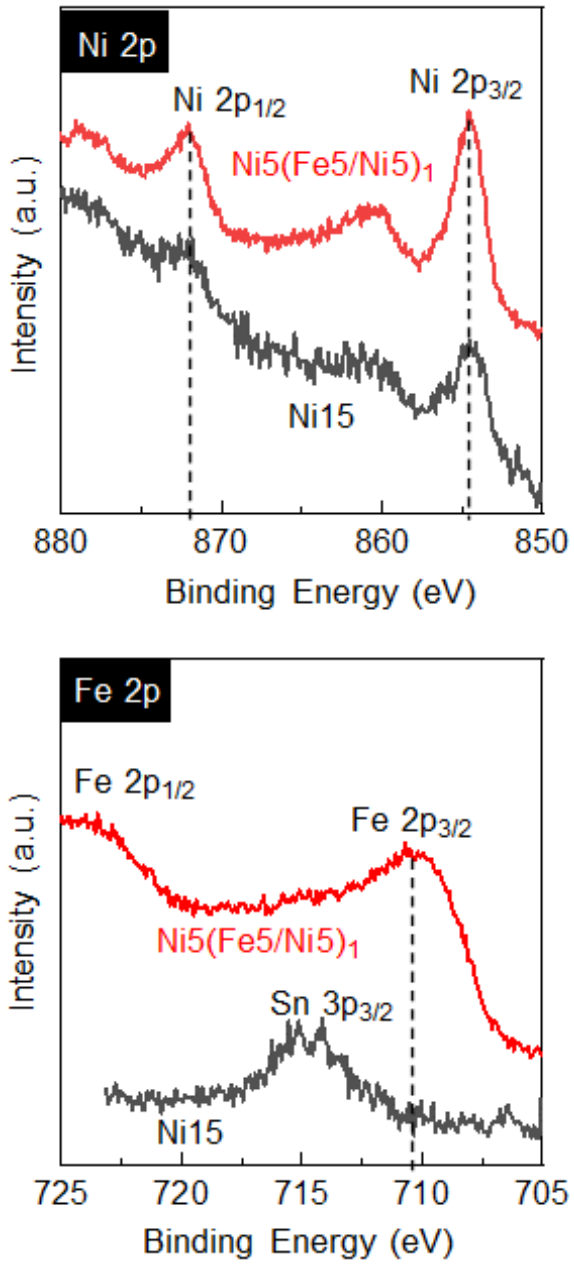

Figure 3.10. Ni 2p and Fe 2p XPS spectra of **Ni15** and **Ni5(Fe5/Ni5)$_1$** on the FTO substrate.

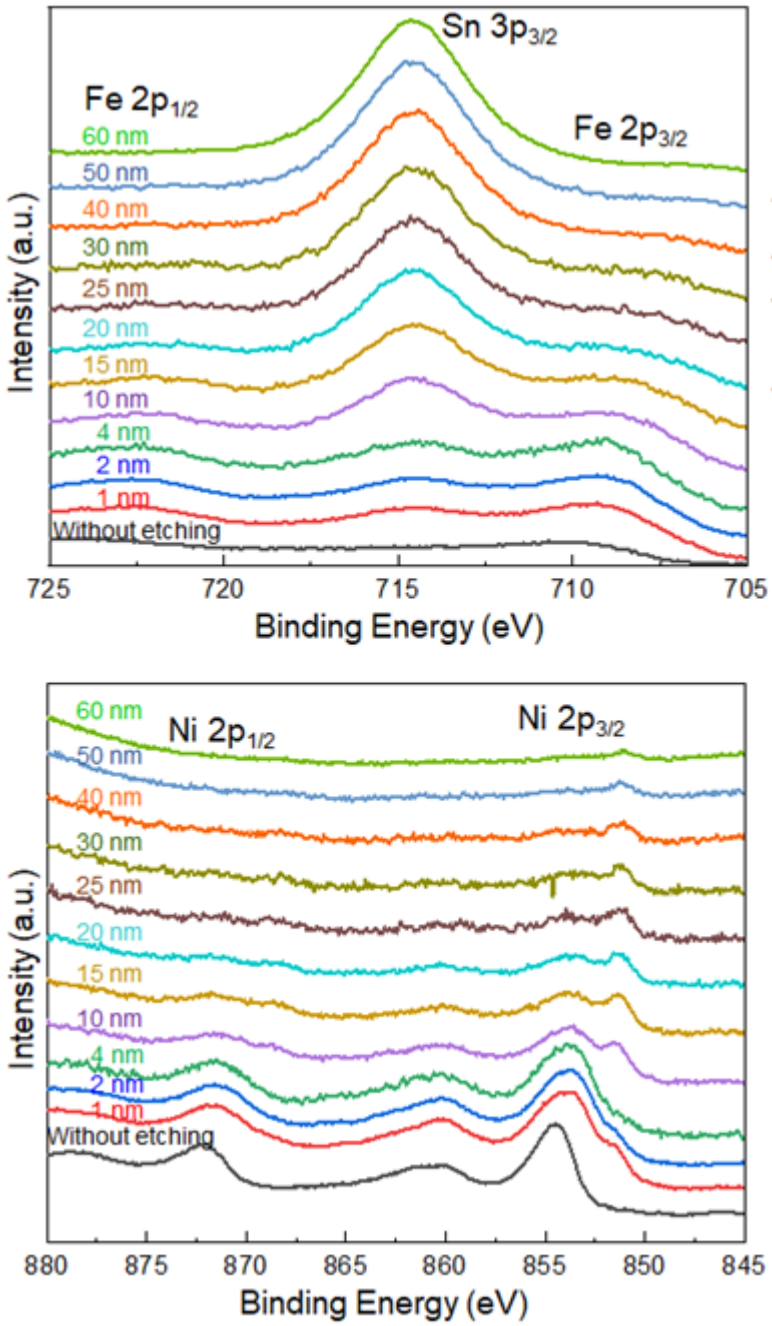

Figure 3.11. Fe 2p and Ni 2p spectra of Ar-etched **Ni5(Fe5/Ni5)$_1$** deposited on FTO.: Fe 2p and Ni 2p peaks shifted to low-energy side due to the reduction by Ar^+ sputtering.

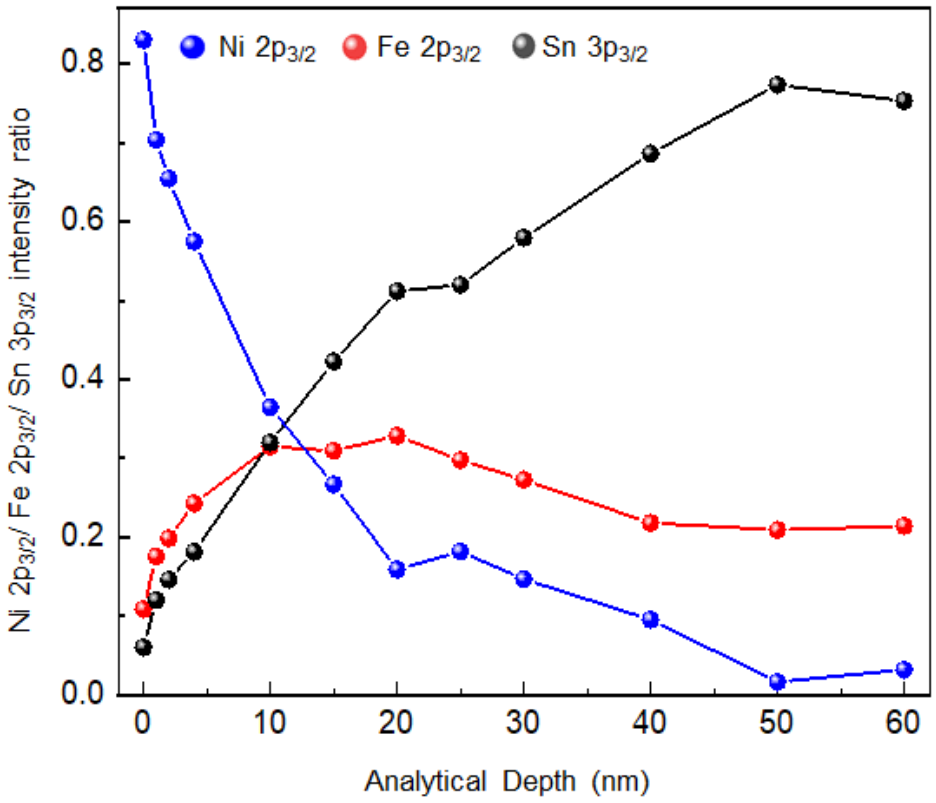

Figure 3.12. XPS depth profile of **Ni5(Fe5/Ni5)$_1$** deposited on the FTO substrate.

The microstructures of the SILAR-derived $Ni(OH)_2$/FeOOH heterostructures were investigated by XRD and transmission electron microscopy (TEM). For this investigation, the total number of deposition cycles was increased to 75 times to enhance the output signals, while the order and number of depositions for each $Ni(OH)_2$ and FeOOH layer remained the same (5 cycles). Accordingly, the sample was labeled **Ni5(Fe5/Ni5)$_7$**. The XRD pattern showed a broad peak attributable to the 006 reflection from the α-$Ni(OH)_2$ phase with a background peak from the FTO substrate (Figure 3.13).[46-47] No diffraction peaks were detectable from the Fe-based compounds, indicating that the $Ni(OH)_2$ and FeOOH layers should be amorphous-like or composed of tiny crystallites.

TEM observation was performed to resolve the heterostructures in **Ni5(Fe5/Ni5)$_7$**. Figure 3.14 (a) displays a cross-sectional scanning TEM (STEM) image of the **Ni5(Fe5/Ni5)$_7$** film formed on a FTO substrate. The observed thickness was ca. 100 nm -150 nm. The total number of deposition cycles is 75 so that a growth rate of ca. 2 nm per a deposition cycle is estimated. The corresponding elemental mapping image of Ni and Fe (Figure 3.14 (b)) clearly probe the inhomogeneous distribution of these elements. In particular, the top and bottom layers predominantly composed of Ni-based layers with the thicknesses up to ca. 10 nm. An Ni/Fe elemental mapping focused on a FTO interface region further revealed that a Ni-based layer was dominantly formed at the bottom (Figure 3.15). Subsequently, a Fe-based layer was formed on the Ni-based bottom layer. Each Fe and Ni-based domains was in ca. 10 nm scale. Lattice fringes were slightly observed in a bright-field

high resolution TEM (HRTEM) image (Figure 3.16). The Fast Fourier Transform (FFT) analysis of the HRTEM image detected the presence of lattice fringes with the distances of 0.38 nm and 0.48 nm attributable to (006) and (001) planes of α-$Ni(OH)_2$ and β-$Ni(OH)_2$ phases, respectively,[48-49] whereas the presence of any FeOOH phases was not indicated. Considering that the homogeneous precipitation of Fe^{2+} with KOH at 75 °C yielded crystalline α-FeOOH (Figure 3.4), the nanometric growth mechanism of the SILAR deposition would inhibit the crystallization. On the basis of the combined XRD and TEM analyses, it is concluded that the nanoscale heterostructures based on the crystalline $Ni(OH)_2$ phases and amorphous FeOOH were produced via the sequenced SILAR.

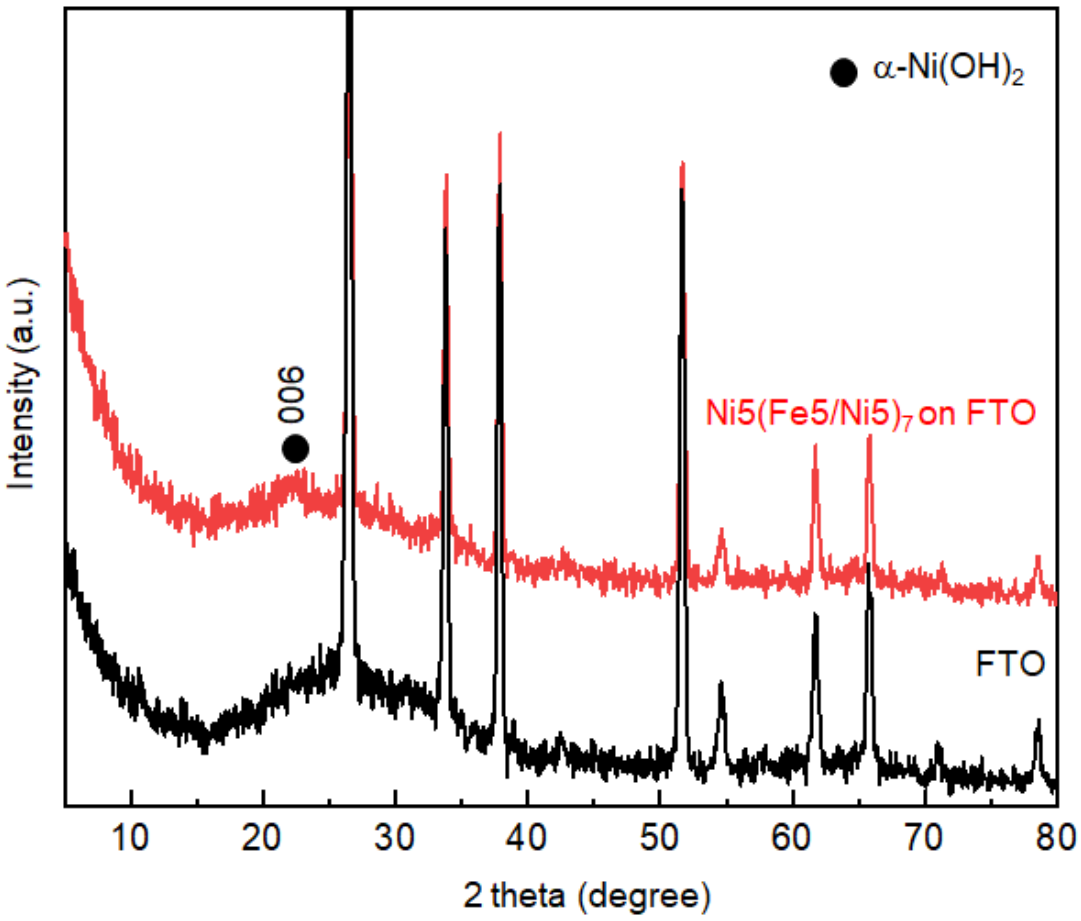

Figure 3.13. XRD patterns of a FTO substrate and **Ni5(Fe5/Ni5)$_7$** deposited on FTO substrate.

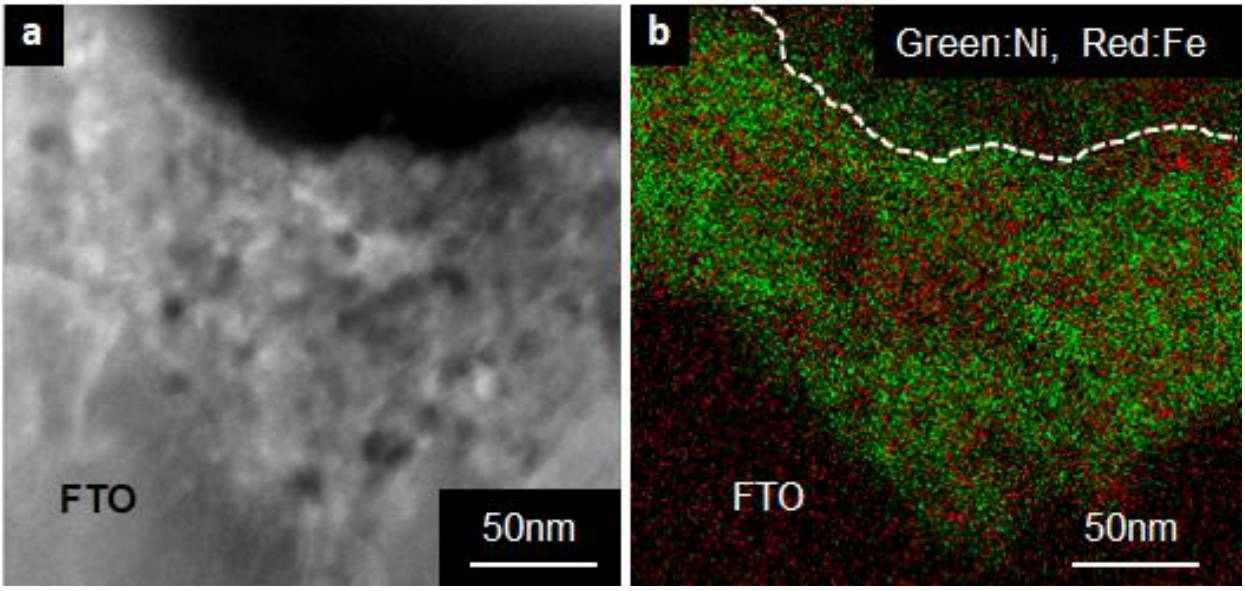

Figure 3.14. (a) Low-magnification cross-sectional STEM image of **Ni5(Fe5/Ni5)$_7$**, (b) Ni/Fe overlay image obtained by STEM-EDS mapping corresponding to Figure 3.14. (a).

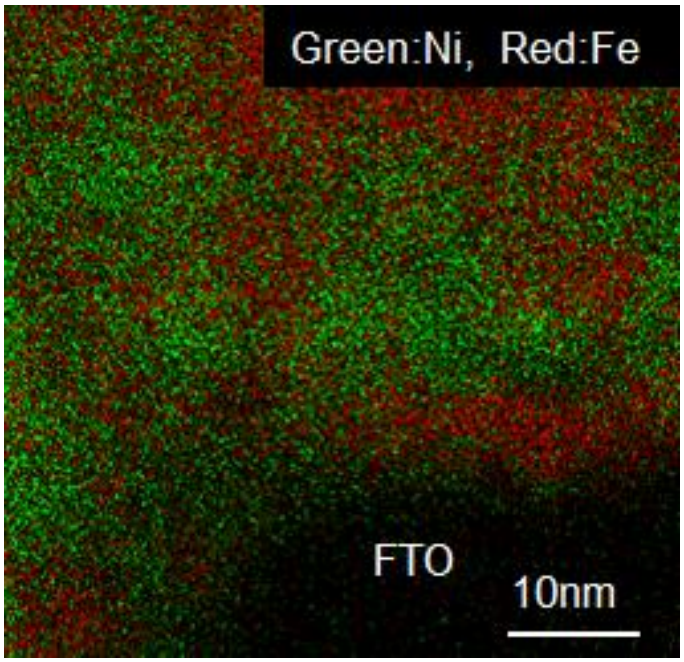

Figure 3.15. Ni/Fe elemental mapping focused on a FTO interface region.

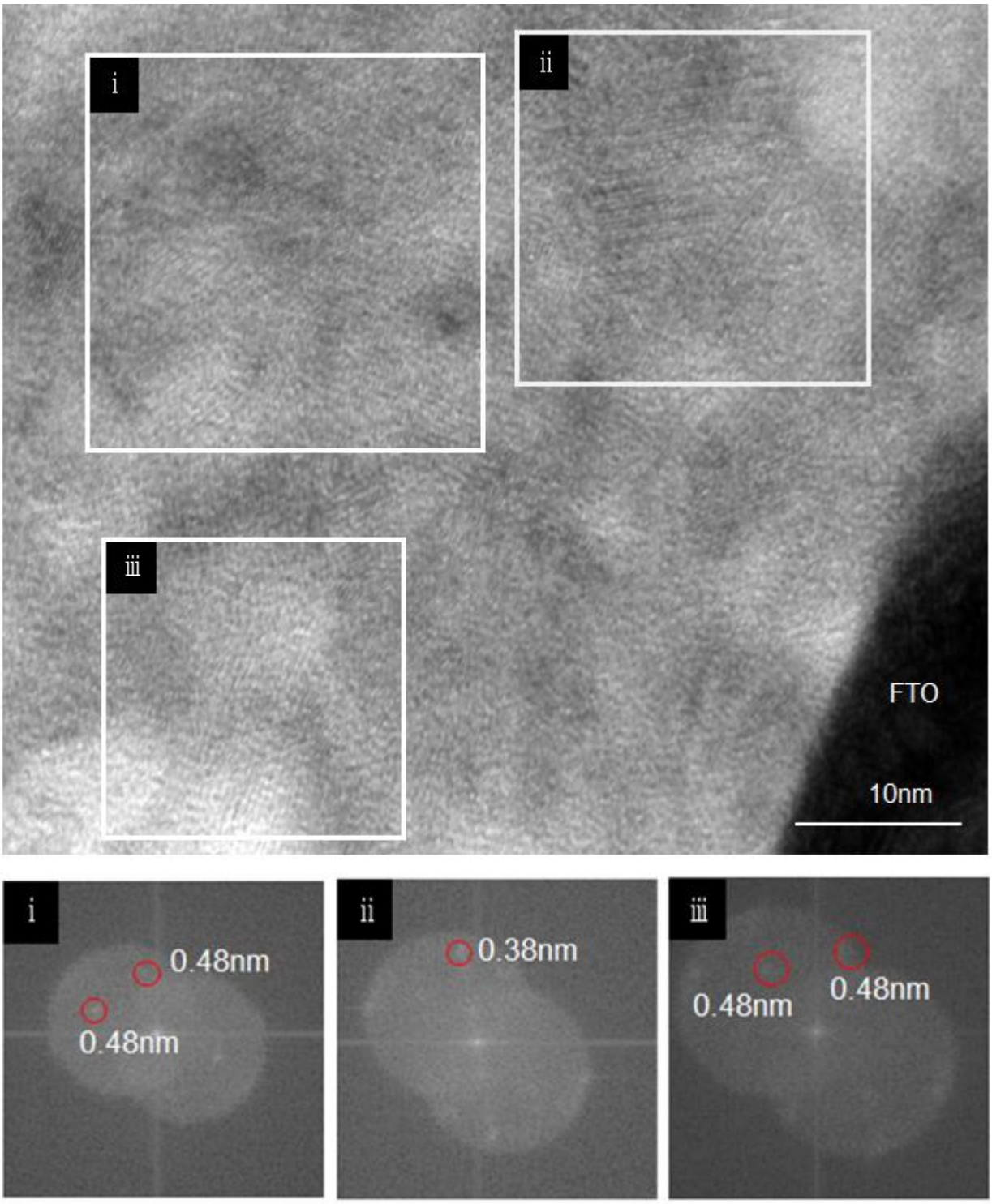

Figure 3.16. HRTEM image and FFT images obtained from the region (i), (ii), and (iii).

3.3.3 OER performance of Sequenced-SILAR-derived Electrodes.

The **Ni15**, **Fe15**, and **Ni5(Fe5/Ni5)$_1$** on FTO were used as the working electrodes to catalyze the OER in a three-electrode setup in an alkaline medium (1.0 M KOH). The polarization curves in Figure 3.17 show that the overpotential of the **Ni5(Fe5/Ni5)$_1$** electrode is 330 mV at a current density of 10 mA cm^{-2}, which is much lower than that of **Ni15** (570 mV at 10 mA cm^{-2}) and **Fe15** (610 mV at 10 mA cm^{-2}). After continuous operation for 12 h at an overpotential of 460 mV, the **Ni5(Fe5/Ni5)$_1$** electrode retained 83 % of its original current density (Figure 3.18), while only 24 % was retained for the **Ni15** electrode. Thus, the Ni(OH)$_2$/FeOOH heterostructure improved both the catalytic activity and the durability.

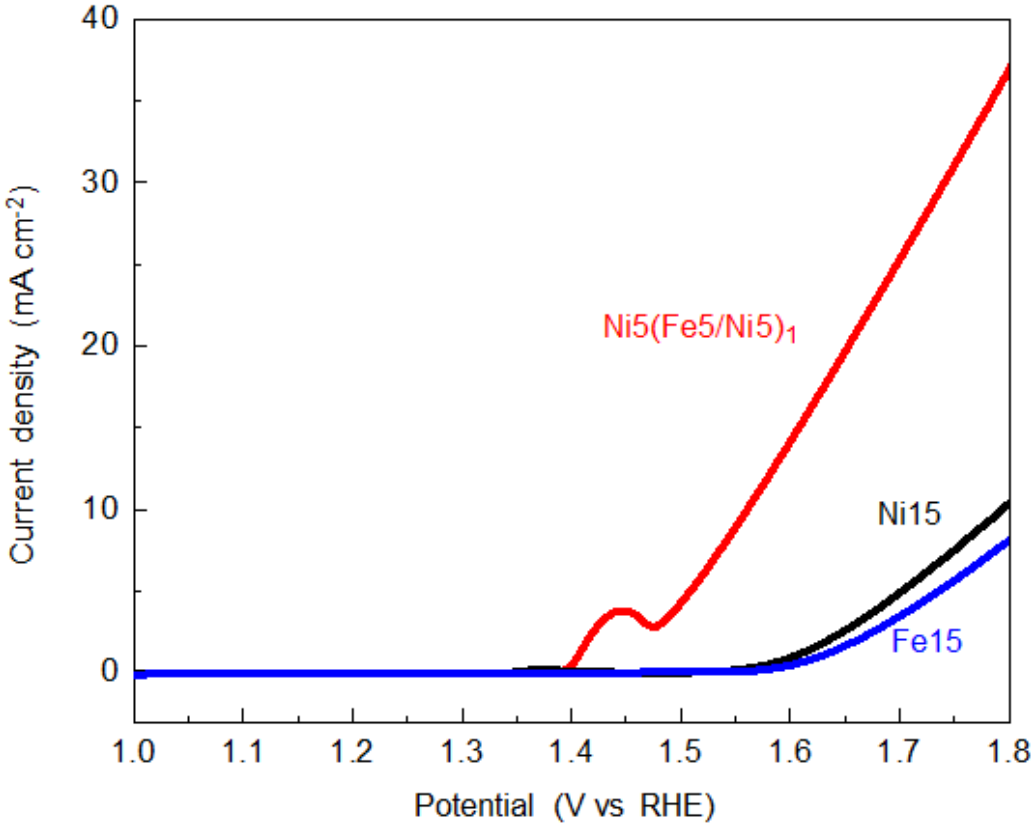

Figure 3.17. LSV curves for **Fe15**, **Ni15**, and **Ni5(Fe5/Ni5)$_1$** deposited on FTO.

Subsequently, the Ni(OH)$_2$/FeOOH heterostructure after 20 cycles CV scans was investigated to discuss the structural stability, since the alternation in the chemical composition and shape of catalysts under the operation of catalytic reactions could be a possible origin of the enhanced activity.[50-51] First, it was confirmed that initial activity was almost unchanged after the CV scans (Figure 3.19). According to the XPS analysis, the sample after the CV scans maintained the initial Ni:Fe ratio (3:1) (Figure 3.20), which indicates the unchanged elemental distribution. It was found that the position of the Fe 2p$_{3/2}$ peak shifted to higher energy side after the CV measurements. Thus, the Fe^{2+} species remained in the as-deposited film were irreversibly

oxidized to the stable trivalent state by the first electrochemical oxidation. XRD analysis of the sample after the CV scans showed that the (006) peak from α-$Ni(OH)_2$ slightly developed, while any peaks from the crystalline FeOOH phases were not detected (Figure 3.21). Thus, remarkable coarsening of α-$Ni(OH)_2$ grains as well as crystallization of FeOOH unlikely occurred during the CV cycles. Thus, the structurally stability of the $Ni(OH)_2$/FeOOH obtained by the sequenced SILAR was supported by all the data. It is noted that the high stability of a $Ni(OH)_2$/FeOOH heterostructure during OER operation was also reported by Niu *et al.*[27] Thus, $Ni(OH)_2$/FeOOH systems could be suitable to offer durable OER catalysts.

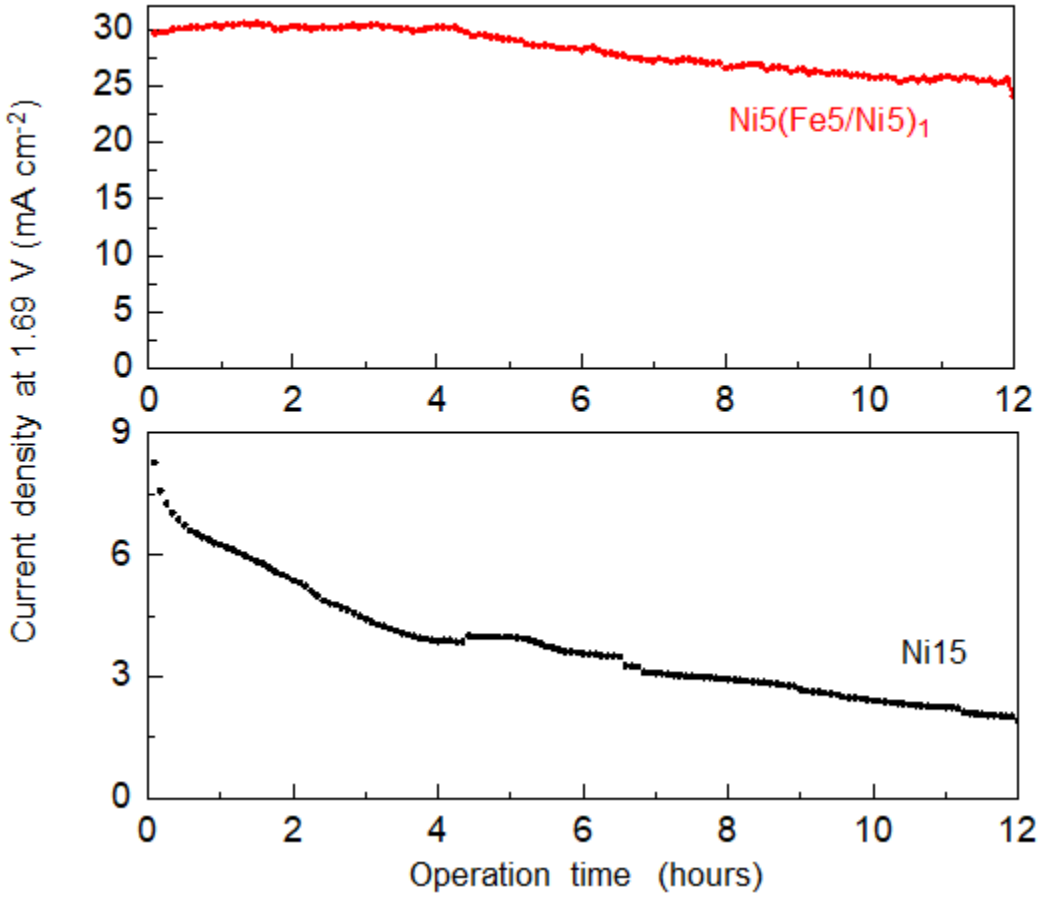

Figure 3.18. Amperometry data recorded for **Ni15** and **Ni5(Fe5/Ni5)$_1$** deposited on FTO substrate at a fixed potential of 1.69 V vs. RHE.

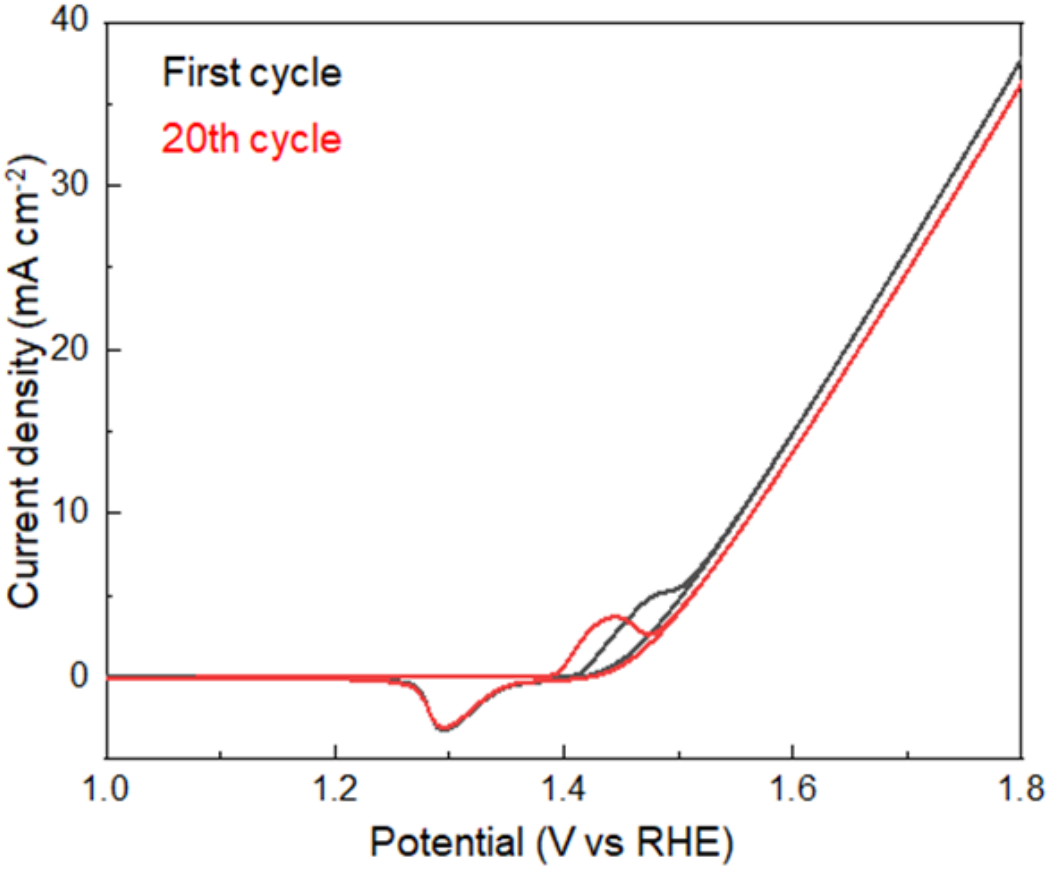

Figure 3.19. CV curves of **Ni5(Fe5/Ni5)$_1$** before/after 20 cycles CV measurements.

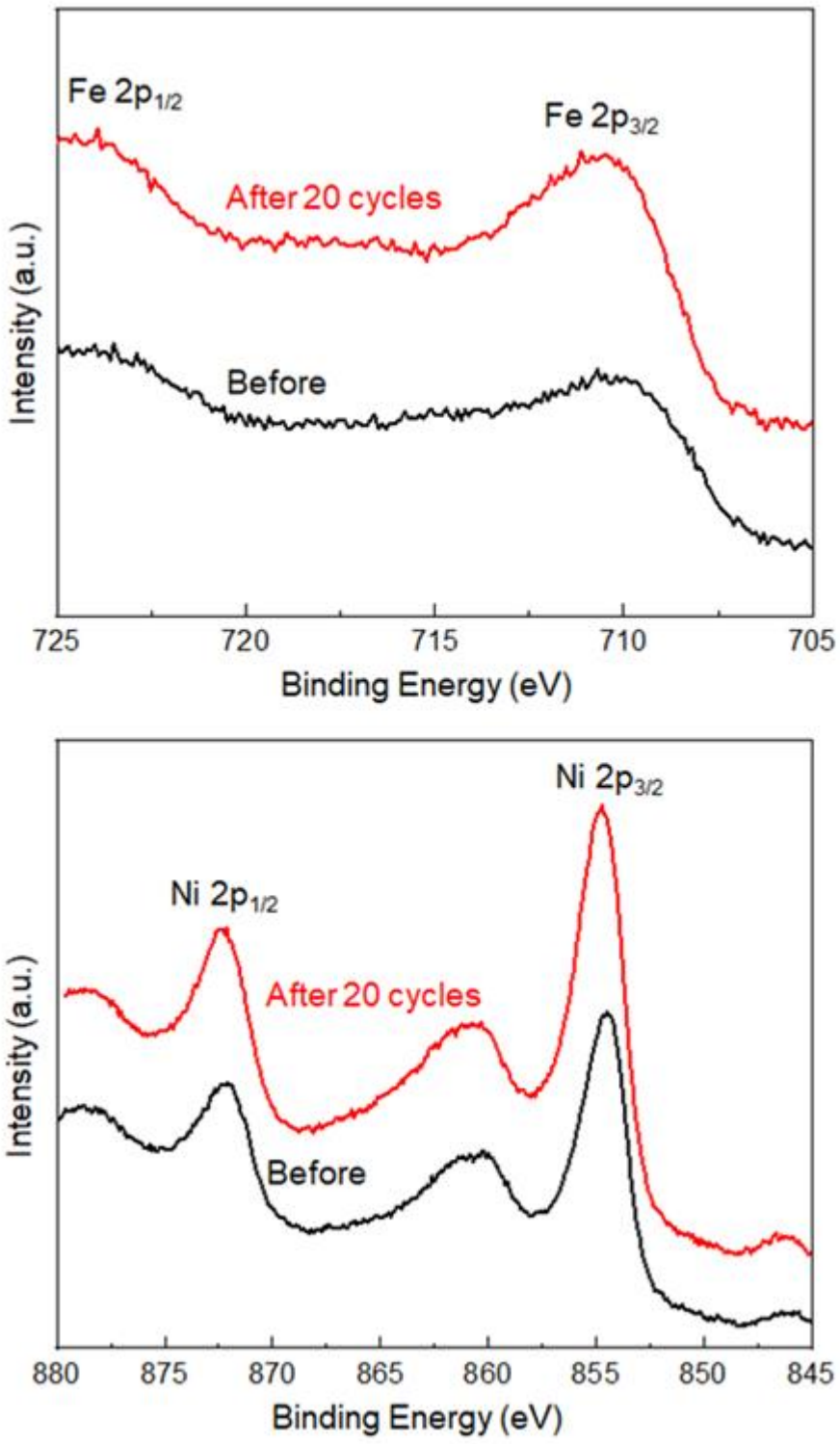

Figure 3.20. Fe 2p and Ni 2p XPS spectra of **Ni5(Fe5/Ni5)$_1$** before/after 20 cycles CV measurements.

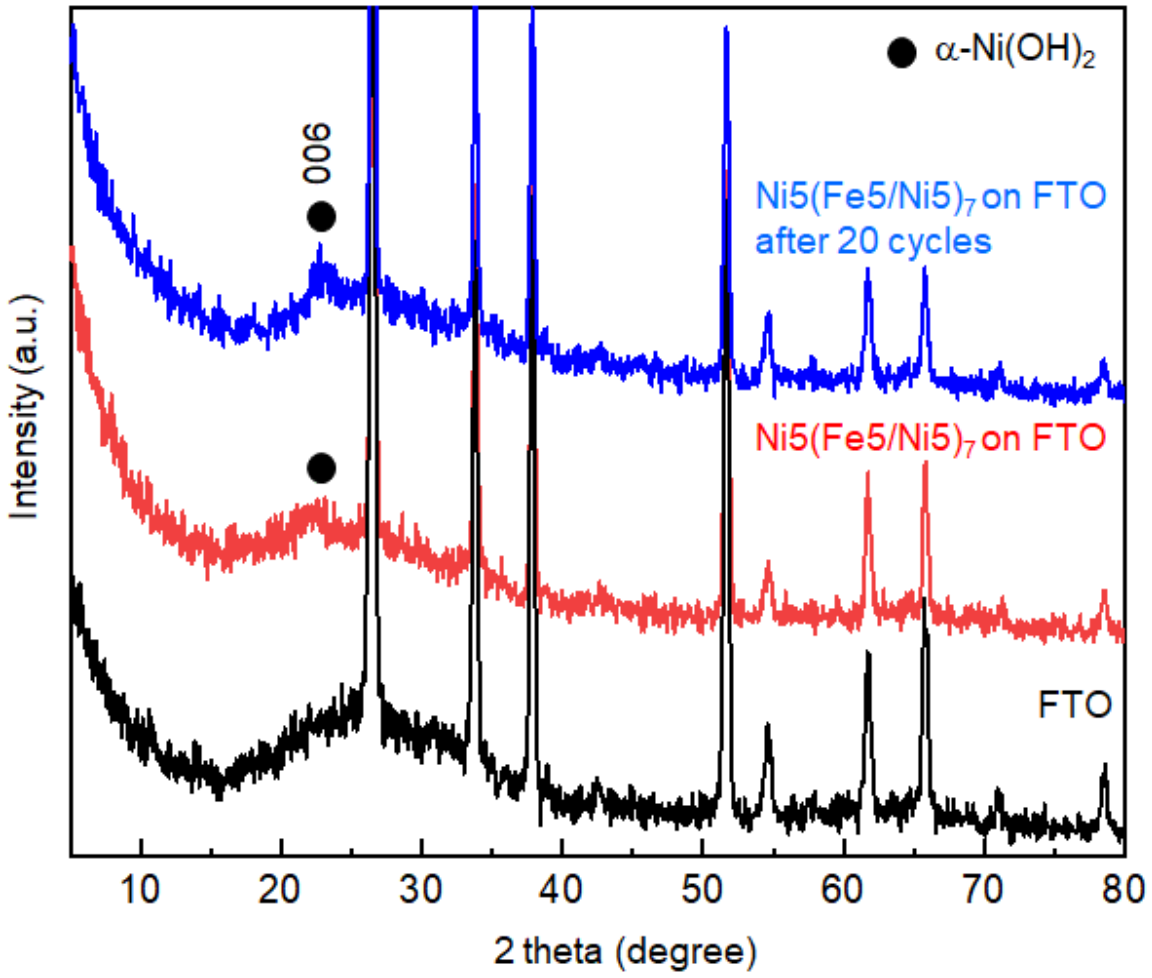

Figure 3.21. XRD patterns of a FTO substrate and **Ni5(Fe5/Ni5)$_7$** deposited on FTO substrate before/after 20 cycles CV measurements.

The sequenced-SILAR method was used to deposit Ni(OH)$_2$/FeOOH heterostructures on Ni foam. FE-SEM observation of **Ni5(Fe5/Ni5)$_1$** deposited on the Ni foam showed the presence of a homogeneously deposited layer on Ni wires (Figure 3.22). The absence of particulate products indicates that the rinse process completely removed the unwanted Ni- or Fe-containing solution from the pores in the Ni foam. As shown in Figure 3.23, the polarization current density was enhanced by approximately 10 times at 1.5 V in comparison with the heterostructure deposited on FTO substrate due to the increased specific surface area. Thus, the sequenced-SILAR method was applicable for the deposition of nanoscale heterostructures on porous substrates. The overpotential value (234 mV) at 10 mA cm^{-2} is comparable or superior to those of state-of-the-art Ni/Fe binary (oxy)hydroxide catalysts obtained by multiple, complex synthetic processes (Table 3.1).[52-57] Thus, the sequenced-SILAR method provided a facile route to the fabrication of a Ni(OH)$_2$/FeOOH-based nanoscale heterostructure with controlled OER activity.

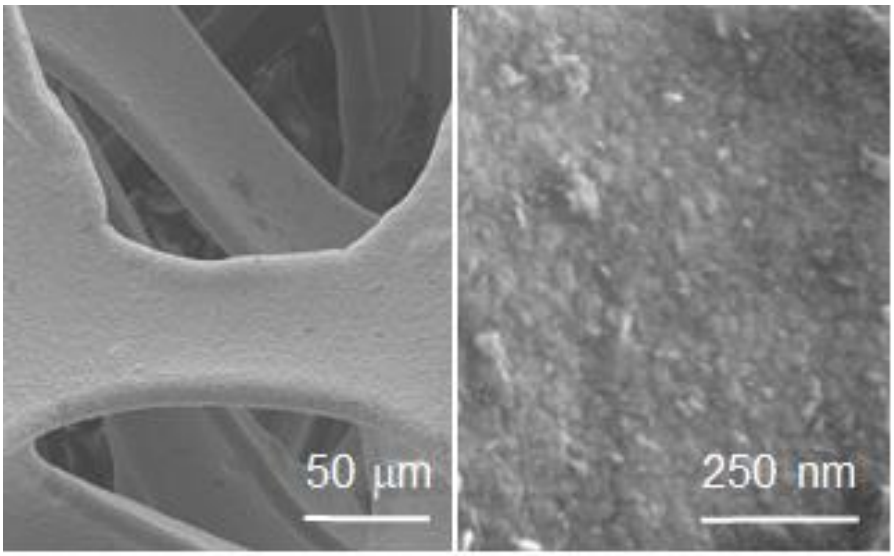

Figure 3.22. The SEM images of **Ni5(Fe5/Ni5)$_1$** deposited on Ni foam.

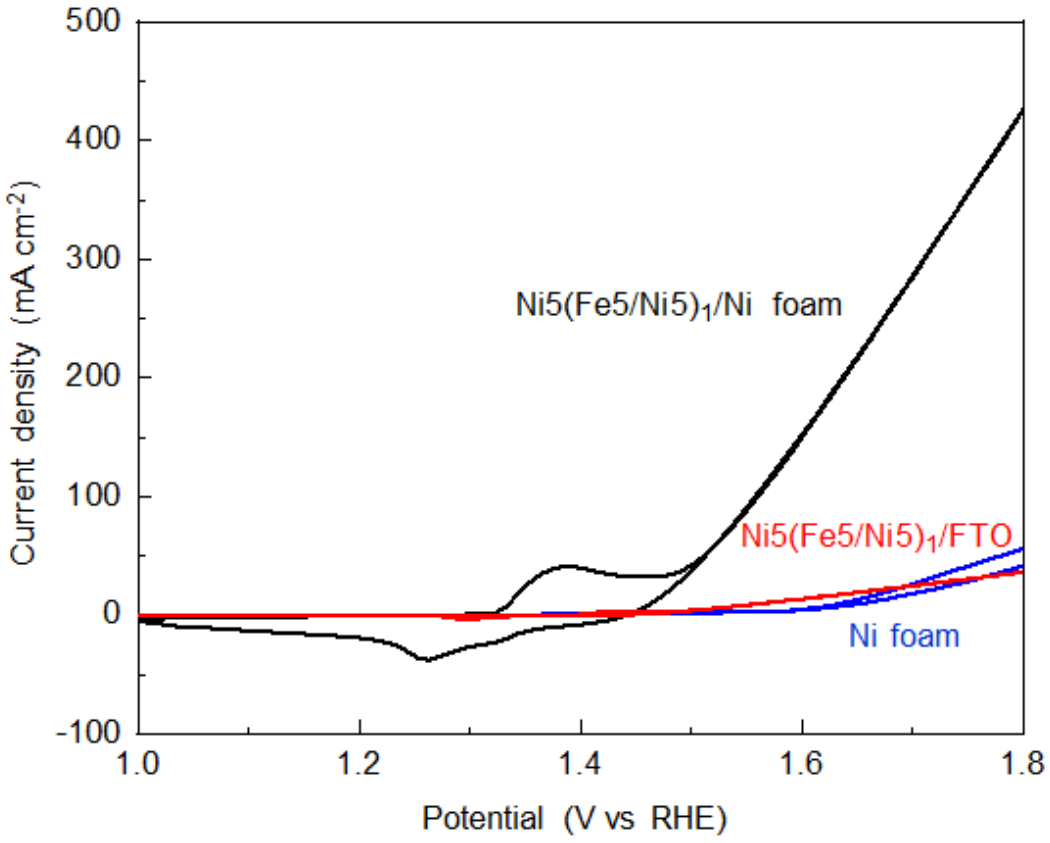

Figure 3.23. CV curves for **Ni5(Fe5/Ni5)$_1$** deposited on FTO substrate and Ni foam.

Table 3.1. Summarized OER activity of state-of-art homogeneous NiFe binary catalysts deposited on Ni foam in 1.0 M KOH electrolyte from the literature.

	Overpotential (mV, 10 mA cm^{-2})	**References**
Chapter 3	234	
***J. Mater. Chem. A*, 7, 21722, 2019.**	239	52
***ACS Energy Lett.*, 4, 3, 622, 2019**	219	53
***Adv. Mater.*, 30, 10, 1706279, 2018.**	230	54
***ACS Sustainable Chem. Eng.*, 7, 11, 10035, 2019.**	240	55
***ACS Sustainable Chem. Eng.*, 6, 15411, 2018.**	224	56
***RSC Adv.*, 10, 43, 25426, 2020.**	270	57

Subsequently, the OER activity depending on the deposition sequence and conditions was investigated. Figure 3.24 summarizes the overpotential values at 10 mA cm^{-2} based on the polarization curve of the samples produced with various deposition sequences (Figure 3.25). First, it was found from the series of $Ni(OH)_2$ single component samples (**Ni1** to **Ni30**) that the overpotential value of the $Ni(OH)_2$ layer decreased with an increase in the deposition cycle number up to 7 times, and then gradually increased (see also Figure 3.25). If a growth rate of 2 nm per deposition cycle is assumed based on the TEM analysis, the thickness would reach ~14 nm for **Ni7**. The charge transfer efficiency, i.e. catalytic activity, was suppressed in the thicker layer presumably due to the low electrical conductivity of α-$Ni(OH)_2$.[58] Second, a significant improvement of the overpotential was observed in the series of samples based on the $Ni(OH)_2$/FeOOH heterostructures, **Ni1(Fe1/Ni1)$_7$**, **Ni3(Fe3/Ni3)$_2$**, and **Ni5(Fe5/Ni5)$_1$**. Furthermore, a trend can be seen in these samples where the overpotential value improved with an increase in the number of deposition cycles for each layer. Ni-sites could be responsible for the catalytically active sites for OER in Ni/Fe binary (oxy)hydroxide systems.[11, 59-60] Thus, the trend can be interpreted as that the catalytic activity is improved in the order of the total number of $Ni(OH)_2$ deposition cycles, i.e. total number of Ni-active sites in the deposited film. Therefore, the best performance observed in **Ni5(Fe5/Ni5)$_1$** could be interpreted as that the $Ni(OH)_2$/FeOOH coupling effect is not localized only in the interface region. Namely, since the 5-cycle $Ni(OH)_2$ deposition in the given sequence would yield layers of ~10 nm thickness (Figure 3.14), the interfacial coupling effect may even affect the catalytic activity at Ni^{2+} sites located about 10 nm from the heterojunction. Such a long-range influence from

interfacial coupling has not been considered in the previous studies focusing on electrocatalysis based on heterostructure.[20-23] Thus, our finding may shed some insights to understand and design catalytic activities of heterostructured catalysts.

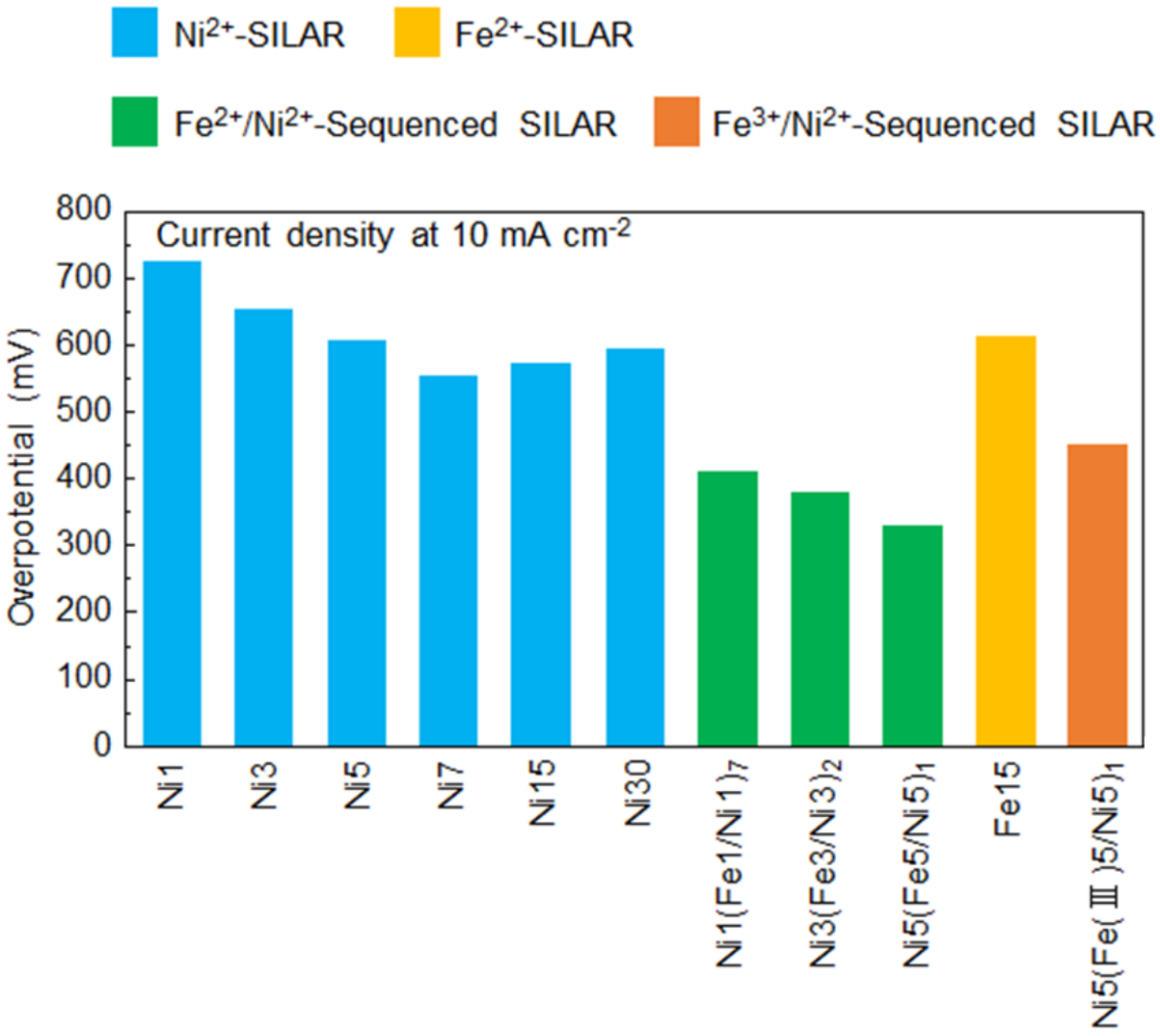

Figure 3.24. Summarized OER overpotentials at 10 mA cm^{-2} after 20 cycles CV scans.

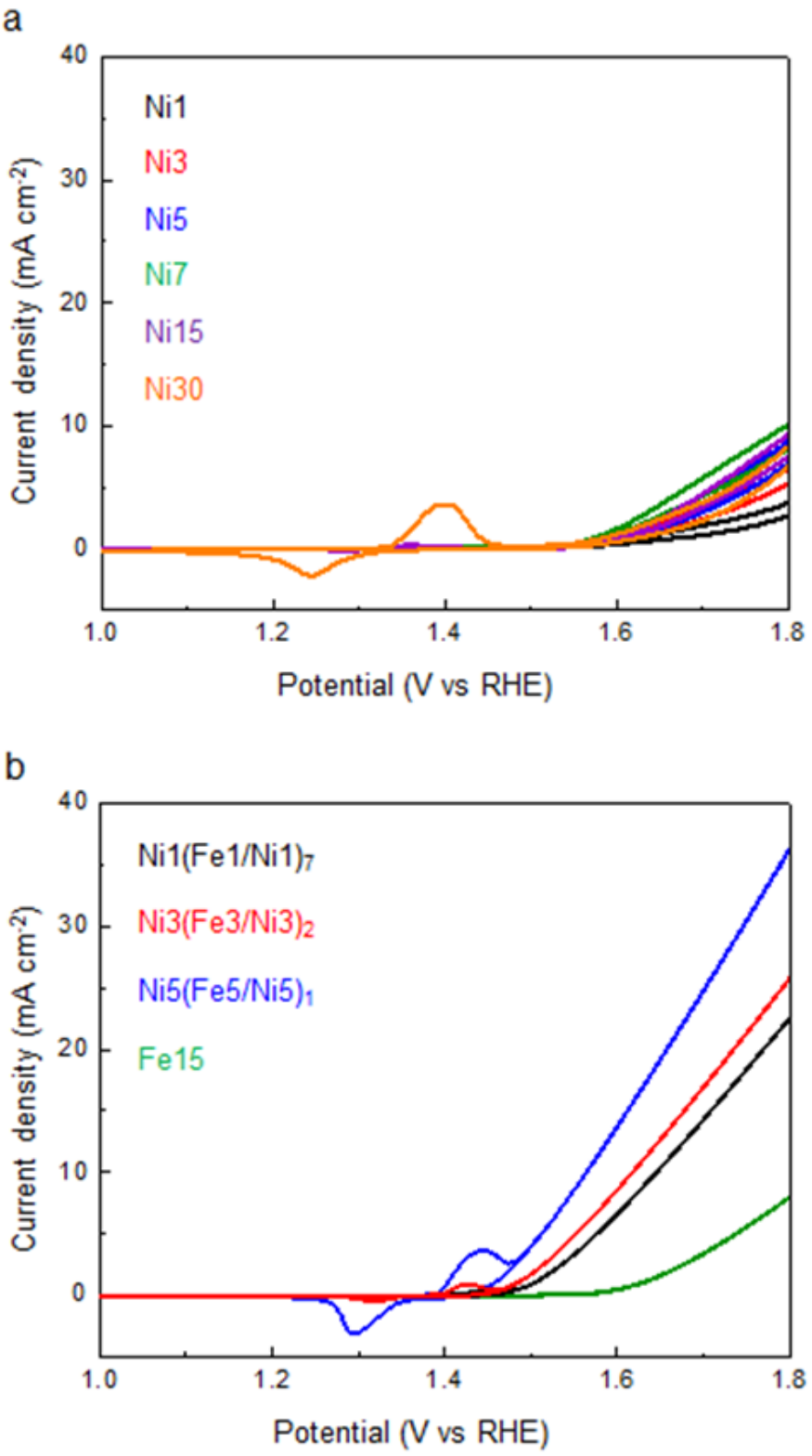

Figure 3.25. (a) CV curves for **Ni1-30**, (b) **Ni1(Fe1/Ni1)$_7$**, **Ni3(Fe3/Ni3)$_2$**, **Ni5(Fe5/Ni5)$_1$**, and **Fe15** deposited on FTO substrate.

3.3.4 Sequenced-SILAR deposition with a Fe^{3+} precursor.

Lastly, as a control experiment, the sequenced-SILAR process using the Fe^{3+} precursor solution was conducted to verify the hypothesis that the use of Fe^{2+} as a precursor solution is key to obtaining nanoscale heterostructures (Figure 3.26).

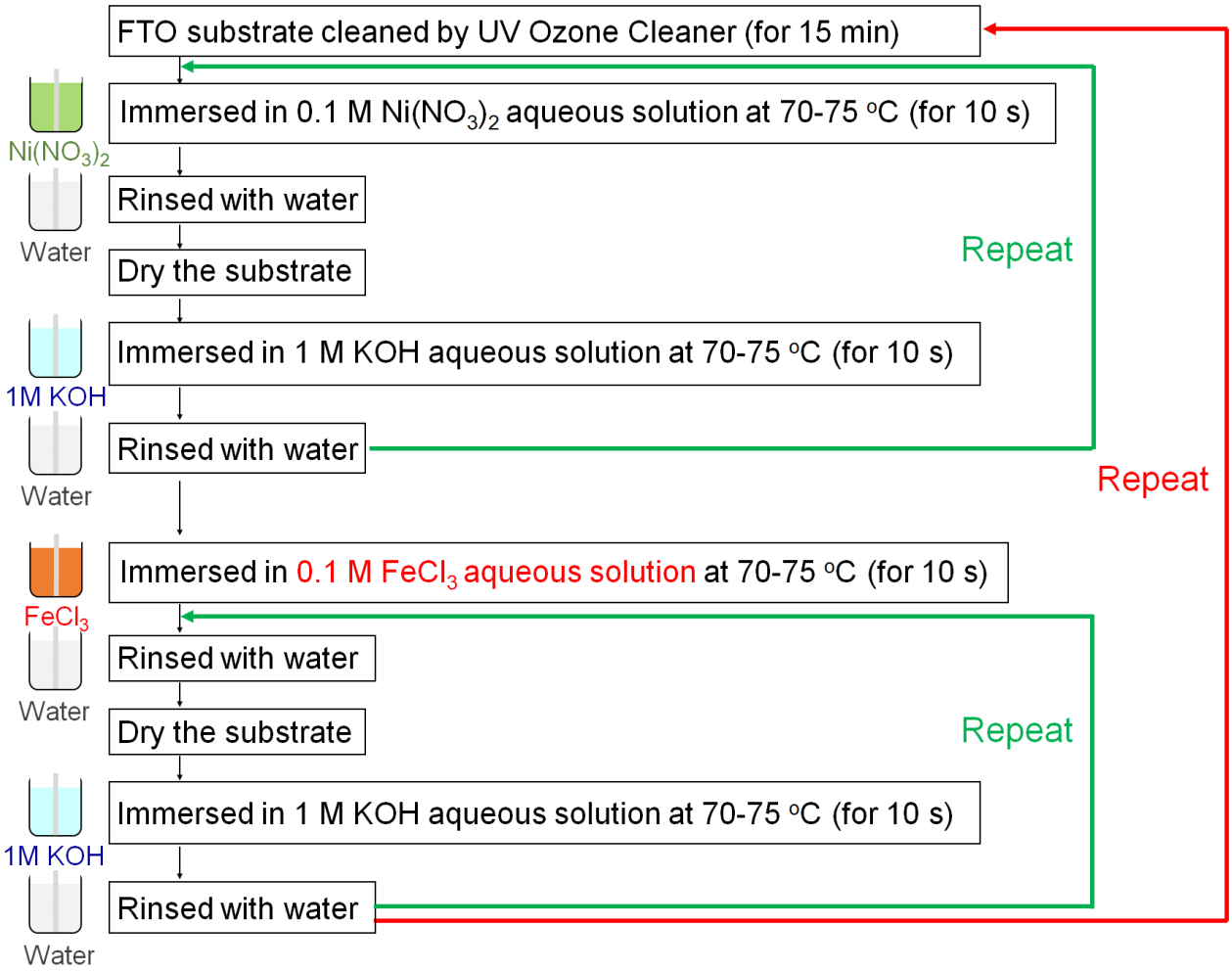

Figure 3.26. Flowchart of sequenced-SILAR procedure with a Fe^{3+} precursor.

For this purpose, Fe^{3+} solution was employed, while the other parameters remained the same as those employed in the fabrication of **Ni5(Fe5/Ni5)$_1$**. The sample, denoted as **Ni5(Fe(III)5/Ni5)$_1$**, showed an overpotential of 450 mV at 10 mA cm^{-2}, which is 120 mV worse than **Ni5(Fe5/Ni5)$_1$** synthesized with the Fe^{2+} precursor (also see Figure 3.24 and Figure 3.27).

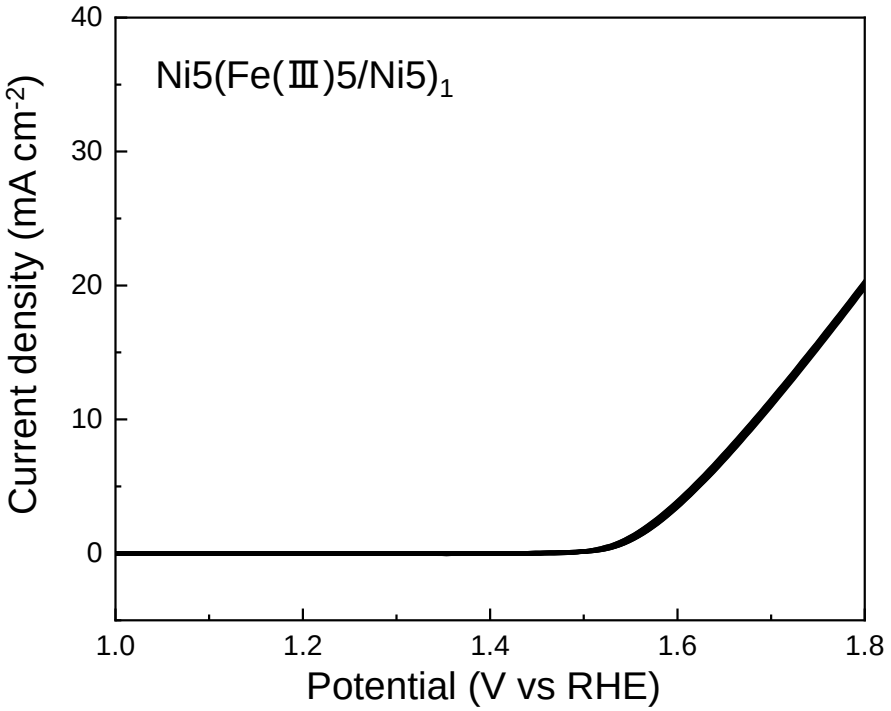

Figure 3.27. CV curve for **Ni5(Fe(III)5/Ni5)$_1$** deposited on FTO substrate.

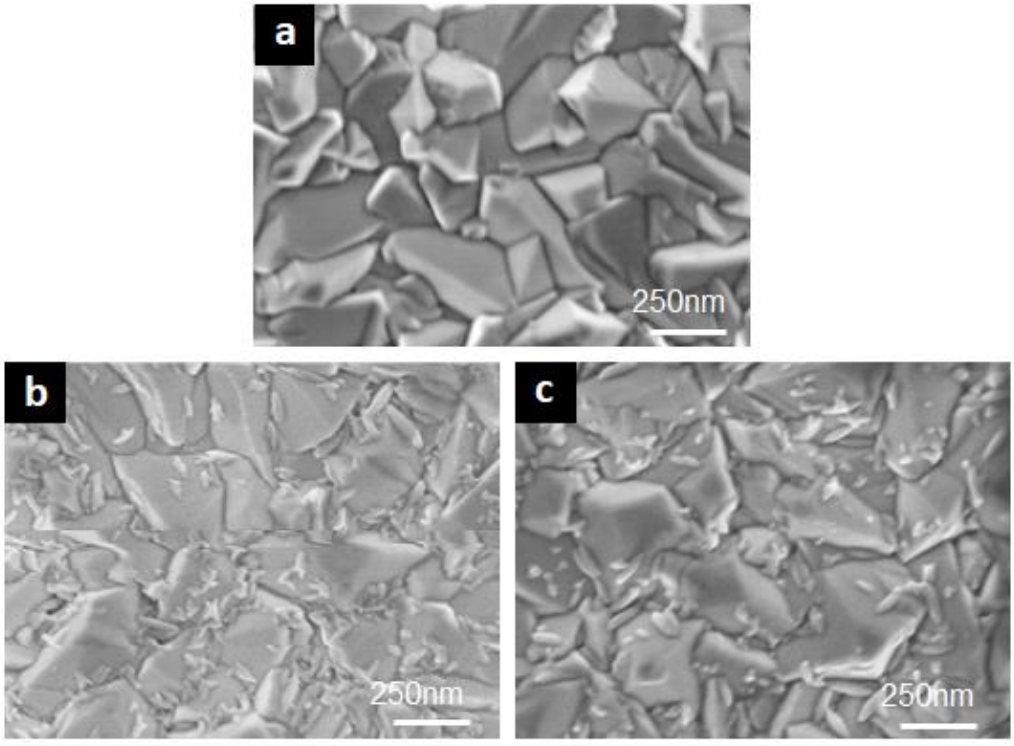

Figure 3.28. SEM images of (a) FTO substrate, (b) **Fe(III)15** and (c) **Ni5(Fe(III)5/Ni5)$_1$** on FTO substrate.

SEM observation of **Ni5(Fe(III)5/Ni5)$_1$** revealed that spindle-shaped particles of approximately 20-100 nm in size were sparsely formed (Figure 3.28 (c)). Such particles were also formed when the deposition was performed with only the Fe^{3+} precursor (**Fe(III)15**). The observed spindle-shaped particles are probably based on FeOOH phases.[61-62] Moreover, the Sn $3p_{3/2}$ peak rather than the Fe $2p_{3/2}$ peak was dominant in the Fe 2p spectral region of the XPS spectra of **Ni5(Fe(III)5/Ni5)$_1$** (Figure 3.29), which is responsible for the low coverage of FeOOH layer due to the formation of the isolated spindle particles. This would result in a lack of dense $Ni(OH)_2$/FeOOH heterojunctions, weakening the effects of the interfacial coupling on OER activity. As it was addressed previously, **Ni5(Fe5/Ni5)$_1$**, synthesized with the Fe^{2+} precursor, turned to be a Fe^{3+}-dominant state after the 20 cycles CV scans, while retaining the high catalytic activity. Thus, it is propose that the lower catalytic activity of **Ni5(Fe(III)5/Ni5)$_1$** than that of **Ni5(Fe5/Ni5)$_1$** should come from the lower density of heterointerface, instead of the difference in the valence state of ion species in the heterostructures. Thus, the choice of the Fe^{2+} precursor is critical for obtaining highly catalyzed $Ni(OH)_2$/FeOOH heterostructures via the sequenced-SILAR method. A true understanding of the formation mechanism of dense amorphous FeOOH layer via the Fe^{2+}-route remains challenging because of the complex chemistry regarding nucleation and growth of inorganic layers at solid-liquid interfaces. Nevertheless, it can be hypothesized that the precipitation reactions depending on the precursors play a key role as follows. If the Fe^{3+} precursor is used, crystalline FeOOH nuclei are immediately formed by reactions between adsorbed Fe^{3+} and OH^- at the initial SILAR cycle. The nuclei are not densely formed on the surface. Fe^{3+} cations provided in the subsequent SILAR cycles are expensed by the growth rather than nucleation, thus leading to the formation of sparsely distributed nanoparticles. In contrast, precipitation reactions of the Fe^{2+} precursor involve the formation of $Fe(OH)_2$ as an intermediate compound. The temporal formation of $Fe(OH)_2$ presumably suppress the nucleation of crystalline FeOOH nuclei as well as the subsequent growth into nanoparticles. This results in the formation of the dense and amorphous FeOOH layer. Other than the valency of the iron precursors focused in the present study, there remains various synthetic parameters to be considered for further controlling the heterostructures as well as catalytic properties. These include precursor types (chlorides, sulphates, and nitrates, etc) and concentrations as well as reaction temperatures and durations. Optimizing these parameters will not only improve catalytic properties but also open up the possibility of the sequencing SILAR routes to a variety of functional heterostructures. For example, recently, a heterostructure based on nickel-decorated transition metal oxide/ceria has been found to offer remarkable bifunctional catalytic activity for OER and hydrogen evolution reactions because of the formation of high valency Ni at the interface.[24] The sequencing SILAR might be used to obtain the heterostructure with more adequately controlled nanoscale structures.

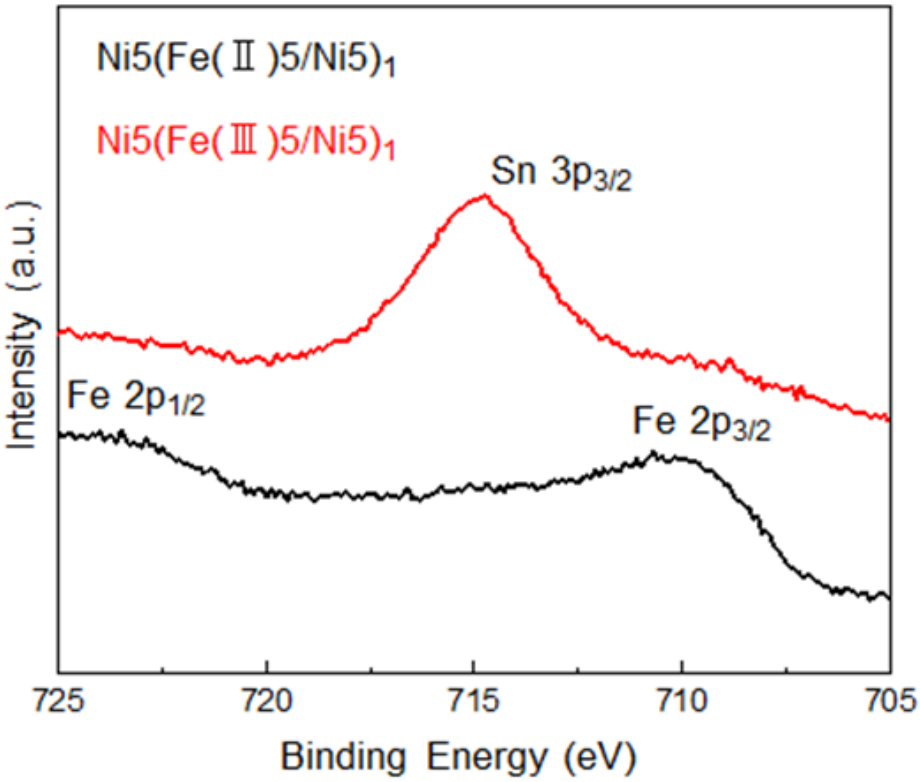

Figure 3.29. Fe 2p XPS spectra of **Ni5(Fe(II)5/Ni5)$_1$** and **Ni5(Fe(III)5/Ni5)$_1$** deposited on FTO substrate.

3.4 Conclusion

A sequenced-SILAR method was developed for fabricating nanoscale $Ni(OH)_2$/FeOOH heterostructures. Electrochemical OER measurements under alkaline conditions revealed that $Ni(OH)_2$/FeOOH with dense heterojunctions had low overpotentials of 330 and 234 mV at 10 mA cm^{-2} on flat FTO and Ni foam, respectively. Furthermore, it was found that the design of the deposition sequences and conditions was crucial for optimizing the catalytic activity in the heterostructure. The key for successfully controlling the LbL deposition of $Ni(OH)_2$ and FeOOH layers relies on the utilization of the Fe^{2+} precursor solution. Otherwise, dense heterojunctions cannot be obtained because of the formation of isolated FeOOH nanoparticles. The sequenced-SILAR method, potentially employed to explore other heterostructured catalysts composed of diverse metallic and anionic species, will contribute to the further development of catalysts for sustainable energy conversion.

https://doi.org/10.1021/acsaem.1c01505

References

1. Seh, Z. W.; Kibsgaard, J.; Dickens, C. F.; Chorkendorff, I.; Nørskov, J. K.; Jaramillo, T. F., Combining Theory and Experiment in Electrocatalysis: Insights into Materials Design. *Science* **2017,** *355*, eaad4998.

2. Cook, T. R.; Dogutan, D. K.; Reece, S. Y.; Surendranath, Y.; Teets, T. S.; Nocera, D. G., Solar Energy Supply and Storage for the Legacy and Nonlegacy Worlds. *Chem. Rev.* **2010,** *110*, 6474-6502.

3. Dresp, S.; Dionigi, F.; Klingenhof, M.; Strasser, P., Direct Electrolytic Splitting of Seawater: Opportunities and Challenges. *ACS Energy Lett.* **2019,** *4*, 933-942.

4. Suntivich, J.; May, K. J.; Gasteiger, H. A.; Goodenough, J. B.; Shao-Horn, Y., A Perovskite Oxide Optimized for Oxygen Evolution Catalysis from Molecular Orbital Principles. *Science* **2011,** *334*, 1383-1385.

5. Suen, N.-T.; Hung, S.-F.; Quan, Q.; Zhang, N.; Xu, Y.-J.; Chen, H. M., Electrocatalysis for the Oxygen Evolution Reaction: Recent Development and Future Perspectives. *Chem. Soc. Rev.* **2017,** *46*, 337-365.

6. Walter, M. G.; Warren, E. L.; McKone, J. R.; Boettcher, S. W.; Mi, Q.; Santori, E. A.; Lewis, N. S., Solar Water Splitting Cells. *Chem. Rev.* **2010,** *110*, 6446-6473.

7. Shan, J.; Guo, C.; Zhu, Y.; Chen, S.; Song, L.; Jaroniec, M.; Zheng, Y.; Qiao, S.-Z., Charge-Redistribution-Enhanced Nanocrystalline Ru@IrO_x Electrocatalysts for Oxygen Evolution in Acidic Media. *Chem* **2019,** *5*, 445-459.

8. Cao, L.; Luo, Q.; Chen, J.; Wang, L.; Lin, Y.; Wang, H.; Liu, X.; Shen, X.; Zhang, W.; Liu, W.; Qi, Z.; Jiang, Z.; Yang, J.; Yao, T., Dynamic Oxygen Adsorption on Single-Atomic Ruthenium Catalyst with High Performance for Acidic Oxygen Evolution Reaction. *Nat. Commun.* **2019,** *10*, 4849.

9. Ma, C.; Sun, W.; Qamar Zaman, W.; Zhou, Z.; Zhang, H.; Shen, Q.; Cao, L.; Yang, J., Lanthanides Regulated the Amorphization–Crystallization of IrO_2 for Outstanding OER Performance. *ACS Appl. Mater. Interfaces* **2020,** *12*, 34980-34989.

10. Corrigan, D. A.; Conell, R. S.; Fierro, C. A.; Scherson, D. A., In-situ Moessbauer Study of Redox Processes in a Composite Hydroxide of Iron and Nickel. *J. Phys. Chem.* **1987,** *91*, 5009-5011.

11. Trotochaud, L.; Young, S. L.; Ranney, J. K.; Boettcher, S. W., Nickel–Iron Oxyhydroxide Oxygen-Evolution Electrocatalysts: The Role of Intentional and Incidental Iron Incorporation. *J. Am. Chem. Soc.* **2014,** *136*, 6744-6753.

12. Friebel, D.; Louie, M. W.; Bajdich, M.; Sanwald, K. E.; Cai, Y.; Wise, A. M.; Cheng, M.-J.; Sokaras, D.; Weng, T.-C.; Alonso-Mori, R.; Davis, R. C.; Bargar, J. R.; Nørskov, J. K.; Nilsson, A.; Bell, A. T., Identification of Highly Active Fe Sites in (Ni,Fe)OOH for Electrocatalytic Water Splitting. *J. Am. Chem. Soc.* **2015,** *137*, 1305-1313.

13. Stevens, M. B.; Trang, C. D. M.; Enman, L. J.; Deng, J.; Boettcher, S. W., Reactive Fe-Sites in Ni/Fe (Oxy)hydroxide Are Responsible for Exceptional Oxygen Electrocatalysis Activity. *J. Am Chem. Soc.* **2017,** *139*, 11361-11364.

14. Roy, C.; Sebok, B.; Scott, S. B.; Fiordaliso, E. M.; Sørensen, J. E.; Bodin, A.; Trimarco, D. B.; Damsgaard, C. D.; Vesborg, P. C. K.; Hansen, O.; Stephens, I. E. L.; Kibsgaard, J.; Chorkendorff, I., Impact of Nanoparticle Size and Lattice Oxygen on Water Oxidation on $NiFeO_xH_y$. *Nat. Catal.* **2018,** *1*, 820-829.

15. Wang, Q.; Shang, L.; Shi, R.; Zhang, X.; Zhao, Y.; Waterhouse, G. I. N.; Wu, L.-Z.; Tung, C.-H.; Zhang, T., NiFe Layered Double Hydroxide Nanoparticles on Co,N-Codoped Carbon Nanoframes as Efficient Bifunctional Catalysts for Rechargeable Zinc–Air Batteries. *Adv. Energy Mater.* **2017,** *7*, 1700467.
16. Yu, L.; Yang, J. F.; Guan, B. Y.; Lu, Y.; Lou, X. W., Hierarchical Hollow Nanoprisms Based on Ultrathin Ni-Fe Layered Double Hydroxide Nanosheets with Enhanced Electrocatalytic Activity towards Oxygen Evolution. *Angew. Chem. Int. Ed.* **2018,** *57*, 172-176.
17. Song, F.; Hu, X., Exfoliation of Layered Double Hydroxides for Enhanced Oxygen Evolution Catalysis. *Nat. Commun.* **2014,** *5*, 4477.
18. Li, Z.; Wang, Z.; Xi, S.; Zhao, X.; Sun, T.; Li, J.; Yu, W.; Xu, H.; Herng, T. S.; Hai, X.; Lyu, P.; Zhao, M.; Pennycook, S. J.; Ding, J.; Xiao, H.; Lu, J., Tuning the Spin Density of Cobalt Single-Atom Catalysts for Efficient Oxygen Evolution. *ACS Nano* **2021**.
19. Guan, S.; Fu, X.; Lao, Z.; Jin, C.; Peng, Z., NiS–MoS_2 Hetero-nanosheet Array Electrocatalysts for Efficient Overall Water Splitting. *Sustain. Energy Fuels* **2019,** *3*, 2056-2066.
20. Zhai, P.; Zhang, Y.; Wu, Y.; Gao, J.; Zhang, B.; Cao, S.; Zhang, Y.; Li, Z.; Sun, L.; Hou, J., Engineering Active Sites on Hierarchical Transition Bimetal Oxides/Sulfides Heterostructure Array Enabling Robust Overall Water Splitting. *Nat. Commun.* **2020,** *11*, 5462.
21. Zhang, J.; Qian, J.; Ran, J.; Xi, P.; Yang, L.; Gao, D., Engineering Lower Coordination Atoms onto NiO/Co_3O_4 Heterointerfaces for Boosting Oxygen Evolution Reactions. *ACS Catal.* **2020,** *10*, 12376-12384.
22. Guo, Y.; Tang, J.; Henzie, J.; Jiang, B.; Xia, W.; Chen, T.; Bando, Y.; Kang, Y.-M.; Hossain, M. S. A.; Sugahara, Y.; Yamauchi, Y., Mesoporous Iron-doped MoS_2/$CoMo_2S_4$ Heterostructures through Organic–Metal Cooperative Interactions on Spherical Micelles for Electrochemical Water Splitting. *ACS Nano* **2020,** *14*, 4141-4152.
23. Liang, Q.; Zhong, L.; Du, C.; Luo, Y.; Zhao, J.; Zheng, Y.; Xu, J.; Ma, J.; Liu, C.; Li, S.; Yan, Q., Interfacing Epitaxial Dinickel Phosphide to 2D Nickel Thiophosphate Nanosheets for Boosting Electrocatalytic Water Splitting. *ACS Nano* **2019,** *13*, 7975-7984.
24. Long, X.; Lin, H.; Zhou, D.; An, Y.; Yang, S., Enhancing Full Water-Splitting Performance of Transition Metal Bifunctional Electrocatalysts in Alkaline Solutions by Tailoring CeO_2–Transition Metal Oxides–Ni Nanointerfaces. *ACS Energy Lett.* **2018,** *3*, 290-296.
25. Chen, Z.; Ju, M.; Sun, M.; Jin, L.; Cai, R.; Wang, Z.; Dong, L.; Peng, L.; Long, X.; Huang, B.; Yang, S., TM LDH Meets Birnessite: A 2D-2D Hybrid Catalyst with Long-Term Stability for Water Oxidation at Industrial Operating Conditions. *Angew. Chem. Int. Ed.* **2021,** *60*, 9699-9705.
26. Long, X.; Qiu, W.; Wang, Z.; Wang, Y.; Yang, S., Recent Advances in Transition Metal–based Catalysts with Heterointerfaces for Energy Conversion and Storage. *Mater. Today Chem.* **2019,** *11*, 16-28.
27. Niu, S.; Sun, Y.; Sun, G.; Rakov, D.; Li, Y.; Ma, Y.; Chu, J.; Xu, P., Stepwise Electrochemical Construction of FeOOH/$Ni(OH)_2$ on Ni Foam for Enhanced Electrocatalytic Oxygen Evolution. *ACS Appl. Energy Mater.* **2019,** *2*, 3927-3935.
28. Zhu, K.; Luo, W.; Zhu, G.; Wang, J.; Zhu, Y.; Zou, Z.; Huang, W., Interface-Engineered $Ni(OH)_2$/β-like FeOOH Electrocatalysts for Highly Efficient and Stable Oxygen Evolution Reaction. *Chem Asian J* **2017,** *12*,

2720-2726.
29. Cheng, X.; Yuan, J.; Cao, J.; Lei, C.; Yang, B.; Li, Z.; Zhang, X.; Yuan, C.; Lei, L.; Hou, Y., Strongly Coupling of Amorphous/crystalline Reduced FeOOH/α-$Ni(OH)_2$ Heterostructure for Extremely Efficient Water Oxidation at Ultra-high Current Density. *J. Colloid Interface Sci.* **2020,** *579*, 340-346.
30. Lindroos, S.; Leskelä, M., Successive Ionic Layer Adsorption and Reaction (SILAR) and Related Sequential Solution-Phase Deposition Techniques. In *Solution Processing of Inorganic Materials*, 2008; pp 239-282.
31. Nath, A. R.; Sandhyarani, N., SILAR Deposited Nickel Sulphide-nickel Hydroxide Nanocomposite for High Performance Asymmetric Supercapacitor. *Electrochim Acta* **2020,** *356*, 136844.
32. Jana, M.; Saha, S.; Samanta, P.; Murmu, N. C.; Kim, N. H.; Kuila, T.; Lee, J. H., Growth of Ni–Co Binary Hydroxide on a Reduced Graphene Oxide Surface by a Successive Ionic Layer Adsorption and Reaction (SILAR) Method for High Performance Asymmetric Supercapacitor Electrodes. *J. Mater. Chem. A* **2016,** *4*, 2188-2197.
33. Su, Z.; Sun, K.; Han, Z.; Liu, F.; Lai, Y.; Li, J.; Liu, Y., Fabrication of Ternary Cu–Sn–S Sulfides by a Modified Successive Ionic Layer Adsorption and Reaction (SILAR) Method. *J. Mater. Chem.* **2012,** *22*, 16346-16352.
34. Wang, Q.; Zhong, L.; Sun, J.; Shen, J., A Facile Layer-by-Layer Adsorption and Reaction Method to the Preparation of Titanium Phosphate Ultrathin Films. *Chem. Mater.* **2005,** *17*, 3563-3569.
35. Babar, P. T.; Lokhande, A. C.; Shim, H. J.; Gang, M. G.; Pawar, B. S.; Pawar, S. M.; Kim, J. H., SILAR Deposited Iron Phosphate as a Bifunctional Electrocatalyst for Efficient Water Splitting. *J. Colloid Interface Sci.* **2019,** *534*, 350-356.
36. Tolstoy, V. P.; Altangerel, B., A New "Fluoride" Synthesis Route for Successive Ionic Layer Deposition of the $Zn_xZr(OH)_yF_z \cdot nH_2O$ Nanolayers. *Mater. Lett.* **2007,** *61*, 123-125.
37. Decher, G.; Hong, J.-D., Buildup of Ultrathin Multilayer Films by a Self-assembly Process, 1 Consecutive Adsorption of Anionic and Cationic Bipolar Amphiphiles on Charged Surfaces. *Makromolekulare Chemie. Macromol Symp* **1991,** *46*, 321-327.
38. Taniguchi, A.; Taniguchi, T.; Wagata, H.; Katsumata, K.-i.; Okada, K.; Matsushita, N., Liquid-phase Atomic Layer Deposition of Crystalline Hematite without Post-growth Annealing. *CrystEngComm* **2019,** *21*, 4184-4191.
39. Taniguchi, A.; Kubota, Y.; Matsushita, N.; Ishii, K.; Uchikoshi, T., Solution-mediated Nanometric Growth of α-Fe_2O_3 with Electrocatalytic Activity for Water Oxidation. *Nanoscale Adv.* **2020,** *2*, 3933-3941.
40. Wu, Z.; Huang, X.-L.; Wang, Z.-L.; Xu, J.-J.; Wang, H.-G.; Zhang, X.-B., Electrostatic Induced Stretch Growth of Homogeneous β-$Ni(OH)_2$ on Graphene with Enhanced High-Rate Cycling for Supercapacitors. *Sci. Rep.* **2014,** *4*, 3669.
41. Wang, B.; Wu, H.; Yu, L.; Xu, R.; Lim, T.-T.; Lou, X. W., Template-free Formation of Uniform Urchin-like α-FeOOH Hollow Spheres with Superior Capability for Water Treatment. *Adv. Mater.* **2012,** *24*, 1111-1116.
42. He, Q.; Wan, Y.; Jiang, H.; Pan, Z.; Wu, C.; Wang, M.; Wu, X.; Ye, B.; Ajayan, P. M.; Song, L., Nickel Vacancies Boost Reconstruction in Nickel Hydroxide Electrocatalyst. *ACS Energy Lett.* **2018,** *3*, 1373-1380.

43. Lv, C.; Wang, X.; Gao, L.; Wang, A.; Wang, S.; Wang, R.; Ning, X.; Li, Y.; Boukhvalov, D. W.; Huang, Z.; Zhang, C., Triple Functions of $Ni(OH)_2$ on the Surface of WN Nanowires Remarkably Promoting Electrocatalytic Activity in Full Water Splitting. *ACS Catal.* **2020,** *10*, 13323-13333.

44. Zhu, J.; Guo, S.; Chu, Z.; Jin, W., CO_2-tolerant Oxygen-permeable Perovskite-type Membranes with High Permeability. *J. Mater. Chem. A* **2015,** *3*, 22564-22573.

45. Yang, Z.; Zhang, J.-Y.; Liu, Z.; Li, Z.; Lv, L.; Ao, X.; Tian, Y.; Zhang, Y.; Jiang, J.; Wang, C., "Cuju"-Structured Iron Diselenide-Derived Oxide: A Highly Efficient Electrocatalyst for Water Oxidation. *ACS Appl. Mater. Interfaces* **2017,** *9*, 40351-40359.

46. Zhao, Y.; Gu, G.; You, S.; Ji, R.; Suo, H.; Zhao, C.; Liu, F., Preparation of $Ni(OH)_2$ Nanosheets on Ni Foam via a Direct Precipitation Method for a Highly Sensitive Non-enzymatic Glucose Sensor. *RSC Adv.* **2015,** *5*, 53665-53670.

47. Zhang, J. T.; Liu, S.; Pan, G. L.; Li, G. R.; Gao, X. P., A 3D Hierarchical Porous α-$Ni(OH)_2$/graphite Nanosheet Composite as an Electrode Material for Supercapacitors. *J. Mater. Chem. A* **2014,** *2*, 1524-1529.

48. Yang, Y.; Wang, H.; Wang, L.; Ge, Y.; Kan, K.; Shi, K.; Chen, J., A Novel Gas Sensor based on Porous α-$Ni(OH)_2$ Ultrathin Nanosheet/reduced Graphene Oxide Composites for Room Temperature Detection of NO_x. *New J. Chem.* **2016,** *40*, 4678-4686.

49. Ang, H.; Hong, L., Engineering Defects into Nickel-based Nanosheets for Enhanced Water Permeability. *J. Mater. Chem. A* **2017,** *5*, 20598-20602.

50. Yu, J.; Cao, Q.; Li, Y.; Long, X.; Yang, S.; Clark, J. K.; Nakabayashi, M.; Shibata, N.; Delaunay, J.-J., Defect-Rich $NiCeO_x$ Electrocatalyst with Ultrahigh Stability and Low Overpotential for Water Oxidation. *ACS Catal.* **2019,** *9*, 1605-1611.

51. Yu, J.; Cao, Q.; Feng, B.; Li, C.; Liu, J.; Clark, J. K.; Delaunay, J.-J., Insights into the Efficiency and Stability of Cu-based Nanowires for Electrocatalytic Oxygen Evolution. *Nano Res.* **2018,** *11*, 4323-4332.

52. Cai, Z.; Bu, X.; Wang, P.; Su, W.; Wei, R.; Ho, J. C.; Yang, J.; Wang, X., Simple and Cost Effective Fabrication of 3D Porous Core–shell Ni Nanochains@NiFe Layered Double Hydroxide Nanosheet Bifunctional Electrocatalysts for Overall Water Splitting. *J. Mater. Chem. A* **2019,** *7*, 21722-21729.

53. Kou, T.; Wang, S.; Hauser, J. L.; Chen, M.; Oliver, S. R. J.; Ye, Y.; Guo, J.; Li, Y., Ni Foam-Supported Fe-Doped β-$Ni(OH)_2$ Nanosheets Show Ultralow Overpotential for Oxygen Evolution Reaction. *ACS Energy Lett.* **2019,** *4*, 622-628.

54. Chen, G.; Wang, T.; Zhang, J.; Liu, P.; Sun, H.; Zhuang, X.; Chen, M.; Feng, X., Accelerated Hydrogen Evolution Kinetics on NiFe-Layered Double Hydroxide Electrocatalysts by Tailoring Water Dissociation Active Sites. *Adv. Mater.* **2018,** *30*, 1706279.

55. Babar, P.; Lokhande, A.; Karade, V.; Pawar, B.; Gang, M. G.; Pawar, S.; Kim, J. H., Bifunctional 2D Electrocatalysts of Transition Metal Hydroxide Nanosheet Arrays for Water Splitting and Urea Electrolysis. *ACS Sustain. Chem. Eng.* **2019,** *7*, 10035-10043.

56. Zhang, Q.; Zhang, S.; Tian, Y.; Zhan, S., Ce-Directed Double-Layered Nanosheet Architecture of NiFe-Based Hydroxide as Highly Efficient Water Oxidation Electrocatalyst. *ACS Sustain. Chem. Eng.* **2018,** *6*, 15411-15418.

57. Sengupta, D.; Privitera, S. M. S.; Milazzo, R. G.; Bongiorno, C.; Scalese, S.; Lombardo, S., Ni Foam Electrode Solution Impregnated with Ni-$Fe_X(OH)_Y$ Catalysts for Efficient Oxygen Evolution Reaction in Alkaline Electrolyzers. *RSC Adv.* **2020,** *10*, 25426-25434.
58. Motori, A.; Sandrolini, F.; Davolio, G., Electrical Properties of Nickel Hydroxide for Alkaline Cell Systems. *J. Power Sources* **1994,** *48*, 361-370.
59. Louie, M. W.; Bell, A. T., An Investigation of Thin-Film Ni–Fe Oxide Catalysts for the Electrochemical Evolution of Oxygen. *J. Am. Chem. Soc.* **2013,** *135*, 12329-12337.
60. Yu, J.; Wang, J.; Long, X.; Chen, L.; Cao, Q.; Wang, J.; Qiu, C.; Lim, J.; Yang, S., Formation of FeOOH Nanosheets Induces Substitutional Doping of CeO_{2-x} with High-Valence Ni for Efficient Water Oxidation. *Adv. Energy Mater.* **2021,** *11*, 2002731.
61. Purbia, R.; Paria, S., Green Synthesis of Single-Crystalline Akaganeite Nanorods for Peroxidase Mimic Colorimetric Sensing of Ultralow-Level Vitamin B1 and Sulfide Ions. *ACS Appl. Nano Mater.* **2018,** *1*, 1236-1246.
62. Sayed, F. N.; Polshettiwar, V., Facile and Sustainable Synthesis of Shaped Iron Oxide Nanoparticles: Effect of Iron Precursor Salts on the Shapes of Iron Oxides. *Sci. Rep.* **2015,** *5*, 9733.

Chapter 4: Facile and rapid formation of $Ni(OH)_2$/FeOOH heterostructures by electrochemical deposition

Overview

The utilization of nanoscale heterostructures is a promising strategy for the development of noble metal-free catalysts towards sustainable energy conversion. Recently, an enhancement of catalytic activity for oxygen evolution reactions has been found in Ni/Fe (oxy)hydroxide heterostructures. Due to the structural and morphological complexity, however, the materials design in this system has not been established. In this chapter, the electrochemical deposition method is used for fabrication of heterostructures consisting of $Ni(OH)_2$ and FeOOH. The synthesis of transition metal hydroxides by the electrochemical deposition method is well-established, where hydroxide films can be deposited on the cathode by using metal salts as electrolytes. A strong synergistic coupling effect was obtained from the $Ni(OH)_2$/FeOOH bilayer structure prepared by FeOOH on the electrode followed by the subsequent $Ni(OH)_2$ deposition in Ni solution. The overpotential of 213 mV at 10 mA cm^{-2} and the high catalytic stability of 97% after 12 h were obtained by optimizing the deposition time of $Ni(OH)_2$ thin film on FeOOH nanomesh.

4.1 Introduction

Water electrolysis is an important technology for the production of large amounts of H_2 fuel from renewable energy generated electricity[1-3]. However, the anodic oxygen evolution reaction (OER) currently requires a huge overpotential in order to overcome the slow kinetics of OOH bond formation and OH bond breaking[4-5]. To achieve a carbon-neutral society, it is necessary to develop an electrocatalyst for oxygen evolution without using precious metals.

Ni/Fe bimetallic (oxy)hydroxide is considered a promising candidate of electrocatalyst for oxygen evolution that does not use precious metals[6-8]. Recent advances in synthesis methods have enabled the production of Ni/Fe hydroxides with a variety of nanostructures such as nanoparticles[9-10], hollow nanoprisms[11], and nanosheets[12], which exhibit catalytic activity superior to that of RuO_2- and IrO_2- based catalysts. These works rely on a common strategy of uniform arrangement of two or more metal ions in the same crystal to control the catalytic activity on a solid surface. On the other hand, recently, β-$Ni(OH)_2$ nanosheets loaded with α-FeOOH nanoparticles[13], β-FeOOH nanorods coated with $Ni(OH)_2$[14], and γ-FeOOH nanoparticles coated with α-$Ni(OH)_2$ layer on Ni[15] have been reported. In chapter 3, the sequenced-SILAR method was employed to produce α-$Ni(OH)_2$/amorphous FeOOH heterostructures[16]. These heterostructures have been shown to enhance the activity of OER catalysts. Thus, in recent years, synergistic effects through heterointerfaces have been suggested to be possible. However, while such "heterostructuring" can extend the design of catalytic materials, it requires a multistep precision synthesis process consisting of synthesis and integration of components to fabricate the desired heterostructure, which would be a bottleneck for industrial applications.

In this chapter, the fabrication of heterostructures consisting of $Ni(OH)_2$ and FeOOH by electrochemical deposition was focused on as a simple and rapid fabrication method. In general, the electrochemical deposition method is a simple, rapid, and scalable method for depositing metal hydroxide layers on conductive substrates. Here, $Ni(OH)_2$/FeOOH bilayer catalysts were prepared by a two-step electrochemical deposition method. As a result, a strong synergistic effect was obtained despite the simplicity of the bilayer design and fabrication method. The complete coverage of $Ni(OH)_2$ layer on FeOOH nanomesh was found to be the key to maximizing the catalytic activity, and the catalytic activity was suppressed when the thickness of $Ni(OH)_2$ or FeOOH layer became excessive. By optimizing the deposition time, the overpotential and catalytic durability were comparable to or superior to the state-of-the-art $Ni(OH)_2$/FeOOH catalysts.

4.2 Experimental

4.2.1 Preparation of the precursor solutions.

$FeCl_2 \cdot 4H_2O$ (99.0-102.0%) and $Ni(NO_3)_2 \cdot 6H_2O$ (98.0%) (FUJIFILM Wako Pure Chemical Corp.) were used as metal source precursors. 50 mM $FeCl_2 \cdot 4H_2O$ or $Ni(NO_3)_2 \cdot 6H_2O$ was dissolved in 30 mL of the ethanol-water mixture (ethanol: distilled water = 8:1 (volume ratio)) to prepare the precursor solution.

4.2.2 Electrochemical deposition process for the fabrication of films.

The substrates were fluorine-doped tin oxide coated glass (FTO; 10×50×1.1 mm, FTN 1.1, 10 Ω/sq, AGC Inc.) and Ni foam (99.99% purity, 1.6 mm thickness, 80-110 PPI pore size, MTI Co., Ltd. 50 mM $FeCl_2 \cdot 4H_2O$ aqueous solution (ethanol: distilled water = 8:1 (volume ratio)) was used to prepare the iron hydroxide layer by applying a voltage of 3 V to the FTO substrate or Ni foam as the cathode and the stainless-steel plate as the anode (reaction time: 0 to 150 s). Subsequently, a nickel hydroxide layer was deposited on the iron oxyhydroxide layer using the same electrochemical deposition system in 50 mM $Ni(NO_3)_2 \cdot 6H_2O$ aqueous solution (reaction time: 0 to 150 s) (Figure 4.1).

4.2.3 Characterization.

The crystalline phases of the deposited films were investigated by X-ray diffraction (XRD; X'Pert Pro MRD, CuKα, 45 kV and 40 mA, PANalytical). The surface morphologies and textures of the films were observed by scanning electron microscopy (SEM; SU-8020, Hitachi High-Technologies). X-ray photoelectron spectroscopy (XPS; JPS-9010 TR, Jeol) was conducted to study the chemical state of the samples. All measured XPS spectra were calibrated corresponding to the value of the C 1s peak at 284.4 eV using a Mg Kα X-ray source at 1253.6 eV.

4.2.4 Electrochemical measurement.

The OER measurements were performed in a 1 M KOH aqueous solution using a three-electrode configuration, with a Pt wire counter electrode and an Ag/AgCl, KCl reference electrode (Figure 4.2). All

potentials were referenced to the reversible hydrogen electrode (RHE) by the following equation: $V_{RHE} = V_{Ag/AgCl} + 0.197\ V + 0.059\ V \times pH$. Cyclic voltammetry (CV) and linear sweep voltammetry (LSV) were performed at a scan rate of 20 mV s^{-1}.

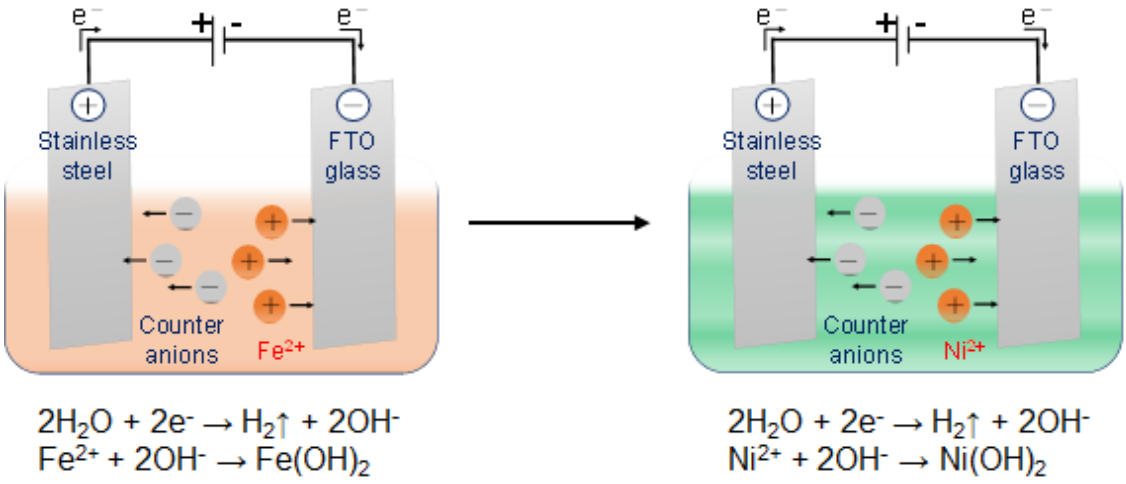

Figure 4.1. Schematic image of electrochemical deposition.

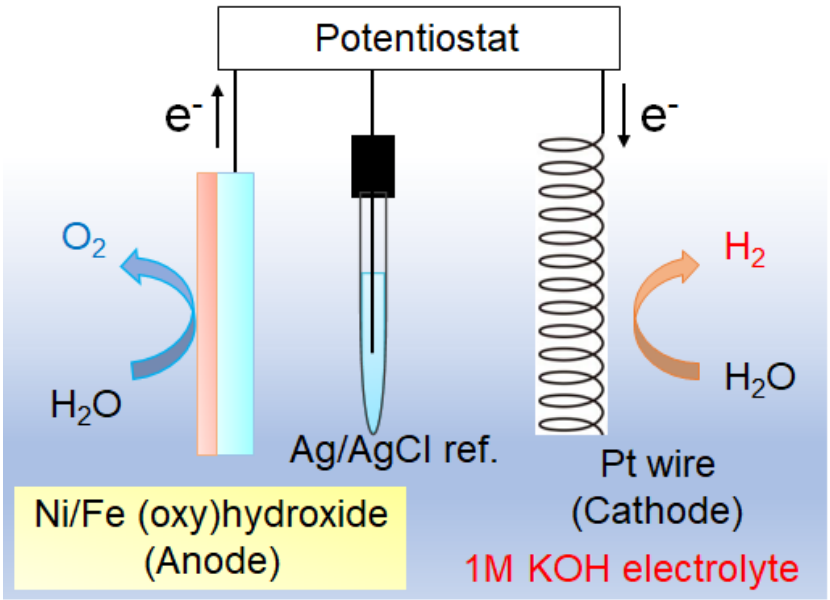

Figure 4.2. OER measurement conditions.

4.3 Results and discussion

4.3.1 Characterizations of $Ni(OH)_2$/FeOOH heterostructures by XRD and XPS.

First, the electrochemical deposition of a single layer consisting of $Ni(OH)_2$ or FeOOH on a fluorine-doped tin oxide-coated glass (FTO) substrate was investigated. In this deposition process, OH^- generated on the cathode through the electrolysis of water precipitates transition metal cations as hydroxides or oxyhydroxides. X-ray diffraction (XRD) was measured on the products formed by electrochemical deposition using $Ni(NO_3)_2$ and $FeCl_2$ solutions on a FTO substrate for 40 s. In the case of using $Ni(NO_3)_2$ and $FeCl_2$ solutions, the 101 peak of α-$Ni(OH)_2$ (JCPDS No. 38-0715[17]) and the 211 peak of β-FeOOH (JCPDS No. 75-1594[18]) were detected, respectively (Figure 4.3).

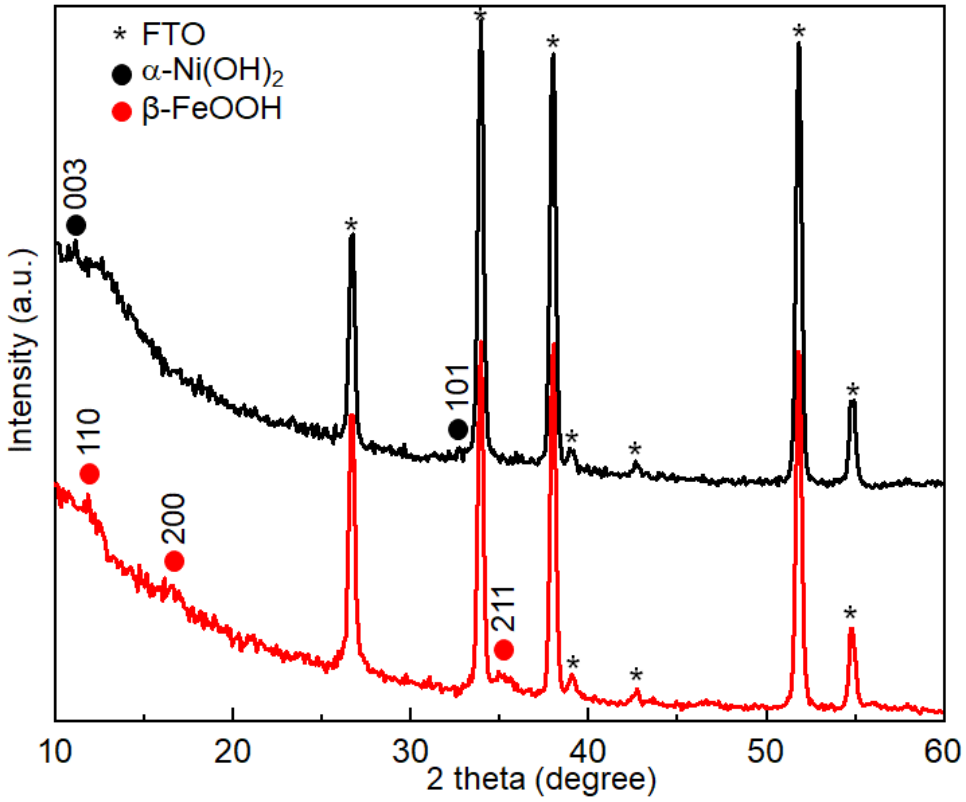

Figure 4.3. XRD patterns of α-$Ni(OH)_2$, β-FeOOH deposited on FTO substrate.

To obtain a bilayer structure as the target, two-step electrochemical deposition consisting of the initial β-FeOOH and the subsequent α-$Ni(OH)_2$ depositions were performed where the electrodeposition time for each solution was fixed at 40 s. The obtained thin films, as expected, exhibit both β-FeOOH and α-$Ni(OH)_2$ peaks, which suggests the formation of a bilayer structure (Figure 4.4).

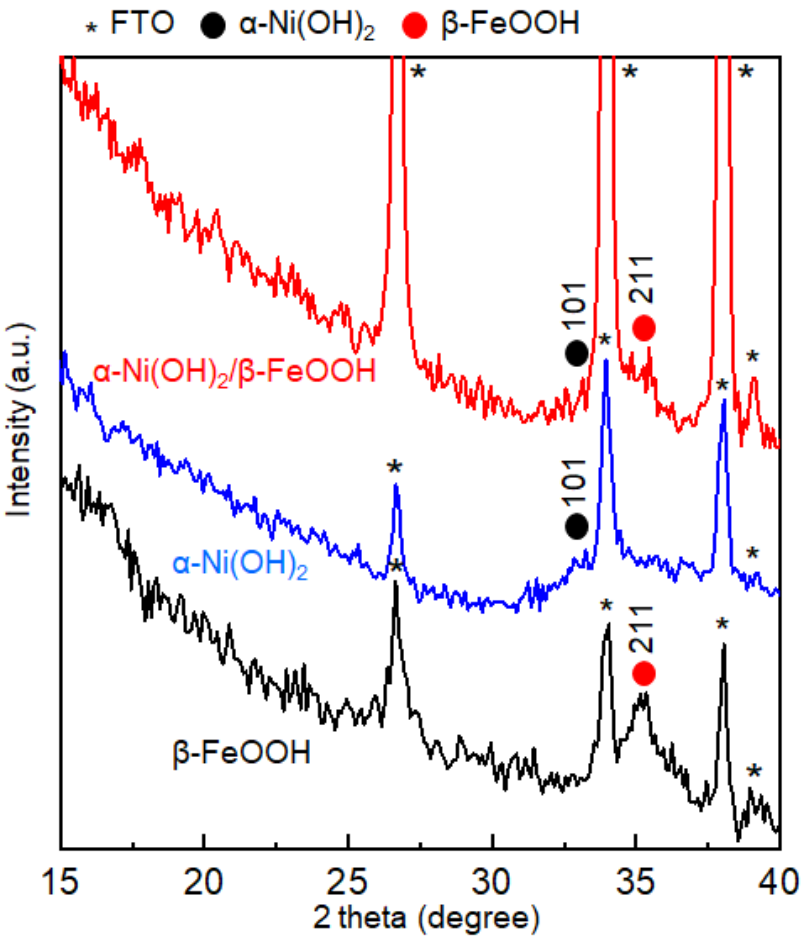

Figure 4.4. XRD patterns of α-$Ni(OH)_2$, β-FeOOH and α-$Ni(OH)_2$/β-FeOOH deposited on FTO substrate.

To further examine the formation of the heterostructure, X-ray photoelectron spectroscopy (XPS) measurements were performed. The Fe 2p XPS spectra of the samples with β-FeOOH deposited and α-$Ni(OH)_2$ deposited following the deposition of β-FeOOH are shown in Figure 4.5 (a). First, the Fe $2p_{1/2}$ and Fe $2p_{3/2}$ peaks were detected in the β-FeOOH film. The Fe $2p_{3/2}$ peak appeared at 710.5 eV, ensuring the trivalent state of the Fe species[19]. After the $Ni(OH)_2$ layer was deposited, the intensity of these peaks decreased significantly. At the same time, the Ni 2p XPS peak derived from divalent Ni species appeared (Figure 4.5 (b))[20]. In consideration of the analytical depth of XPS measurement (5-10 nm), the reduced Fe 2p peaks are related to the formation of the $Ni(OH)_2$ layer with high coverages in the α-$Ni(OH)_2$/β-FeOOH bilayer structure.

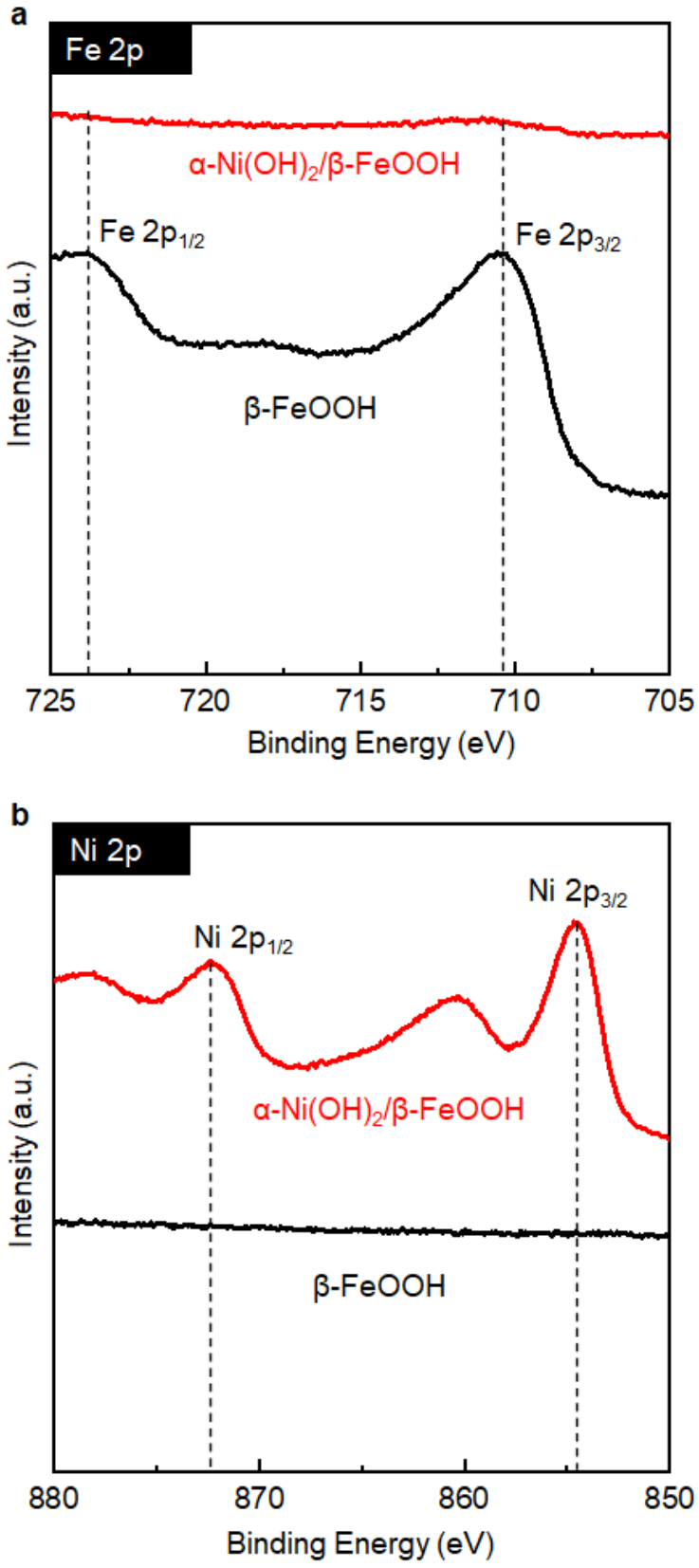

Figure 4.5. (a) Fe 2p and (b) Ni 2p XPS spectra of β-FeOOH, and α-$Ni(OH)_2$/β-FeOOH deposited on FTO substrate.

4.3.2 OER activity of α-Ni(OH)$_2$/β-FeOOH heterostructures.

The OER polarization curves of the above-mentioned α-Ni(OH)$_2$, β-FeOOH and α-Ni(OH)$_2$/β-FeOOH bilayers deposited on FTO are shown in Figure 4.6. The single-component catalysts, α-Ni(OH)$_2$ and β-FeOOH, showed overpotentials of 495 and 589 mV, respectively, at 10 mA cm^{-2} in 1 M KOH solution. In contrast, the α-Ni(OH)$_2$/β-FeOOH bilayer exhibited a decreased overpotential to 398 mV, which indicates that the bilayer structure enhances the OER activity.

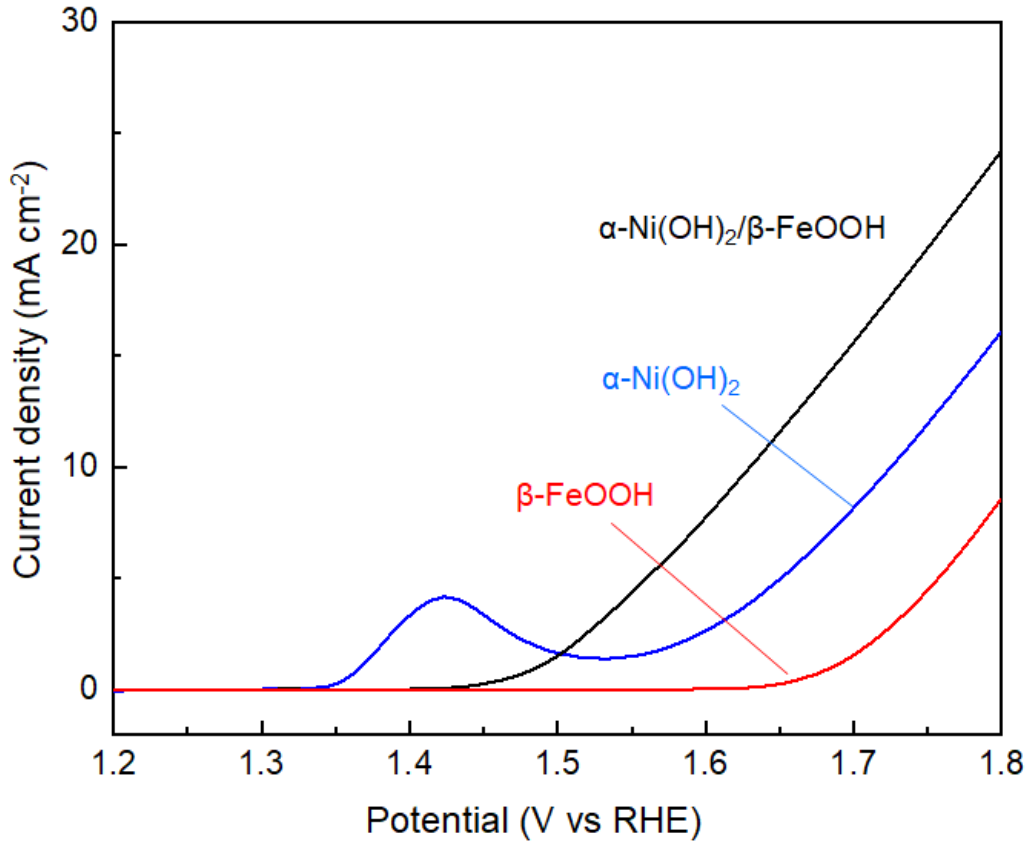

Figure 4.6. OER curves for α-Ni(OH)$_2$, β-FeOOH, and α-Ni(OH)$_2$/β-FeOOH deposited on FTO substrate.

To further enhance the catalytic activity, the deposition conditions of the α-Ni(OH)$_2$/β-FeOOH bilayer were optimized. The deposition time of either the α-Ni(OH)$_2$ or β-FeOOH layer of the bilayer was systematically varied, and the resulting OER current density values at 1.8 V were plotted (Figure 4.7). Firstly, the deposition time of the FeOOH under layer was fixed at 30 s, and that of the Ni(OH)$_2$ top layer was varied from 10 and 150 s. As a result, the current density increased up to approximately 40 s, and then decreased with the increase of the deposition time (Figure 4.7 (a)). Therefore, the deposition time was fixed at 40 s as a reasonable deposition time for the top layer of α-Ni(OH)$_2$. Then, the effect of deposition time on the β-FeOOH underlayer was investigated. The current reached a maximum at 10 or 20 s and subsequently decreased significantly as the deposition time increased (Figure 4.7 (b)).

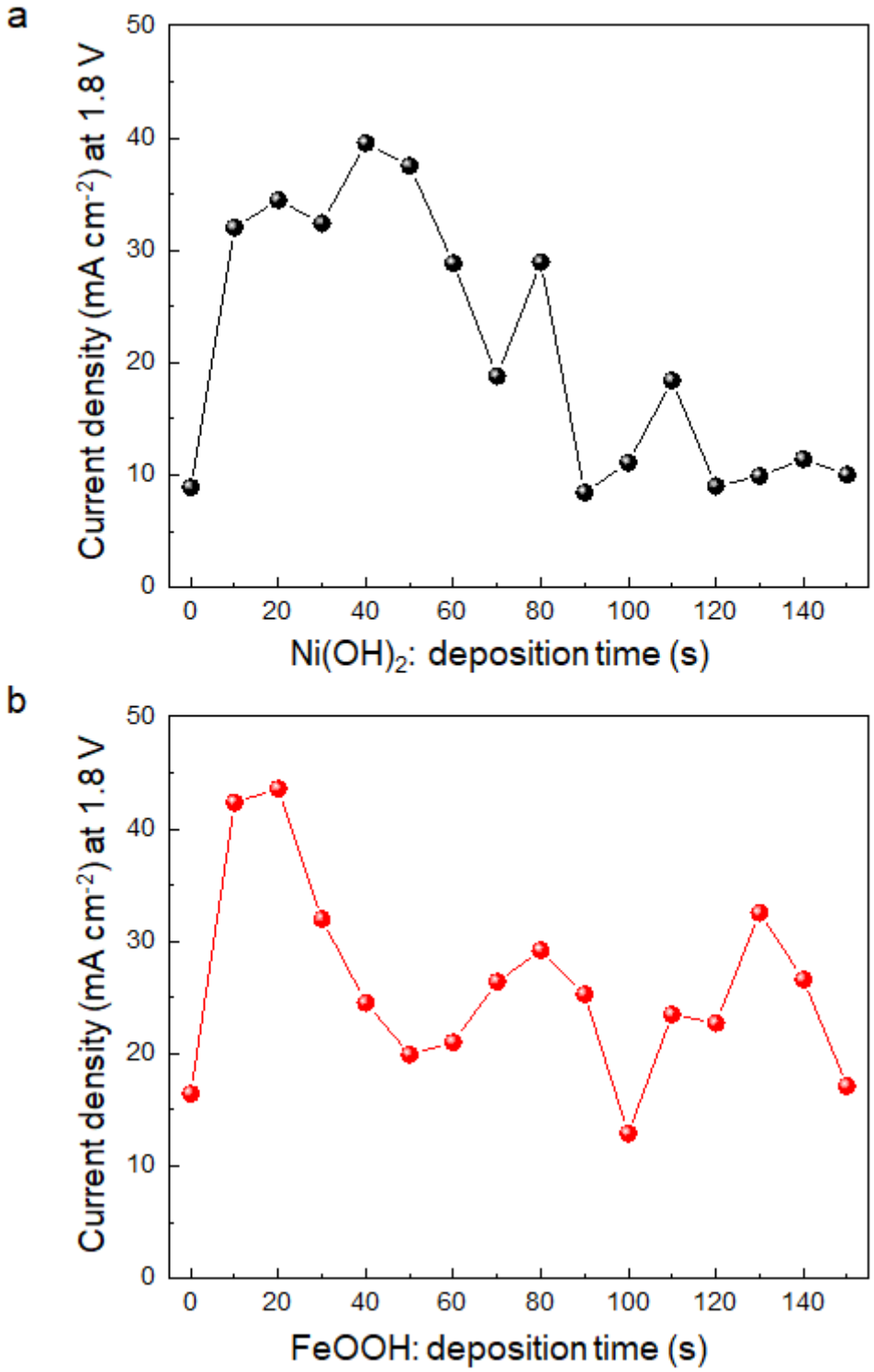

Figure 4.7. (a) Current density (mA cm^{-2}) at 1.8 V of α-$Ni(OH)_2$ layer, and (b) β-FeOOH layer in the bilayer after deposition of 10 to 150 s.

4.3.3 SEM observations of α-Ni(OH)$_2$/β-FeOOH heterostructures.

To confirm the correlation between the deposition time and the catalytic activity, SEM observation was conducted. SEM images of the samples of β-FeOOH and α-Ni(OH)$_2$ deposited on FTO, respectively, are shown (Figure 4.8). β-FeOOH has a mesh-like structure formed by the aggregation of spindle-shaped nanoparticles of approximately 100 nm in length. In contrast, α-Ni(OH)$_2$ deposition resulted in densely aggregated nanoparticles of 50-200 nm diameter.

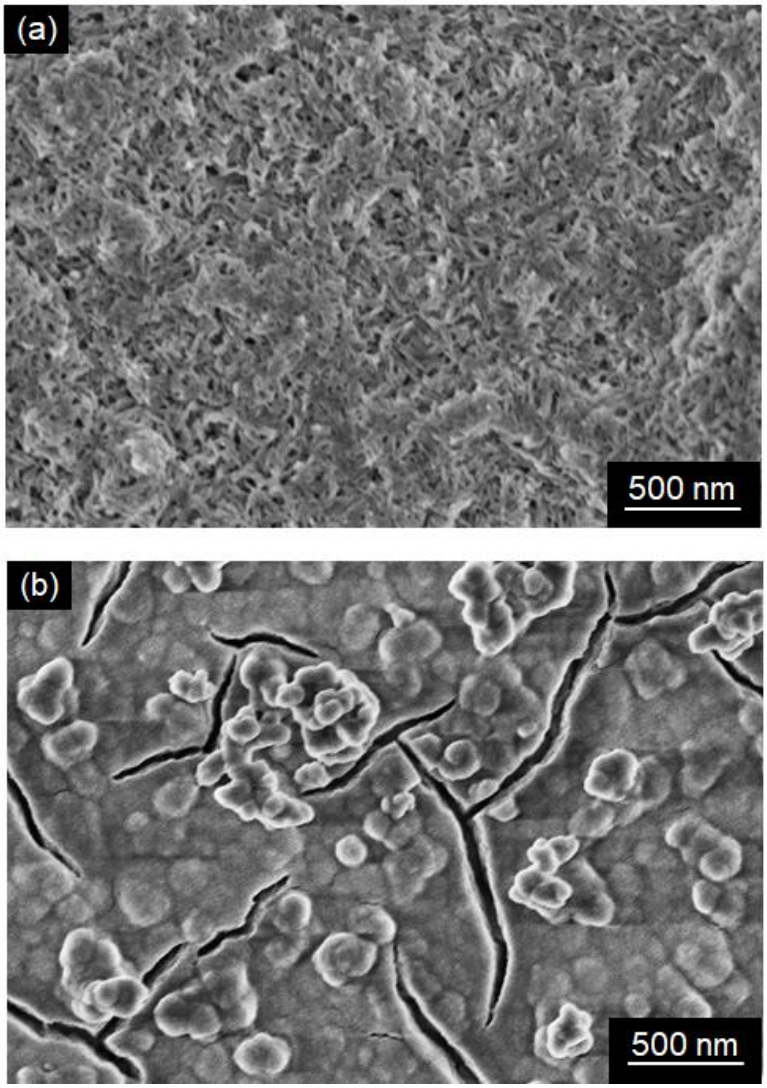

Figure 4.8. SEM images of (a) β-FeOOH, and (b) α-Ni(OH)$_2$ deposited on the FTO substrate.

Figure 4.9 (a)-(c) and Figure 4.10 (a)-(d) show the surface images of α-Ni(OH)$_2$/β-FeOOH bilayer films with varying α-Ni(OH)$_2$ deposition times. Here, the deposition time of β-FeOOH was fixed at 20 s and the α-Ni(OH)$_2$ deposition time was varied from 1 to 40 s. In the initial stage of the reaction (1, 5, 10 s), sheet-like α-Ni(OH)$_2$ was decorated on the surface of the β-FeOOH nanospindles (Figure 4.9 (a)-(c)). When the deposition time of α-Ni(OH)$_2$ increased from 15 to 20 s, the space of the mesh-like structure became almost filled with α-

$Ni(OH)_2$. (Figure 4.10 (a) and (b)). The surface appeared to be fully covered with α-$Ni(OH)_2$ after deposition for 30 s (Figure 4.10 (c)). The highest OER current was obtained when α-$Ni(OH)_2$ was deposited for 40 s (Figure 4.7 (a)), which suggests that the density of the catalytically active heterointerface increased up to 40 s. In this stage, there are pathways such as nano/mesoscale pores, allowing the diffusion of aqueous solution (reactant) into the heterointerface. In Chapter 3, it was suggested that FeOOH enhances the catalytic activity of α-$Ni(OH)_2$ at a distance of about 10 nm from the interface. Thus, if the solution could not diffuse to the heterojunction, the catalytic activity would be enhanced in the part of the α-$Ni(OH)_2$ layer that is less than 10 nm thick. The decrease in OER activity with increasing α-$Ni(OH)_2$ deposition time could be attributed to the α-$Ni(OH)_2$ layer being excessively thick and preventing the aqueous solution from diffusing to the catalytically active interface region. Likewise the α-$Ni(OH)_2$ deposition, the catalytic activity decreased with prolonged β-FeOOH deposition (Figure 4.7 (b)), indicating that excessively thick β-FeOOH layer prevented the electron transport from the active site to the conductive substrate.

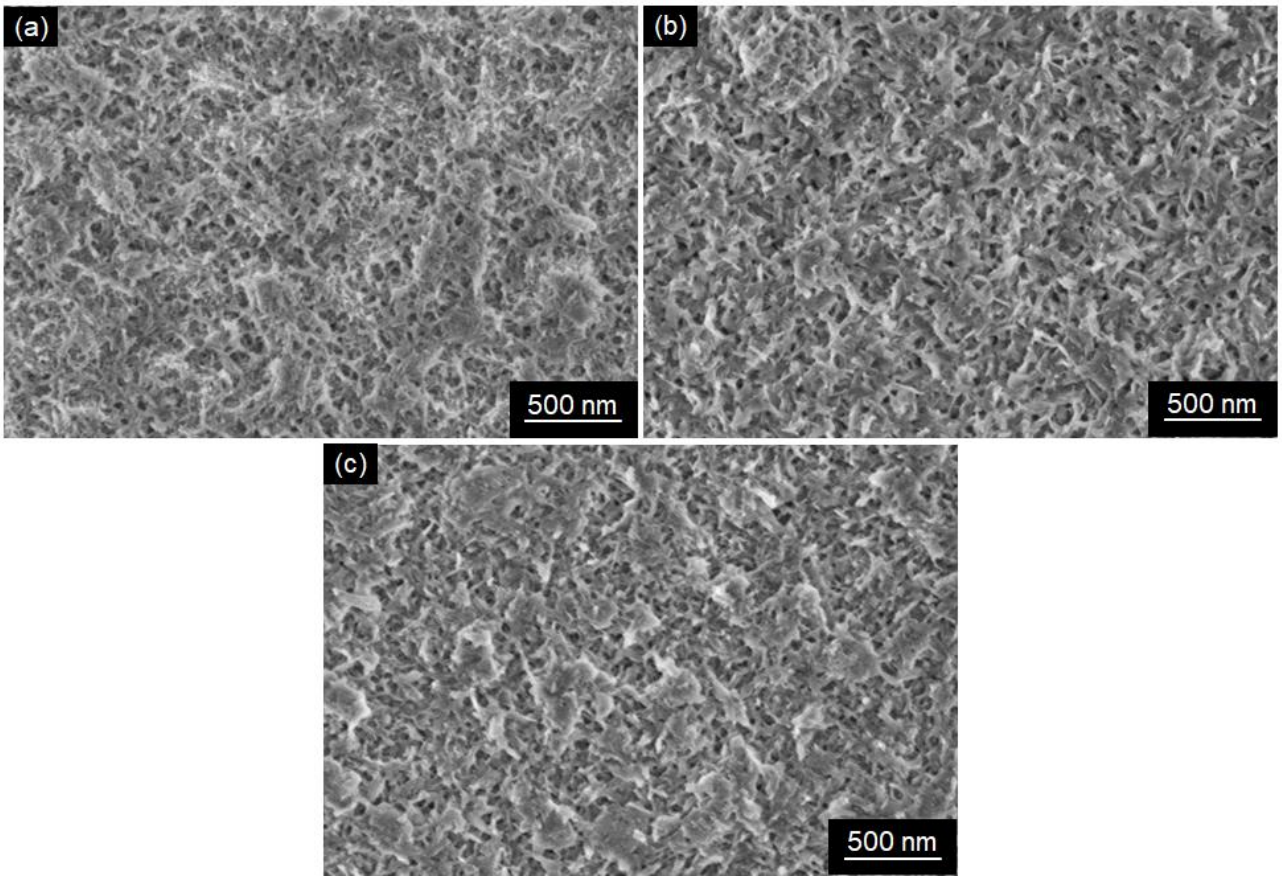

Figure 4.9. SEM images of (a)-(c) α-$Ni(OH)_2$/β-FeOOH deposited on FTO substrate. α-$Ni(OH)_2$ deposition time was (a) 1 s, (b) 5 s, and (c) 10 s.

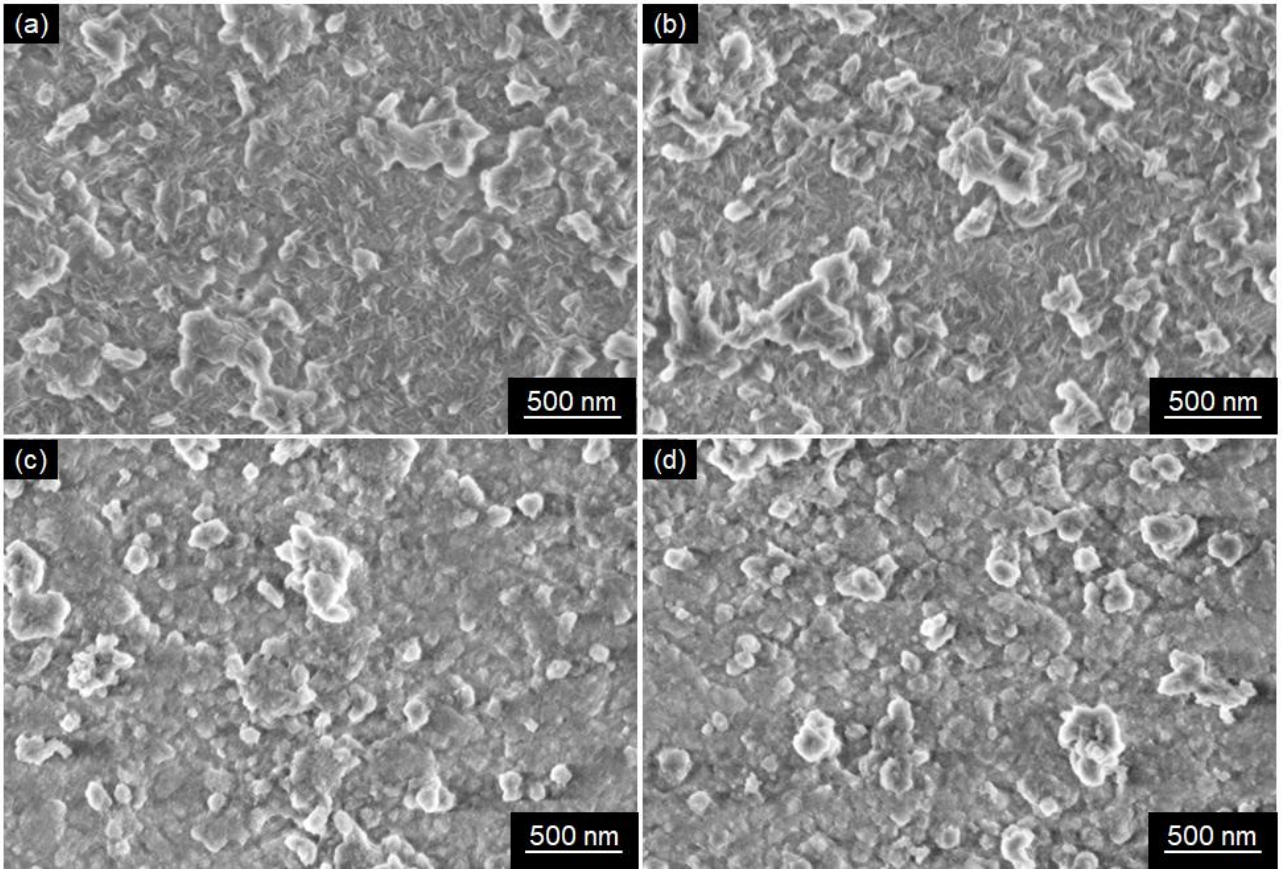

Figure 4.10. SEM images of (a)-(d) α-$Ni(OH)_2$/β-FeOOH deposited on FTO substrate. α-$Ni(OH)_2$ deposition time was (a) 15 s, (b) 20 s, (c) 30 s, and (d) 40 s.

4.3.4 OER activity and durability of α-$Ni(OH)_2$/β-FeOOH heterostructures deposited on Ni foam.

The OER polarization curve of α-$Ni(OH)_2$/β-FeOOH bilayer catalyst deposited on the Ni foam using the optimized deposition conditions is shown in Figure 4.11. The large surface area leads to a much higher current density than that deposited on the flat FTO substrate. The sample showed an excellent overpotential of 213 mV at a current density of 10 mA cm^{-2}. This value is comparable or even lower than the state-of-the-art Fe/Ni-containing hydroxide catalysts that were recently reported (Table 4.1). Furthermore, the current density remained 97% of the initial current density after 12 h of operation under the constant applied potential at 1.59 V, which demonstrated high stability (Figure 4.12).

4.4 Conclusion

In this chapter, the electrochemical deposition of α-$Ni(OH)_2$/β-FeOOH bilayer was examined in order to develop a simple method for the fabrication of a highly efficient OER catalyst. XRD and XPS analyses showed that the α-$Ni(OH)_2$/β-FeOOH bilayer was deposited on the cathode. The deposition times of the α-$Ni(OH)_2$ and β-FeOOH layers were optimized to maximize the catalytic activity. SEM observations showed

that the β-FeOOH nanomesh composed of spindle-shaped nanoparticles was gradually decorated with α-$Ni(OH)_2$ upon prolonged deposition time. The catalytic activity was maximized by fully covering the α-$Ni(OH)_2$ thin layer on β-FeOOH. The electrochemical deposition derived from the α-$Ni(OH)_2$/β-FeOOH bilayer on Ni foam showed an overpotential of 213 mV at 10 mA cm^{-2} and high stability (97% after 12 h of operation). These results indicate that the rapid, low-cost, and scalable method developed in this study has the potential to meet the requirements of the industry.

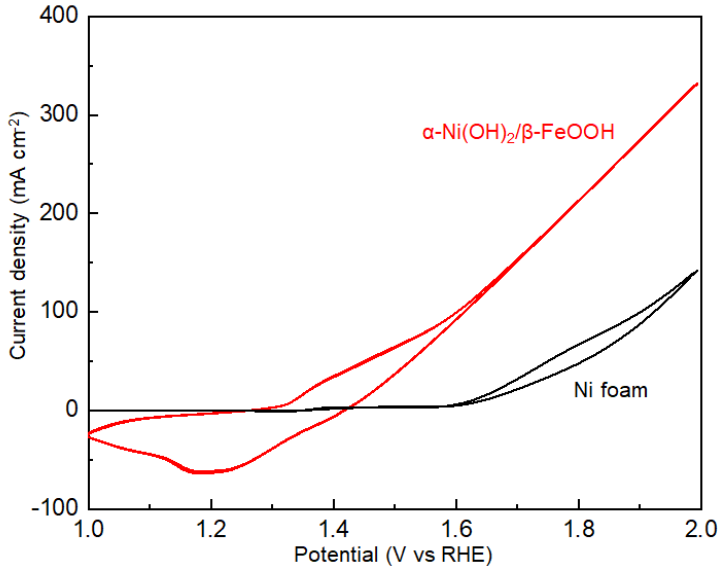

Figure 4.11. OER curves for α-$Ni(OH)_2$/β-FeOOH deposited on Ni foam.

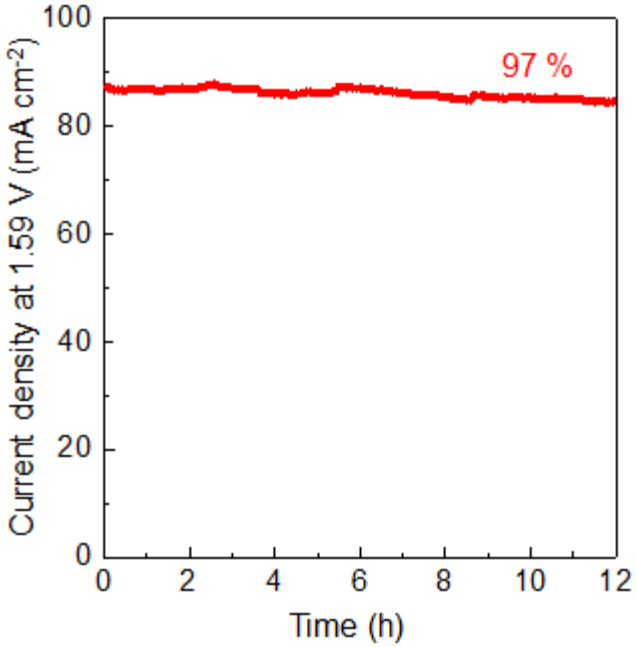

Figure 4.12. Amperometry data recorded for α-$Ni(OH)_2$/β-FeOOH deposited on Ni foam at a fixed potential of 1.59 V vs RHE.

Table 4.1. Summary of OER activity of state-of-the-art Fe/Ni containing hydroxide catalysts deposited on Ni foam in 1.0 M KOH electrolyte (from the literature).

	Overpotential (mV, 10 mA cm^{-2})	**References**
$Ni(OH)_2$/FeOOH (Chapter 4)	213	
$Ni(OH)_2$/FeOOH (Chapter 3)	234	*ACS Appl. Energy Mater.*, 4, 8, 8252, 2021[16].
Fe-doped β-$Ni(OH)_2$ nanosheets	219	*ACS Energy Lett*., 4, 3, 622, 2019[21].
amorphous and porous 2D NiFeCo hydroxide nanosheets	210	*ACS Sustainable Chem. Eng*., 7, 11, 10035, 2019[22].
3D porous core-shell Ni nanochains /NiFe LDH nanosheets	218	*J. Mater. Chem. A*, 7, 21722, 2019[23].
$Ni_{0.83}Fe_{0.17}(OH)_2$ nanosheets	245	*ACS Catal*., 8, 6, 5382, 2018[24].
NiFe LDH/NiCoP	220	*Adv. Funct. Mater*., 28, 1706847, 2018[25].
Ru-doped NiFe-LDH nanosheets	225	*Adv. Mater*., 30, 10, 1706279, 2018[26].

References

1. Seh, Z. W.; Kibsgaard, J.; Dickens, C. F.; Chorkendorff, I.; Nørskov, J. K.; Jaramillo, T. F., Combining theory and experiment in electrocatalysis: Insights into materials design. *Science* **2017,** *355* (6321), eaad4998.

2. Cook, T. R.; Dogutan, D. K.; Reece, S. Y.; Surendranath, Y.; Teets, T. S.; Nocera, D. G., Solar Energy Supply and Storage for the Legacy and Nonlegacy Worlds. *Chemical Reviews* **2010,** *110* (11), 6474-6502.

3. Dresp, S.; Dionigi, F.; Klingenhof, M.; Strasser, P., Direct Electrolytic Splitting of Seawater: Opportunities and Challenges. *ACS Energy Letters* **2019,** *4* (4), 933-942.

4. Suntivich, J.; May, K. J.; Gasteiger, H. A.; Goodenough, J. B.; Shao-Horn, Y., A Perovskite Oxide Optimized for Oxygen Evolution Catalysis from Molecular Orbital Principles. *Science* **2011,** *334* (6061), 1383-1385.

5. Suen, N.-T.; Hung, S.-F.; Quan, Q.; Zhang, N.; Xu, Y.-J.; Chen, H. M., Electrocatalysis for the oxygen evolution reaction: recent development and future perspectives. *Chemical Society Reviews* **2017,** *46* (2), 337-365.

6. Trotochaud, L.; Young, S. L.; Ranney, J. K.; Boettcher, S. W., Nickel–Iron Oxyhydroxide Oxygen-Evolution Electrocatalysts: The Role of Intentional and Incidental Iron Incorporation. *Journal of the American Chemical Society* **2014,** *136* (18), 6744-6753.

7. Friebel, D.; Louie, M. W.; Bajdich, M.; Sanwald, K. E.; Cai, Y.; Wise, A. M.; Cheng, M.-J.; Sokaras, D.; Weng, T.-C.; Alonso-Mori, R.; Davis, R. C.; Bargar, J. R.; Nørskov, J. K.; Nilsson, A.; Bell, A. T., Identification of Highly Active Fe Sites in (Ni,Fe)OOH for Electrocatalytic Water Splitting. *Journal of the American Chemical Society* **2015,** *137* (3), 1305-1313.

8. Stevens, M. B.; Trang, C. D. M.; Enman, L. J.; Deng, J.; Boettcher, S. W., Reactive Fe-Sites in Ni/Fe (Oxy)hydroxide Are Responsible for Exceptional Oxygen Electrocatalysis Activity. *Journal of the American Chemical Society* **2017,** *139* (33), 11361-11364.

9. Roy, C.; Sebok, B.; Scott, S. B.; Fiordaliso, E. M.; Sørensen, J. E.; Bodin, A.; Trimarco, D. B.; Damsgaard, C. D.; Vesborg, P. C. K.; Hansen, O.; Stephens, I. E. L.; Kibsgaard, J.; Chorkendorff, I., Impact of nanoparticle size and lattice oxygen on water oxidation on $NiFeO_xH_y$. *Nature Catalysis* **2018,** *1* (11), 820-829.

10. Wang, Q.; Shang, L.; Shi, R.; Zhang, X.; Zhao, Y.; Waterhouse, G. I. N.; Wu, L.-Z.; Tung, C.-H.; Zhang, T., NiFe Layered Double Hydroxide Nanoparticles on Co,N-Codoped Carbon Nanoframes as Efficient Bifunctional Catalysts for Rechargeable Zinc–Air Batteries. *Advanced Energy Materials* **2017,** *7* (21), 1700467.

11. Yu, L.; Yang, J. F.; Guan, B. Y.; Lu, Y.; Lou, X. W., Hierarchical Hollow Nanoprisms Based on Ultrathin Ni-Fe Layered Double Hydroxide Nanosheets with Enhanced Electrocatalytic Activity towards Oxygen Evolution. *Angewandte Chemie International Edition* **2018,** *57* (1), 172-176.

12. Song, F.; Hu, X., Exfoliation of layered double hydroxides for enhanced oxygen evolution catalysis. *Nature Communications* **2014,** *5* (1), 4477.

13. Niu, S.; Sun, Y.; Sun, G.; Rakov, D.; Li, Y.; Ma, Y.; Chu, J.; Xu, P., Stepwise Electrochemical Construction of $FeOOH/Ni(OH)_2$ on Ni Foam for Enhanced Electrocatalytic Oxygen Evolution. *ACS Applied Energy Materials* **2019,** *2* (5), 3927-3935.

14. Zhu, K.; Luo, W.; Zhu, G.; Wang, J.; Zhu, Y.; Zou, Z.; Huang, W., Interface-Engineered $Ni(OH)_2$/β-like

FeOOH Electrocatalysts for Highly Efficient and Stable Oxygen Evolution Reaction. *Chemistry – An Asian Journal* **2017,** *12* (20), 2720-2726.

15. Cheng, X.; Yuan, J.; Cao, J.; Lei, C.; Yang, B.; Li, Z.; Zhang, X.; Yuan, C.; Lei, L.; Hou, Y., Strongly coupling of amorphous/crystalline reduced FeOOH/α-$Ni(OH)_2$ heterostructure for extremely efficient water oxidation at ultra-high current density. *Journal of Colloid and Interface Science* **2020,** *579*, 340-346.

16. Taniguchi, A.; Kubota, Y.; Matsushita, N.; Ishii, K.; Nguyen, T. K. N.; Uchikoshi, T.; Suzuki, Y., Sequenced Successive Ionic Layer Adsorption and Reaction for Rational Design of $Ni(OH)_2$/FeOOH Heterostructures with Tailored Catalytic Properties. *ACS Applied Energy Materials* **2021,** *4* (8), 8252-8261.

17. Zhang, Z.; Zhou, J.; Wei, H.; Dai, Y.; Li, S.; Shi, H.; Xu, G., Construction of hierarchical NiFe-LDH/$FeCoS_2$/CFC composites as efficient bifunctional electrocatalysts for hydrogen and oxygen evolution reaction. *Journal of Materials Science* **2020,** *55* (35), 16625-16640.

18. Xu, F.; Kang, W.; Wang, X.; Liu, R.; Zhao, C.; Shen, Q., A chemical composition evolution for the shape-controlled synthesis and energy storage applicability of Fe_3O_4–C nanostructures. *CrystEngComm* **2013,** *15* (22), 4431-4437.

19. Zhao, G.; Wan, G.; Tang, Y.; Xu, X.; Zhou, X.; Zhou, M.; Deng, Z.; Lin, S.; Wang, G., Hollandite-type β-FeOOH(Cl) as a new cathode material for chloride ion batteries. *Chemical Communications* **2020,** *56* (82), 12435-12438.

20. Lv, C.; Wang, X.; Gao, L.; Wang, A.; Wang, S.; Wang, R.; Ning, X.; Li, Y.; Boukhvalov, D. W.; Huang, Z.; Zhang, C., Triple Functions of $Ni(OH)_2$ on the Surface of WN Nanowires Remarkably Promoting Electrocatalytic Activity in Full Water Splitting. *ACS Catalysis* **2020,** *10* (22), 13323-13333.

21. Kou, T.; Wang, S.; Hauser, J. L.; Chen, M.; Oliver, S. R. J.; Ye, Y.; Guo, J.; Li, Y., Ni Foam-Supported Fe-Doped β-$Ni(OH)_2$ Nanosheets Show Ultralow Overpotential for Oxygen Evolution Reaction. *ACS Energy Letters* **2019,** *4* (3), 622-628.

22. Babar, P.; Lokhande, A.; Karade, V.; Pawar, B.; Gang, M. G.; Pawar, S.; Kim, J. H., Bifunctional 2D Electrocatalysts of Transition Metal Hydroxide Nanosheet Arrays for Water Splitting and Urea Electrolysis. *ACS Sustainable Chemistry & Engineering* **2019,** *7* (11), 10035-10043.

23. Cai, Z.; Bu, X.; Wang, P.; Su, W.; Wei, R.; Ho, J. C.; Yang, J.; Wang, X., Simple and cost effective fabrication of 3D porous core–shell Ni nanochains@NiFe layered double hydroxide nanosheet bifunctional electrocatalysts for overall water splitting. *Journal of Materials Chemistry A* **2019,** *7* (38), 21722-21729.

24. Zhou, Q.; Chen, Y.; Zhao, G.; Lin, Y.; Yu, Z.; Xu, X.; Wang, X.; Liu, H. K.; Sun, W.; Dou, S. X., Active-Site-Enriched Iron-Doped Nickel/Cobalt Hydroxide Nanosheets for Enhanced Oxygen Evolution Reaction. *ACS Catalysis* **2018,** *8* (6), 5382-5390.

25. Zhang, H.; Li, X.; Hähnel, A.; Naumann, V.; Lin, C.; Azimi, S.; Schweizer, S. L.; Maijenburg, A. W.; Wehrspohn, R. B., Bifunctional Heterostructure Assembly of NiFe LDH Nanosheets on NiCoP Nanowires for Highly Efficient and Stable Overall Water Splitting. *Advanced Functional Materials* **2018,** *28* (14), 1706847.

26. Chen, G.; Wang, T.; Zhang, J.; Liu, P.; Sun, H.; Zhuang, X.; Chen, M.; Feng, X., Accelerated Hydrogen Evolution Kinetics on NiFe-Layered Double Hydroxide Electrocatalysts by Tailoring Water Dissociation Active Sites. *Advanced Materials* **2018,** *30* (10), 1706279.

Chapter 5: Summary and Conclusion

As pointed in the chapter 1, solution deposition techniques are generally inexpensive and less toxic, hence making the fabrication of functional films more environmentally friendly and more cost-effective, though there remain significant challenges to develop advanced solution thin-film processing allowing nanometric growth control. Throughout the present study, I have tried to solve this critical issue by developing alternative reaction routes, which were inspired by LbL and SILAR methods. OER catalysis was set as the application target of the films fabricated. The results are summarized as follows.

In Chapter 2, SMART was established for the direct solution deposition of α-Fe_2O_3 layers on oxide substrates. In this process, a substrate was alternatively reacted with Fe^{2+} solution as an iron source and $NaNO_2$ as an oxidizing agent. This is method yielded an α-Fe_2O_3 layer with a 150 nm thickness and a crystalline size of 47.4 nm after 90 deposition cycles. The layer-by-layer reactions were confirmed by UV-Vis spectroscopy (Figure 5.1) and SEM observations. The growth rate was ca. 1.7 nm per deposition cycle, in which Fe^{2+} cations in a Stern layer were oxidized by $NaNO_2$ to form Fe^{3+} followed by consumption by crystal growth. Thus, the designed reaction route for the α-Fe_2O_3 layer was experientially demonstrated. The defective feature of SMART-derived α-Fe_2O_3 activated and deactivated electrochemical and photoelectrochemical activity for water oxidation, respectively. The annealing in air introduced the Sn^{4+} ions in the α-Fe_2O_3 layer by the thermal diffusion from the substrate, which enhanced the electrocatalytic activity. Also, it was found that $Ni(OH)_2$/α-Fe_2O_3 heterointerface provided excellent OER activity.

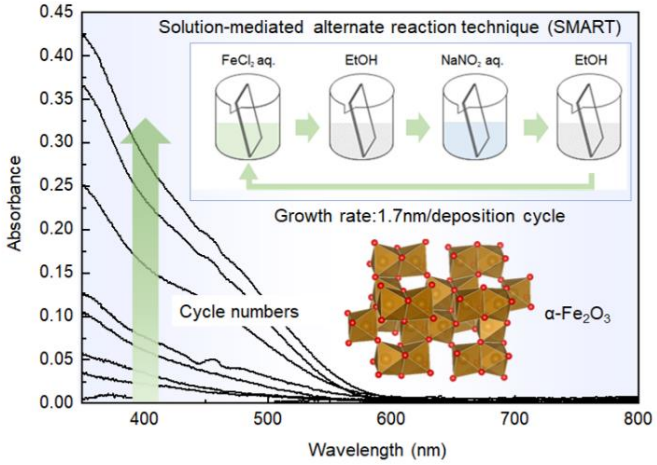

Figure 5.1. UV-Vis spectra of SMART-derived α-Fe_2O_3 obtained after 1, 3, 5, 10, 15, 20, 25, and 30 deposition cycles. (DOI: https://doi.org/10.1039/C9CE00584F)

In Chapter 3, a sequenced-SILAR method was developed for fabricating nanoscale $Ni(OH)_2$/FeOOH heterostructures. In this process, first, the substrates were immersed for 10 s in the source solution heated to 75 °C, followed by rinsing with distilled water. Next, the substrate was immersed for 10 s in a 1 M KOH

aqueous solution heated to 75 °C and then rinsed with distilled water again. A series of these operations was repeated to obtain Ni or Fe hydroxide layers as well as Ni/Fe heterostructures under the programmed deposition sequences. The films were characterized by XRD, SEM, and UV-Vis spectroscopy, etc. Figure 5.2 (a) displays a corresponding elemental mapping image of Ni and Fe clearly demonstrates the inhomogeneous distribution of these elements. The $Ni(OH)_2$, FeOOH, and $Ni(OH)_2$/FeOOH on FTO were used as the working electrodes to catalyze the OER in a three-electrode setup in an alkaline medium (1.0 M KOH). The polarization curves in Figure 5.2 (b) show that the overpotential of the $Ni(OH)_2$/FeOOH electrode is 330 mV at a current density of 10 mA cm^{-2}, which is much lower than that of $Ni(OH)_2$ and FeOOH. Electrochemical OER measurements under alkaline conditions revealed that $Ni(OH)_2$/FeOOH with dense heterojunctions had low overpotentials of 234 mV at 10 mA cm^{-2} on Ni foam. Furthermore, it was found that the design of the deposition sequences and conditions was crucial for optimizing the catalytic activity in the heterostructure. The sequenced-SILAR method, potentially employed to explore other heterostructured catalysts composed of diverse metallic and anionic species, will contribute to the further development of catalysts for sustainable energy conversion.

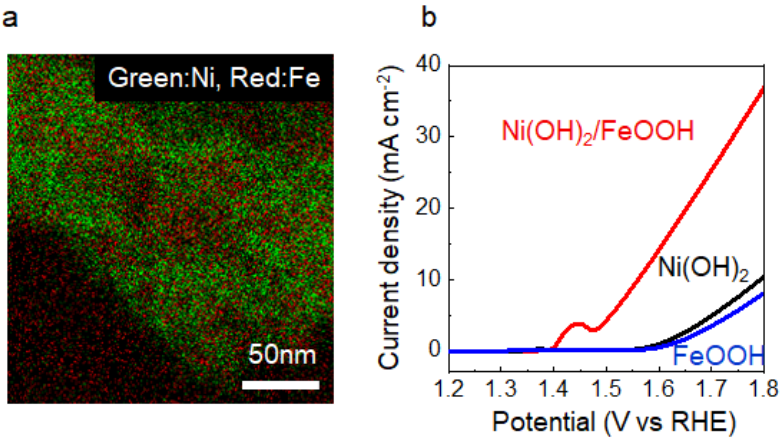

Figure 5.2. (a) Ni/Fe overlay image obtained by STEM−EDS mapping showing the formation of $Ni(OH)_2$/FeOOH heterostructures. (b) Large enchantment of OER activity by the heterostructuring. (Reprinted with permission from {*ACS Appl. Energy Mater*. 2021, 4, 8, 8252-8261[1]}. Copyright {2021} American Chemical Society.DOI: https://doi.org/10.1021/acsaem.1c01505)

Chapter 4 aimed to develop facile electrochemical deposition of $Ni(OH)_2$/FeOOH catalyst. In this process, a fluorine-doped tin oxide-coated glass (FTO) and a stainless-steel plate were used as substrates. An iron hydroxide layer was deposited on the FTO substrate by applying a constant voltage of 3 V (reaction time: 40 s) in 50 mM $FeCl_2{\cdot}4H_2O$ solution (Ethanol: Distilled water = 8:1 (volume ratio)) using an FTO substrate as the anode and a stainless-steel plate as the cathode. Then, a nickel hydroxide layer was deposited on the iron hydroxide layer by the same electrodeposition process in 50 mM $Ni(NO_3)_2{\cdot}6H_2O$ solution. The thickness of each layer was controlled by the reaction time. The structure, composition, shape, and electrochemical catalytic activity (OER) of the obtained samples were evaluated. Figure 5.3 summarizes surface SEM images of $Ni(OH)_2$, FeOOH, and $Ni(OH)_2$/FeOOH on FTO substrate. In the case of Ni hydroxide deposited on the FTO

substrate, particles with 100-300 nm were observed (Figure 5.3 (a)), while in the case of Fe hydroxide deposited on the FTO substrate, needle-like particles with 100 nm in length were observed (Figure 5.3 (b)). In the heterostructure (Figure 5.3 (c)), particle-like products were observed when Fe was deposited and then Ni was deposited. This is probably due to the formation of $Ni(OH)_2$. Electrochemical OER measurements under alkaline conditions revealed that $Ni(OH)_2$/FeOOH with dense heterojunctions had low overpotentials of 327 and 213 mV at 10 mA cm^{-2} on flat FTO (Figure 5.3 (d)) and Ni foam, respectively. Furthermore, after continuous operation for 12 h at an overpotential of 360 mV, the $Ni(OH)_2$/FeOOH heterostructures electrode retained 97% of its original current density. The data indicate that α-$Ni(OH)_2$/β-FeOOH is an effective couple for obtaining high catalytic activity and durability, but it is not clear at present whether other couples such as α-$Ni(OH)_2$/γ-FeOOH and β-$Ni(OH)_2$/α-FeOOH can similarly enhance the catalytic performance.

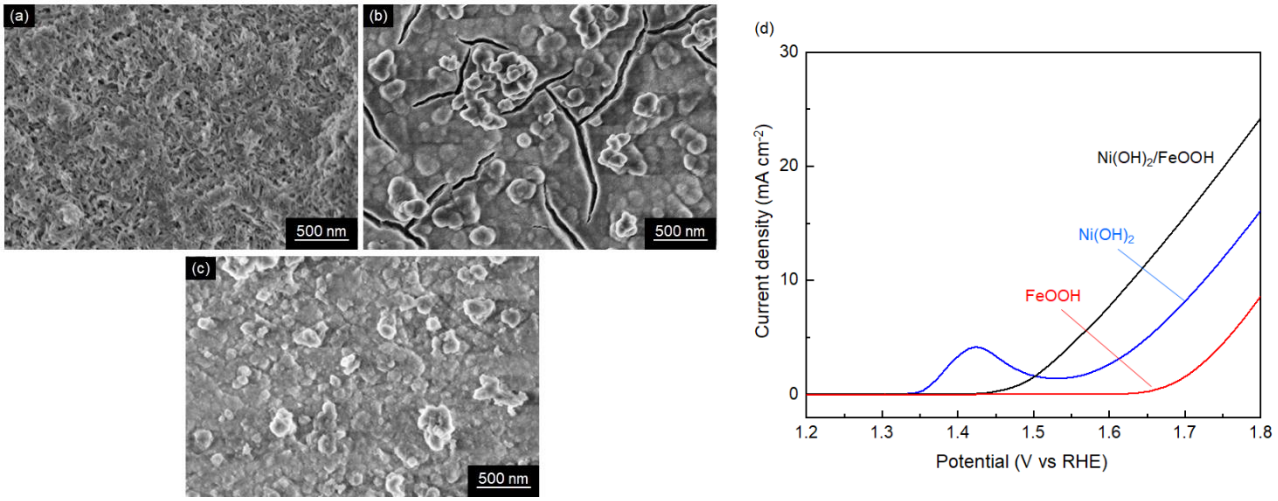

Figure 5.3. SEM images of (a) $Ni(OH)_2$, (b) FeOOH, and (c) $Ni(OH)_2$/FeOOH on FTO substrate. LSV curves for $Ni(OH)_2$/FeOOH, $Ni(OH)_2$, and FeOOH on the FTO substrate.

In conclusion, novel solution-based deposition methods have been developed for metal oxide and hydroxide nanolayers. First, nanoscale film deposition of crystalline hematite by SMART was demonstrated. Then, the concept of SILAR was successfully extended to obtain the nanoscale heterostructure based on Ni/Fe-based hydroxide. Finally, the facile electrochemical deposition route produced catalytically active heterojunction of Ni/Fe-based hydroxide. The methods developed in the thesis study can be applied to fabricate various kinds of heterostructures. Further studies will contribute not only to the development of environmentally friendly and cost-effective solution-based methods for fabricating nanostructured thin films but also to the development of a broad spectrum of functional devices.

Achievements

List of publications

[1] Asako Taniguchi, Takaaki Taniguchi, Hajime Wagata, Ken-ichi Katsumata, Kiyoshi Okada and Nobuhiro Matsushita, Liquid-phase Atomic Layer Deposition of Crystalline Hematite Without Post-growth Annealing, *CrystEngComm*, 21, 4184-4191, 2019.

[2] Asako Taniguchi, Yuta Kubota, Nobuhiro Matsushita, Kento Ishii and Tetsuo Uchikoshi, Solution-mediated nanometric growth of α-Fe_2O_3 with electrocatalytic activity for water oxidation, *Nanoscale Advances*, 2, 3933-3941, 2020.

[3] Asako Taniguchi, Yuta Kubota, Nobuhiro Matsushita, Kento Ishii, Thi Kim Ngan Nguyen, Tetsuo Uchikoshi, and Yoshikazu Suzuki, Sequenced successive ionic layer adsorption and reaction for rational design of $Ni(OH)_2$/FeOOH heterostructures with tailored catalytic properties, *ACS Applied Energy Materials*, 4, 8, 8252-8261, 2021.

Prizes

Presentation awards

International conference

[1] Asako Taniguchi and Yoshikazu Suzuki, Liquid-phase Atomic Layer Deposition of Crystalline Hematite Without Post-growth Annealing, PACRIM13, symposium. 17, Okinawa, Japan, Bronze Award for Student (December 2019).

Domestic conference

[1] Asako Taniguchi, Kento Ishii, Tetsuo Uchikoshi, Yuta Kubota, Nobuhiro Matsushita, Yoshikazu Suzuki, Solution-Mediated Alternate Reaction Technique (SMART) Toward Nanometric Growth of Hematite Thin Films, 日本セラミックス協会第 33 回秋季シンポジウム, セッション 12 (マテリアルデザインとプロセッシングデザイン), Best Presentation Award Gold for Student (September, 2020).

[2] Asako Taniguchi, Kento Ishii, Tetsuo Uchikoshi, Yuta Kubota, Nobuhiro Matsushita, Yoshikazu Suzuki, 水溶液を用いた交互反応プロセスによる結晶化ヘマタイト薄膜の低温直接合成, 表面技術協会第 142 回講演大会, 第 22 回優秀講演賞 (September, 2020).

[3] Asako Taniguchi, Yuta Kubota, Nobuhiro Matsushita, Kento Ishii, Thi Kim Ngan Nguyen, Tetsuo Uchikoshi, Yoshikazu Suzuki, Nanoscale $Ni(OH)_2$/$Fe(OH)_3$ heterostructures fabricated via an alternative deposition process and their catalytic activity, 日本セラミックス協会 2021 年年会優秀ポスター発表賞 (優秀賞) (March, 2021).

[4] Asako Taniguchi, Kento Ishii, Thi Kim Ngan Nguyen, Tetsuo Uchikoshi, Yuta Kubota, Nobuhiro Matsushita, Yoshikazu Suzuki, Electrochemical deposition of $Ni(OH)_2$/FeOOH Heterojunction for water oxidation catalysts, 日本セラミックス協会第 34 回秋季シンポジウム, グリーンプロセッシング-機能性セラミックスの低エネルギー合成による材料イノベーション, 奨励賞 (September, 2021).

[5] Asako Taniguchi, Kento Ishii, Thi Kim Ngan Nguyen, Tetsuo Uchikoshi, Yuta Kubota,

Nobuhiro Matsushita, Yoshikazu Suzuki, 電気化学堆積法による $Ni(OH)_2$-FeOOH ヘテロ積層と水電解への応用, 日本電子材料技術協会 第 58 回秋期講演大会, 奨励賞 (November, 2021).

Research funds

[1] 公益財団法人 ホソカワ粉体工学振興財団, 令和元年度研究者育成のための援助, 低温・低コスト溶液プロセスによる α-Fe_2O_3 膜の原子層堆積, 2020 年 4 月-2021 年 3 月. (The Hosokawa Powder Technology Foundation under Grant 19506)

[2] 特別研究員奨励費 (DC2), 液相原子層堆積法に立脚した低温・低環境負荷セラミックスコーティング技術の開発, 文部科学省, 2020 年-2022 年. (The Research Fellowships of Japan Society for the Promotion of Science for Young Scientists under Grant 202011961)

Conference

International

[1] Asako Taniguchi, Yoshikazu Suzuki, Liquid-phase Atomic Layer Deposition of Crystalline Hematite without Post-growth Annealing, PACRIM13, G0450, Okinawa, Japan, December, 2019. (Poster)

[2] Asako Taniguchi, Yuta Kubota, Nobuhiro Matsushita, Kento Ishii, Tetsuo Uchikoshi, Yoshikazu Suzuki, Aqueous phase layer-by-layer deposition of crystalline hematite thin films without post-growth annealing, ICACC 2021, 3487528, Online, February, 2021. (Oral)

Domestic

[1] Asako Taniguchi, Kento Ishii, Tetsuo Uchikoshi, Yuta Kubota, Nobuhiro Matsushita, Yoshikazu Suzuki, 水溶液を用いた交互反応プロセスによる結晶化ヘマタイト薄膜の低温直接合成, 表面技術協会第 142 回講演大会, B05-20, オンライン, September, 2020. (Oral)

[2] Asako Taniguchi, Kento Ishii, Tetsuo Uchikoshi, Yuta Kubota, Nobuhiro Matsushita, Yoshikazu Suzuki, Solution-Mediated Alternate Reaction Technique (SMART) Toward Nanometric Growth of Hematite Thin Films, 日本セラミックス協会第 33 回秋季シンポジウム, セッション 12 (マテリアルデザインとプロセッシングデザイン), 2K17, オンライン, September, 2020. (Oral)

[3] Asako Taniguchi, Yuta Kubota, Nobuhiro Matsushita, Kento Ishii, Thi Kim Ngan Nguyen, Tetsuo Uchikoshi, Yoshikazu Suzuki, Nanoscale $Ni(OH)_2$/$Fe(OH)_3$ heterostructures fabricated via an alternative deposition process and their catalytic activity, 日本セラミックス協会 2021 年年会, 1PB127, オンライン, March, 2021. (Poster)

[4] Asako Taniguchi, Kento Ishii, Thi Kim Ngan Nguyen, Tetsuo Uchikoshi, Yuta Kubota, Nobuhiro Matsushita, Yoshikazu Suzuki, Convenient Electrochemical deposition of $Ni(OH)_2$/$Fe(OH)_3$ Heterojunction with Controllable Electrocatalytic Activity for water oxidation, 日本セラミックス協会 2021 年年会, 3K09, オンライン, March, 2021. (Oral)

[5] Asako Taniguchi, Kento Ishii, Thi Kim Ngan Nguyen, Tetsuo Uchikoshi, Yuta Kubota, Nobuhiro Matsushita, Yoshikazu Suzuki, Electrochemical deposition of $Ni(OH)_2$/FeOOH Heterojunction for water oxidation catalysts, 日本セラミックス協会第 34 回秋季シンポジウム, セッション 12 (グリーン

プロセッシング―機能性セラミックスの低エネルギー合成による材料イノベーション―), 2K03, オンライン, September, 2021. (Oral)

[6] Asako Taniguchi, Yuta Kubota, Nobuhiro Matsushita, Kento Ishii, Thi Kim Ngan Nguyen, Tetsuo Uchikoshi, Yoshikazu Suzuki, 溶液プロセスを用いた交互積層法による $Ni(OH)_2$/FeOOH ヘテロ構造の作製と酸素生成触媒への応用, 表面技術協会第 144 回講演大会, オンライン, September, 2021. (Oral)

[7] Asako Taniguchi, Kento Ishii, Thi Kim Ngan Nguyen, Tetsuo Uchikoshi, Yuta Kubota, Nobuhiro Matsushita, Yoshikazu Suzuki, 電気化学堆積法による $Ni(OH)_2$-FeOOH ヘテロ積層と水電解への応用, 日本電子材料技術協会 第 58 回秋期講演大会, I-A5, オンライン, November, 2021. (Oral)

Acknowledgements

It is my pleasure to acknowledge the assistance of many who have helped me to bring this work to its final form.

Words fail to express the deep debt of gratitude I owe to Professor Yoshikazu Suzuki, Faculty of Pure and Applied Sciences, University of Tsukuba, for his stimulating discussions, critical comments & suggestions, inspiring guidance and constant encouragement during the course of the present investigation. The author would like to thank Prof. Hiroko Tokoro, and Prof. Junji Nakamura, Faculty of Pure and Applied Sciences, University of Tsukuba, and Prof. Tetsuo Uchikoshi, Research Center for Functional Materials, National Institute for Materials Science (NIMS). Their valuable suggestions are greatly acknowledged.

I owe to Dr. Kento Ishii, and Dr. Thi Kim Ngan Nguyen, Research Center for Functional Materials, National Institute for Materials Science (NIMS) for their encouragement and help. The author thanks to Prof. Nobuhiro Matsushita and Prof. Yuta Kubota, Department of Materials Science and Engineering, School of Materials and Chemical Technology, Tokyo Institute of Technology for XRD measurement, measurement of photoelectrochemical properties. I would like to thank Prof. Jun Akedo, Dr. Yasuhito Matsubayashi, and Dr. Taku Goto, National Institute of Advanced Industrial Science & Technology, AIST for fruitful discussions. The author gratefully acknowledges to author's colleagues of Yoshikazu Suzuki Laboratory for their kind help.

I would like to thank Prof. Naoto Shirahata and Mr. Hiroyuki Yamada at International Center for Materials Nanoarchitectonics (MANA), National Institute for Materials Science (NIMS) for the assistance of UV-Vis measurement. I also thank Open Facility Center, Materials Analysis Division, Tokyo Institute of Technology, for XRD, cross-sectional STEM, and STEM-EDS analyses. I appreciate the Open Facility Network Office, Research Facility Center for Science and Technology, University of Tsukuba, for SEM observations. This work was supported in part by the Hosokawa Powder Technology Foundation under Grant 19506 and the Research Fellowships of Japan Society for the Promotion of Science for Young Scientists under Grant 202011961.

My sincere thanks to my father Hideyo Takeuchi, mother Ushio Takeuchi, and brother Itofumi Takeuchi for their support throughout.

I am deeply grateful to my husband Takaaki Taniguchi, and son Kazuha Taniguchi for their hearty supports and understandings.

Asako Taniguchi

February, 2022
Tsukuba, Japan